# Preparation, Characterization and Oxidation of Nanostructured Pt-Rh Surfaces

Christine Pettersen


Master Thesis
Materials Science for Energy and Nanotechnology
60 credits

Department of Chemistry
Faculty of Mathematics and Natural Sciences

UNIVERSITY OF OSLO

June 2020

2020

**Preparation, Characterization and Oxidation of Nanostructured Pt-Rh Surfaces**

Christine Pettersen

http://www.duo.uio.no/

# Acknowledgment

The work presented in this MSc was performed in the NAFUMA group at the Department of Chemistry, Faculty of Mathematics and Natural Sciences at the University of Oslo, from August 2018 to June 2020.

First, I want to thank my supervisor Anja O. Sjåstad. Thank you for letting me work on this project, and for providing me with the best supervison I could have asked for. Your dedication, level of knowledge and good work ethics is something I really admire. It has inspired me when working on this thesis, and it is something I will bring with me when going forward in life.

I also want to thank my co-supervisor Oleksii Ivashenko. Your guidance throughout this project has been extremely valuable to me; from teaching me how to operate the STM, performing image and data analysis, giving advice on writing, and so much more. Thank you for letting me ask stupid questions without laughing (too much), and always providing me with answers when needed. It has been a pleasure to work with you for the last couple of years!

Throughout the years at the University of Oslo, I have had the pleasure of getting to know a lot of amazing people. Good memories have been made, and the years here would definitely not have been the same without you. Especially thank you to Ida, Hanne, Silje and Martin in the NAFUMA group for all the uplifting conversations, coffee and lunch breaks, dinners and much more!

A big thank you to my parents and my sister, Astrid for all the support. I appreciate that you always want the best for me, and encourage me to work hard. Thank you for providing me with much-needed coffee throughout my years at university, and for all the Sunday dinners!

I also want to thank my friends for reminding me that there is a world outside the university. All the dinners, nights out and vacations have been much needed and highly valued!

Finally, I want to thank Ole for the constant love and support, and for always cheering me on! And thank you for reminding me of what is most important in life.

# Abbreviations

| | |
|---|---|
| AES | Auger Electron Spectroscopy |
| AP | Ambient Pressure |
| AP | As Prepared |
| AP-XPS | Ambient-Pressure X-ray Photoelectron Spectroscopy |
| CAICISS | Coaxial Impact-Collision Ion Scattering Spectroscopy |
| ccp | cubic close-packed |
| DFT | Density Functional Theory |
| DOS | Density of State |
| EBE | Electron Beam Evaporator |
| EELS | Electron Energy Loss Spectroscopy |
| fcc | face-centered cubic |
| GC | Gas Chromatography |
| hcp | hexagonal close-packed |
| HOPG | Highly Oriented Pyrolytic Graphite |
| HP-STM | High Pressure Scanning Tunneling Microscopy |
| HRCLS | High Resolution Core Level Spectroscopy |
| HREELS | High Resolution Electron Energy Loss Spectroscopy |
| HT-STM | High Temperature Scanning Tunneling Microscopy |
| LEED | Low Energy Electron Diffraction |
| IMFP | Inelastic Mean Free Path |
| MPRI | Multiphoton Resonance Ionization |
| MS | Mass Spectrometery |
| NAP-XPS | Near-Ambient Pressure X-ray Photoelectron Spectroscopy |
| NP | Nanoparticle |
| PA | Post-Annealed |
| PAX | Photoemission Spectra of Adsorbed Xe |
| PVD | Physical Vapor Deposition |
| QMS | Quadrupole Mass Spectrometery |
| RT | Room Temperature |
| RT-RHEED | Real-Time Reflection High-Energy Electron Diffraction |
| SPL | Surface Preparation Laboratory |
| SPM | Scanning Probe Microscopy |
| STM | Scanning Tunneling Microscopy |
| SXRD | Surface X-ray Diffraction |

| | |
|---|---|
| TDS | Thermal Desorption Spectroscopy |
| TEAS | Thermal Energy Atomic Scattering |
| TEM | Transmission Electron Microscopy |
| TLK | Terrace-Ledge-Kink |
| TPD | Temperature-Programmed Desorption |
| UHV | Ultra-High Vacuum |
| UPS | Ultraviolet Photoelectron Spectroscopy |
| XAS | X-ray Absorption Spectroscopy |
| XPS | X-ray Photoelectron Spectroscopy |
| XP | X-ray Photoelectron |
| XRR | X-ray Reflectivity |

# Abstract

Studying the Pt-Rh system and its behavior in gas atmospheres is useful for the understanding of catalytic reactions. In this master project, preparation and characterization of Pt-Rh surfaces in UHV and oxidizing conditions was performed. This was done in order to get a better understanding of the nucleation, growth and alloying behavior of Pt-Rh surfaces, and to see how the variations in nanostructured surfaces alter their oxidation behavior.

Preparation of Pt/Rh(111) surfaces was performed in our Reactor STM instrument, and surfaces were characterized by means of LEED and STM at UHV. Varying preparation conditions like deposition temperature (300 – 700 K), coverage (0.14 – 2.3 ML), post-annealing time and temperature, was shown to dictate morphology, growth and degree of alloying. From these results, a synthesis strategy roadmap for preparation of nanostructured Pt/Rh(111) surfaces was made. The Pt/Rh(111) roadmap was compared to a similar roadmap for the inverse system (Rh/Pt(111)). The results indicated that choice of substrate, Pt(111) or Rh(111), leads to significant differences in the nanostructure composition. To expand on the results from the Rh/Pt(111) roadmap, Rh/Pt(111) surfaces with coverages in the range 0.4 – 1.2 ML were prepared and characterized by means of XPS in UHV. The XPS results indicated that PA to higher temperatures (700-770 K) led to more subsurface diffusion of Rh and alloying compared to lower PA temperatures (600 K), confirming results obtained in the initial Rh/Pt(111) roadmap.

To establish how different nanostructured alloys behave in oxidizing conditions, a selection of surfaces (from bare Rh(111) to 2.3 ML Pt/Rh(111)) were exposed to low oxygen pressures ($pO_2 = 1 \times 10^{-3}$ mbar) at 700 K. The surfaces were characterized by means of LEED and STM at UHV. For bare Rh(111) and low Pt enrichement (0.14 ML), a Rh surface oxide was formed displaying a characteristic moiré pattern over the entire surface. Increase in the Pt content led to a gradual loss of moiré pattern. For the 2.3 ML Pt/Rh(111) surface, no surface oxide formed.

In addition, NAP-XPS measurements on Rh/Pt(111) surfaces were performed at 1 mbar $O_2$ and 600 K. The surfaces had previously been post-annealed to different temperatures (600-770 K). XP spectra revealed that formation of Rh surface oxide correlated with the degree of alloying with Pt(111), where more alloying prevented oxidation. These results were in line with what had been observed in STM and LEED for Pt/Rh(111) surfaces in low oxygen pressures. This led to the conclusion that amount of Rh on the surface is what governs the degree of surface oxide formation. Depending on the choice of substrate (Pt(111) or Rh(111)), the Rh content on the surface can be modified by either changing the PA/deposition temperature, or by tuning the Pt coverage.

# Contents

# 1 Introduction

This MSc thesis describes preparation of bimetallic PtRh surfaces on Rh(111) and Pt(111) single crystals at variable synthesis conditions. Obtained nanostructured surfaces are described with methods as scanning tunneling microscopy (STM) and X-ray photoelectron spectroscopy (XPS) in the pressure range from ultra-high vacuum (UHV) to ambient pressure (AP), in gas atmospheres relevant for ammonia oxidation. In the following a brief introduction to the background of the project is given, followed by an overview of relevant literature available on the preparation and characterization of Pt or Rh deposited on Pt(111) as well as Pt or Rh deposited on Rh(111), and on Pt-Rh surfaces in oxygen atmospheres. In the end, the motivation behind the project is described.

## 1.1 Background

Catalysis plays a key role in most chemical industry- and energy related production processes, and more than 90% of all chemical processes are activated catalytically using heterogeneous or homogeneous catalysts [1]. Fundamental knowledge of the catalysts goes through understanding of the surface phenomena. On the heterogeneous interface between the surface atoms on the solid catalyst and the gas/liquid reactant molecules, products form via elementary reaction steps. Traditionally, mechanistic insight into the catalytic processes is achieved by combining classic catalysis on real industrial catalysts with surface science on model surfaces. However, a major issue is the huge gap in operative process parameters as temperature and pressure together with the solid catalyst and instrumentation, and approaches between the two disciplines. We often denote this as the materials-, pressure- and temperature gap [2-5]; see illustration in Figure 1.1.

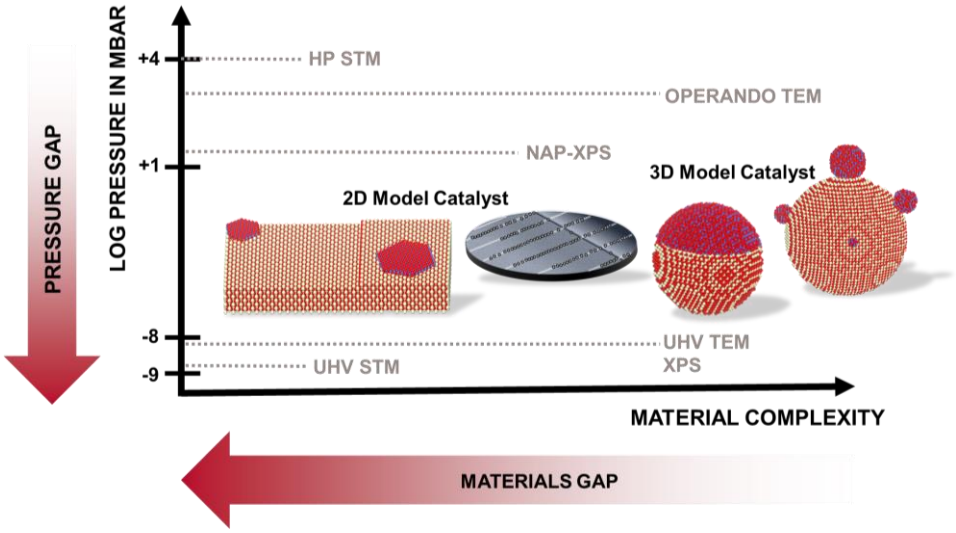


Figure 1.1: Illustration of the materials gap and pressure gap, where increased complexity of the material studied decreases the materials gap, and increased pressure decreases the pressure gap. Different characterization techniques are placed in the pressure range in which they are operated, as well as the complexity of the sample.

Industrial catalysts are frequently ill defined, consisting of a porous support material (e.g. alumina) with deposited alloyed metallic nanoparticles with heterogeneous element distribution, a wide size distribution and with irregular shapes (facets). Such materials are difficult to use in surface-science approaches and in single parameter materials studies. As a result, the *model system approach* was developed [6] (p. 461). Model catalysts are well-defined two- or three-dimensional simplified versions of the real catalysts, and they can be single-crystal surfaces, single crystal surfaces modified into alloyed surfaces, or single crystals with oxidized surfaces and deposited nanoparticles [7-11]. Finally, well-defined colloidal nanoparticles (size, shape and compositional control) deposited onto a support material as a honeycomb or powders belong to the model systems [12]. Such model materials allow for exploring effects when systematic tuning materials parameters as particle size, shape and composition. Model catalysts are used to simplify fundamental studies, and results from such studies are extrapolated to give a prediction of how the real-life, complex catalyst behave. With the development in the complexity of the model systems, the scientists are moving in a direction of closing the materials gap.

Surface sensitive techniques and techniques with sub-atomic resolution, such as STM, XPS and transmission electron microscopy (TEM), are typically operated at UHV and at ambient temperature or temperatures below. Although the surface-science approach, with the use of model catalysts at lower pressures has been ground-breaking in many aspects, a significant problem and limitation to the methods was identified already in the 1980s [13]. The working conditions and structure of the real catalyst deviate strongly from the simple model catalysts characterized in mild, often UHV conditions. In industry, the pressure is in the several bar range and operating temperatures are high, and the catalysts are much more complex in their structure. In other words, the active surface at real process conditions is likely to be different from the one observed by the surface sensitive techniques in good vacuum. Consequently, our interpretations of the active phase(s) might be misleading or wrong. The discrepancy between the UHV conditions in the laboratory to the several bars used in industry is called the *pressure gap* [2]. However, through the last decades a tremendous development in the instrumentation have taken place. XPS has become operative in the mbar range (near-ambient pressure XPS (NAP-XPS)) whereas special versions of STM and TEM can be operated beyond atmospheric pressure [1, 14]. A closer look on STM operating at higher pressures and NAP-XPS is presented in section 2.3.1.5 and 2.3.2.4, respectively.

Finally, most commercial chemical processes are taking place above room temperature (RT) whereas the surface sensitive techniques typically were designed for operation at RT and below. This is also a real constraint, as we know all phases or structures have a defined thermal stability window, and we might risk concluding on wrong active phases if the investigations not are carried out at realistic temperatures; this is the so-called *temperature gap* [15]. Again, instrumental developments have taken place. Currently we are able to investigate surfaces by means of STM and TEM up to around 1275 K in dedicated systems [1, 16] , and NAP-XPS up to typically 875-975 K [17, 18].

Despite there has been a tremendous development both in surface sensitive instrumentation and in the development of highly well-defined nanostructured model surfaces, scientists working on the interface between surface science, catalysis and materials science still need to push the limits to mimic the real chemical processes outermost using surface sensitive tools.

Returning to the fact that more than 90% of all chemical processes are catalytically activated, it is easy to pick examples of catalysis with huge impact for society. Ammonia oxidation is such a process, and oxidation of ammonia give rise to three nitrogen based products [19, 20], as described in equations 1.1, 1.2 and 1.3 below.

$$4NH_3(g) + 5O_2(g) \rightarrow 4NO(g) + 6H_2O(g) \quad 1.1$$

$$4NH_3(g) + 3O_2(g) \rightarrow 2N_2(g) + 6H_2O(g) \quad 1.2$$

$$4NH_3(g) + 4O_2(g) \rightarrow 2N_2O(g) + 6H_2O(g) \quad 1.3$$

Depending on process conditions, product selectivity and usage area is altered. If high temperatures (1075-1275 K) are used over PtRh catalyst gauzes, NO formation is the favored product [19]. The ammonia oxidation step is optimized for this reaction in the $HNO_3$ production (and N-based fertilizers). In order to convert NO to $HNO_3$, NO is oxidized homogeneously to $NO_2$ before converted to $HNO_3$ by reaction with water [21].

However, if the ammonia oxidation is carried out at milder temperature conditions (475-775 K), $N_2$ formation is promoted (equation 1.2). This is utilized in NOx abatement processes. In NOx abatement, NOx is first reduced by $NH_3$ to $N_2$. In order to have full removal of NOx, an excess of $NH_3$ has to be added to the process stream. Excess $NH_3$ (in ppm range) is the subsequently oxidized to $N_2$ around 475-775 K. Various catalytic systems are explored for this purpose [19], including PtRh nanoparticles [22, 23].

## 1.2 The Platinum – Rhodium System

The work presented in this MSc thesis is based on Pt-Rh surfaces, but to our knowledge no phase diagram of the surface Pt-Rh alloy has been made. Therefore we use the phase diagram for *bulk* Pt-Rh as our starting point. Both metals crystallize with the face-centered cubic (fcc) structure. The phase diagram shown in Figure 1.2 present the expected phases as a function of temperature and ratio of Pt and Rh. Above 1030 K, Pt and Rh form a solid solution [24]. An immiscibility dome occur at around

1030 K, and below this temperature the solid solution is expected to segregate into pure Rh and Pt phases. The dashed line indicates that this is only based on calculations, and not proved experimentally. Experimental results indicate that there is some short range order, and a study by Steiner et al. showed no local decomposition of Rh and Pt [24]. As mentioned, the phase diagram is based on the expected behavior of bulk Pt-Rh, and when going into the nano-size regime the behavior is not necessarily the same. It has been shown that nanoparticles of Pt-Rh form a solid solution [25, 26].

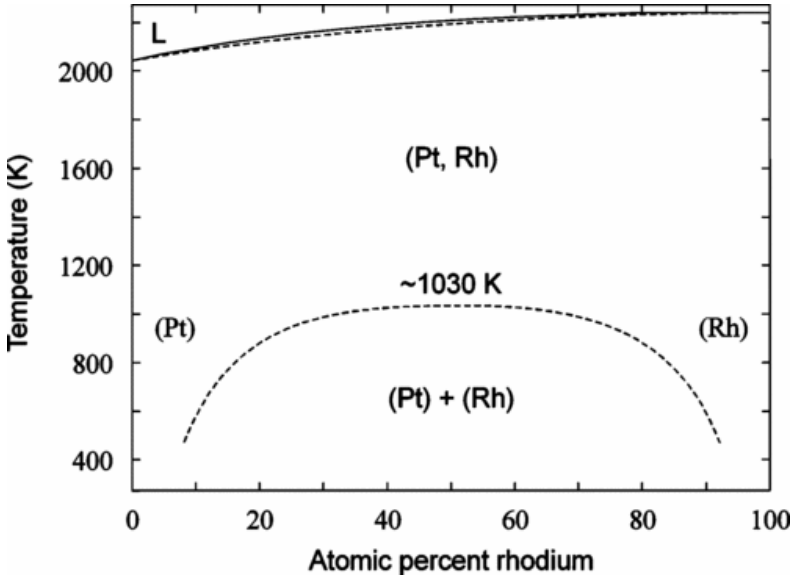


Figure 1.2: Phase diagram of Pt and Rh. The dashed line indicates that an immiscibility dome is expected at 1030 K, where Pt and Rh segregate. Figure from [27].

## 1.3 Previous Work

In this section, some of the previous work done on characterization of four different metal on metal systems will be introduced. These are pure Pt on Pt(111) and Rh on Rh(111), and bimetallic Rh on Pt(111) and Pt on Rh(111). Literature describe the morphology and surface structures obtained when evaporating metal on single metal surfaces, which heavily depend on deposition temperature and post-annealing (PA) temperature. Studies of catalytic activity reveal that the oxide phase or a surface oxide in some cases is the catalytic active component [28-30]. Hence, attention should also be given to the different structures that form upon exposing the surfaces to oxygen at different pressures and temperatures. Previous work done on oxidation of Pt(111) and Rh(111) and a description of the surface structures obtained is included in this section. For a more detailed description on characteristics of surfaces, both clean and adsorbate structures, see section 2.1.

### 1.3.1 Pt on Pt(111)

The morphology of the obtained Pt layer(s) depends strongly on the substrate temperature, and presence of impurities. In the origin of this dependency is mobility of Pt atoms on Pt(111), which is controlled by a range of barriers for diffusion (terrace, corner, step, and intralayer diffusion) and dissociation (kink, step, and dimer dissociation). Owing to the sixfold symmetry of a fcc (111) surface, the formation of a hexagon-like island with a sixfold symmetry is expected. In such a hexagon-like island, two types of steps can be distinguished: A and B steps, exhibiting (111) and (100) microfacets, respectively.

Comsa and co-authors showed how island shapes change in response to increase in surface temperature during Pt deposition [31], [32]. Dendritic islands form at 205 K, at which surface mobility is restricted and kinks cannot be healed (Figure 1.3 left). Higher temperature increases mobility, allowing for kinks healing resulting in more compact, triangular and hexagonal shapes. A similar nucleation and growth behavior has been reported for Ru/Pt(111) [33]. Interestingly, initially the triangular islands were observed both at low and higher temperatures, while the hexagonal shape appeared at intermediate range (around 455 K). The difference between high and low T triangles is in the type of steps they exhibit, low temperature favored islands with A steps, and high temperatures – B steps [34, 35].

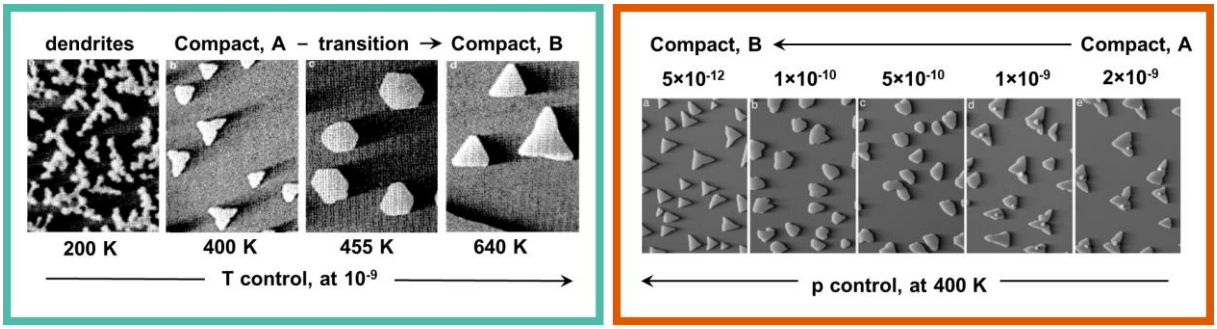


Figure 1.3: Temperature (left) and pressure (right) dependence of the morphology of Pt on Pt(111). At residual UHV pressure of CO 400 K deposition results in compact "A" triangles. Decreasing background CO pressure to $10^{-12}$ mbar (right) or increasing surface temperature above 455 K (left) results in lower CO surface coverage, and as a result triangles with B steps appear. Adapted from [34], [36].

Later study of the transition from A-step-bound island to the B one, initially induced by increase in temperature, was possible to achieve by varying UHV cleanliness [36]. Specially achieved UHV with CO pressure of not more than $5\times10^{-12}$ mbar, resulted in a triangular island with B steps at 400 K, contrary to what was expected from temperature-dependent study (Figure 1.3 right). The key reason for this result is preferential adsorption of CO on step atoms. At low temperature and regular UHV, CO will be present at the surface, inducing preferential formation of A-steps. Removal of CO from the surface either by maintaining better UHV or by desorbing it at higher temperatures will result in cleaner surface and formation of B steps. The latter indeed was observed in the earlier experiments.

### 1.3.2 Rh on Pt(111)

A study performed by Zheng el al. [37] show the variety of morphologies obtained when depositing Rh on a Pt(111) single crystal. The STM images obtained by varying temperature and coverage were summarized in a synthesis roadmap shown in Figure 1.4. RT deposition of Rh on Pt(111) resulted in multilayered triangular islands, which upon PA to temperatures in the range 450 - 750 K showed cluster growth and transformation to hexagonal islands. Mixing of Rh and Pt and roughening occurred at the step edges, and above 650 K flattening of islands occurred. It was found that PA to 600 K was necessary for substantial mixing of Pt and Rh. In addition, direct deposition at temperatures in the range 300 - 700 K was performed. A mixed morphology was obtained at 400 K with single-layered triangles, two-layered hexagons, and partially covered two-layered islands. Deposition in the temperature range 450 – 550 K resulted in larger single- and double-layered island with triangular shape, exhibiting both A- and B-steps. It was indicated that PA resulted in more stable surfaces compared to direct high-temperature deposition.

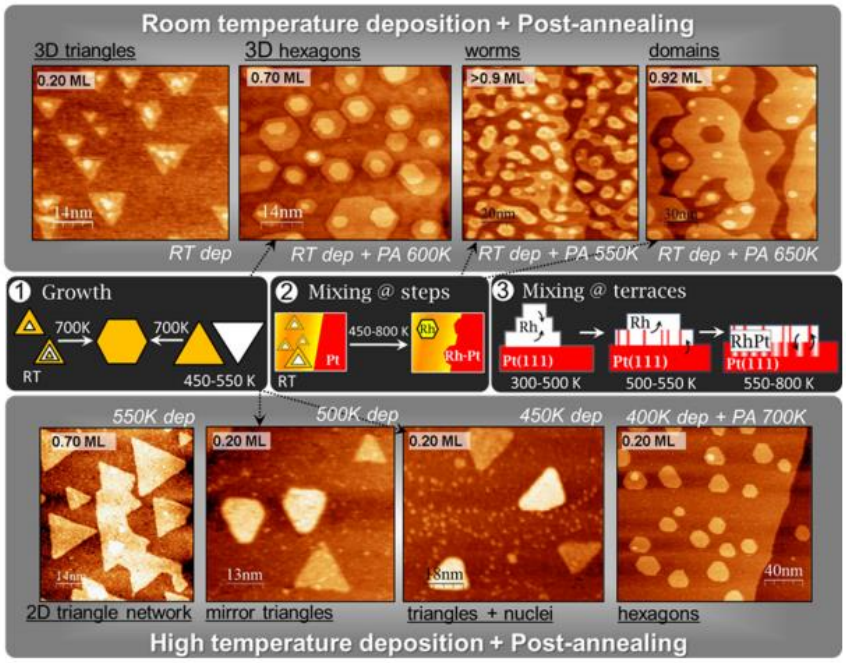


Figure 1.4: Roadmap with STM images of Rh on Pt (111) surfaces showing route to prepare different surface structures and alloys by varying temperature of deposition, coverage and PA. Image from [37].

Composition of the surfaces was examined using XPS. The Rh $3d_{5/2}$ core level peak was observed at 306.9 eV, which was attributed to uncoordinated surface atoms. The ratio between the Rh $3p_{3/2}$ and Pt $4f$ peak was used determine coverage. The ratio decreased upon PA, revealing subsurface diffusion of Rh or enrichment of Pt at the surface.

For a Rh solute in a Pt host, computational modeling indicated no tendency for surface segregation [38]. In another study by Attard et al. [39], Rh films were evaporated onto Pt (111) electrodes, and showed a

(1 × 1) overlayer for all coverages. Upon deposition at T < 400 K, the growth mode was a "pseudo-Frank-van der Merwe", similar to what is known as quasi-2D (Stranski-Krastanov) growth (see section 2.1.3). It also showed a temperature dependent growth of Rh on Pt (111), where substrate temperatures above 400 K resulted in strong deviation from 2D growth by formation of bulk Rh microcrystallites.

### 1.3.3 Rh on Rh(111)

As with Pt, the deposition temperature of Rh on Rh(111) strongly influenced the obtained surface morphology. Tsui et al. [40] published a study on nucleation and growth of epitaxial Rh(111) at high coverages (10.1 ML) (Figure 1.5). Deposition was performed in the temperature range from 375 - 810 K, which showed a transition in morphology at 600 K. The surface features changed from dendritic to compact. Although a transition was seen in the morphology, it was observed that 2D growth remained both below and above the transition temperature. Formation of dendritic islands at lower temperatures has also been reported for Co/Re(0001) [41] and Au/Ru(0001) [42].

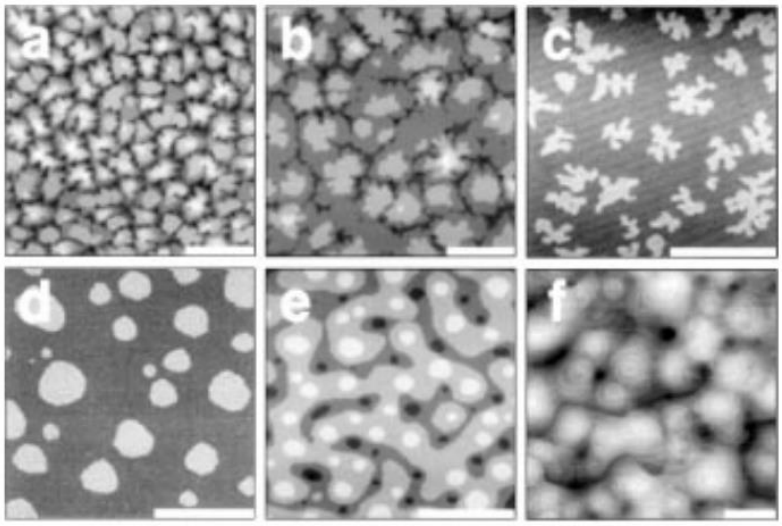


Figure 1.5: STM images of 10.1 ML Rh/Rh(111) at a) 375 K, b) 450 K, c) 530 K, d) 680 K, e) 725 K, f) 810 K. White bar correspond to 40 nm for a) – e), and 100 nm for f). A transition in morphology was observed at around 600 K, where surface structure changed from dendritic to compact. Images from [40].

Máca et al. [43] simulated the inter-layer diffusion of a Rh atom on Rh(111). The study concluded that upon island growth, B-steps will grow faster and hence become shorter, and the resulting islands will have an asymmetric shape with longer A-steps.

### 1.3.4 Pt on Rh(111)

Duisberg et al. [44] studied epitaxial growth of Pt on Rh(111) at 700 K for coverages up to 3.3 ML. Figure 1.6 show STM images of 0.9 and 0.1 ML coverage surfaces with the corresponding height profile. It was shown that Pt forms a surface alloy with Rh by incorporating into the first monolayer, dominating along step edges due to diffusion of Pt. The STM image of 0.9 ML surface reveal a disperse distribution of Pt atoms on the Rh(111) surface. The study also showed that the apparent height of the Rh atoms was higher than Pt atoms in the surface alloy, and that Pt on Rh(111) follow a 2D growth mode. This is in contrast with results obtained by computational modelling indicating surface segregation for Pt in a Rh(111) host [38].

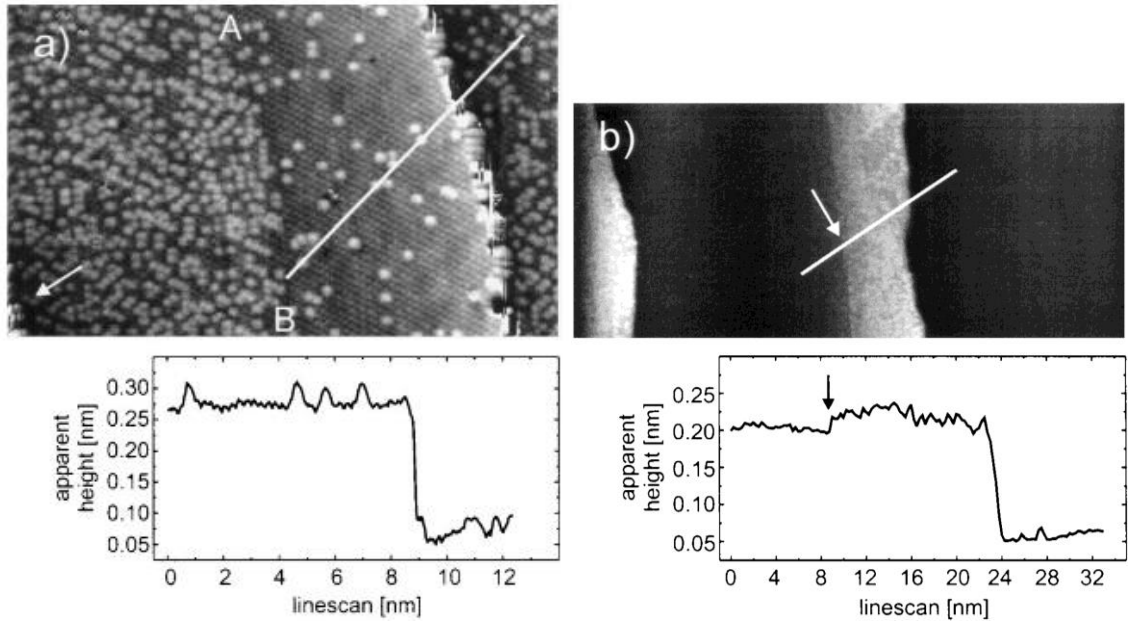


Figure 1.6: a) STM image of 0.9 ML Pt/Rh(111). White bar correspond to height profile below, indicating Rh atoms located higher up than Pt. Scan size 20 × 12 nm. b) STM image of 0.1 ML Pt/Rh(111). White line corresponds to height profile below. The brighter area below the white bar show area with alloyed PtRh at an apparent height of 30 pm above Rh terrace. Scan size 100 × 40 nm. Images from [44].

### 1.3.5 Overview of Pt and Rh systems

An overview of the Pt or Rh on Pt(111) or Rh(111) systems are shown in Table 1.1 It includes the various surface morphologies and growth modes obtained upon varying deposition temperature and coverage (and CO pressure for Pt/Pt(111)). The characterization techniques used are also included.

Table 1.1: Overview of Pt or Rh deposited on Pt(111) and Rh(111), showing island shape and growth based on deposition temperature and coverage. Characterization techniques used are included. A star (*) indicate CO pressure, and is included under temperature column.

| **System** | **Temp., K** | **Coverage, ML** | **Island Shape** | **Growth** | **Characterization Tech.** | **Ref.** |
|---|---|---|---|---|---|---|
| Pt/Pt(111) | 205 | 0.3 | Dendritic | 2D | STM, TEAS | Bott [31] |
| | 425 | | Triangular A step | 3D | | |
| | 628 | | | 2D | | |
| | 425 | 0.8 | | 3D | | |
| | 628 | | | Quasi 2D | | |
| | 205 | 2.4 | Dendritic | Quasi 2D | | |
| | 425 | | Triangular | 3D | | |
| | 628 | | | Quasi 2D | | |
| Pt/Pt(111) | 200 | 0.2 | Dendritic | 2D | STM | Michely [34] |
| | 400 | 0.08 | Triangular A step | | | |
| | 455 | 0.14 | Hexagonal | | | |
| | 640 | 0.15 | Triangular B step | | | |
| Pt/Pt(111) (*) | 400 in $5\times10^{-12}$ mbar | 0.15 | Triangular B step | 2D | STM | Kalff [36] |
| | 400 in $1\times10^{-10}$ mbar | | Hexagonal | | | |
| | 400 in $4.7\times10^{-10}$ mbar | | Hexagonal | | | |
| | 400 in $9.5\times10^{-10}$ mbar | | Triangular A step | 3D | | |
| | 400 in $1.9\times10^{-9}$ mbar | | Triangular A step | | | |
| | 300 | 5 | Dendritic | Quasi-2D | | |
| | 300 in $9.5\times10^{-10}$ mbar | | Dendritic rough | 3D | | |
| | 400 | | Triangular | Quasi-2D | | |
| | 400 in $9.5\times10^{-10}$ mbar | | Triangular rough | 3D | | |

| | | | | | | |
|---|---|---|---|---|---|---|
| Rh/Pt(111) | | 0.2 | Triangular | 3D | STM, XPS, LEED | Zheng [37] |
| | 400 | | Mixed triangular and hexagonal | | | |
| | 450 - 500 | | Triangular | | | |
| | 550 | | Triangular | 2D | | |
| | 600 | | Hexagonal | | | |
| | 700 | | No islands visible | - | | |
| | 300 w/ PA 700 | 0.2 | Hexagonal | 3D | | |
| | 400 w/ PA 700 | | | | | |
| | 500 w/ PA 700 | | | | | |
| | 600 w/ PA 700 | | | 2D | | |
| | 550 | 0.7 | Triangular | 2D | | |
| | 300 w/ PA 550 | >0.9 | Worms | 3D | | |
| Rh/Pt(111) | T<400 | >3 | - | Quasi 2D | Cyclic voltammetry, LEED and AES | Attard [39] |
| | 873 | 0.7 | Microcrystalline bulk Rh | 3D | | |
| Rh/Rh(111) | 375 | 10.1 | Dendritic | 2D | STM, RT-RHEED | Tsui [40] |
| | 450 | | | | | |
| | 530 | | | | | |
| | 680 | | Compact | | | |
| | 725 | | | | | |
| | 810 | | | | | |
| Pt/Rh(111) | 700 | 0.1 | No islands visible. Formed surface alloy. | 2D | STM, AES, UPS, PAX | Duisberg [44] |
| | 700 | 0.9 | No islands. Disperse distribution of clusters. | | | |

### 1.3.6 Oxygen on Pt (111)

A number of oxygen-induced structures form on Pt(111) (Figure 1.7). Gland et al. [45] showed that a molecular phase can be found at temperatures below 160 K, while an atomic phase is found above this temperature, and that oxides form in the temperature range 800 - 1100 K. The atomic phase saturates at a coverage of 0.25 ML and forms a (2 × 2)-O overlayer with oxygen in fcc hollow sites [46-48]. Obtaining chemisorbed structures or oxides with higher coverages can be achieved through the use of higher temperature and pressure [49], atomic oxygen [50, 51], ozone [52], or $NO_2$ [53-55]. It was found that loss of the (2 × 2)-O structure to a subsurface oxide is reversible upon annealing [50].

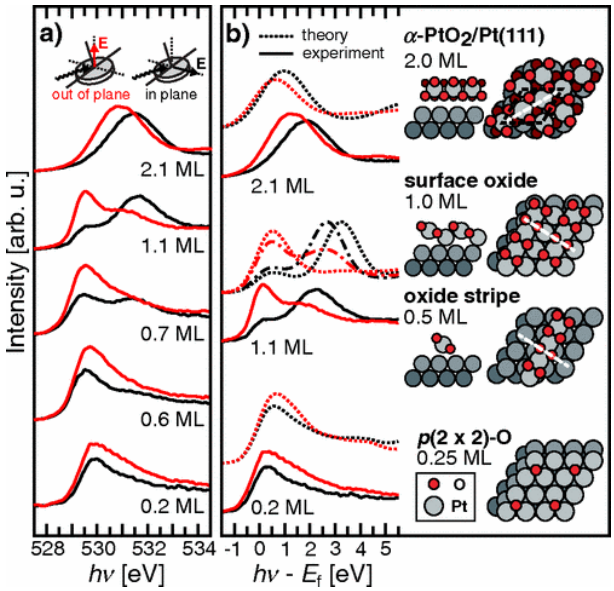


Figure 1.7: Overview of different oxygen induced species on Pt (111), starting with (2 × 2)-O at 0.25 ML, oxide stripes at 0.5 ML, a surface oxide at 1.0 ML, and bulk-like oxide at 2.0 ML. Figure from [56].

From the saturated (2 × 2)-O phase at 0.25 ML and up to about 0.5 ML, the (2 × 2) low-energy electron diffraction (LEED) pattern remains visible, and up to about 0.75 ML, oxygen is found to be chemisorbed on Pt(111) occupying both fcc and hexagonal close-packed (hcp) hollow sites. STM images reveal that chemisorbed oxygen above 0.25 ML form a (2 × 1)-O overlayer structure with domains of rotational degeneracy of three [55]. Once the coverage reaches around 0.4 ML, a Pt oxide chain structure is seen within the domains. Increased oxygen coverages up to about 0.75 ML results in oxide chains forming a network of Y-shaped branches that evolves into a honeycomb structure, and thus oxidation of Pt happens via an oxide chain structure. Upon dozing ozone on Pt(111), it was shown that around 1 ML, there was a change from chemisorbed oxygen to Pt oxide structures on the surface [52]. Another study indicated that around 0.75 ML Pt oxide particles starts to form on Pt(111) [51]. Another study reveal formation of $PtO_2$ nanocluster after high temperature oxidation followed by cooling down in $O_2$ [57].

A few studies using *in-situ* techniques to follow Pt(111) oxidation at *near-ambient* pressure conditions gave different results. One study reported formation of a strongly distorted bulk-like α-$PtO_2$ oxide in 500 mbar $O_2$ at 520 – 880 K [58]. This was in contrast to a study reporting formation of an oxide at similar temperatures, but much lower pressures, and that oxidation proceeded through formation of a PtO-like surface oxide [56]. Our group has previously showed that Pt oxidizes in 1 mbar $O_2$ at 623 K, and below this temperature chemisorbed structures are formed [59]. Fantauzzi et al. [60] reported that prolonged exposure to $O_2$ ($t \geq 4$ h) was needed to form a stable surface oxide. A newer *in-situ* study following the oxidation of Pt(111) under *ambient* conditions and beyond (1 – 5 bar of $O_2$ at ~530 K) reveal no formation of bulk-like α-$PtO_2$, but formation of two other stable surface oxides [61]. In the pressure range 1.0 - 5 bar $O_2$, a spoked-wheel superstructure formed (Figure 1.8) Above 2.2 bar $O_2$ a lifted-row structure with close packed parallel lines formed in co-existence with the spoked-wheel structure. Outside the high pressure regime, the two surface oxides were unstable.

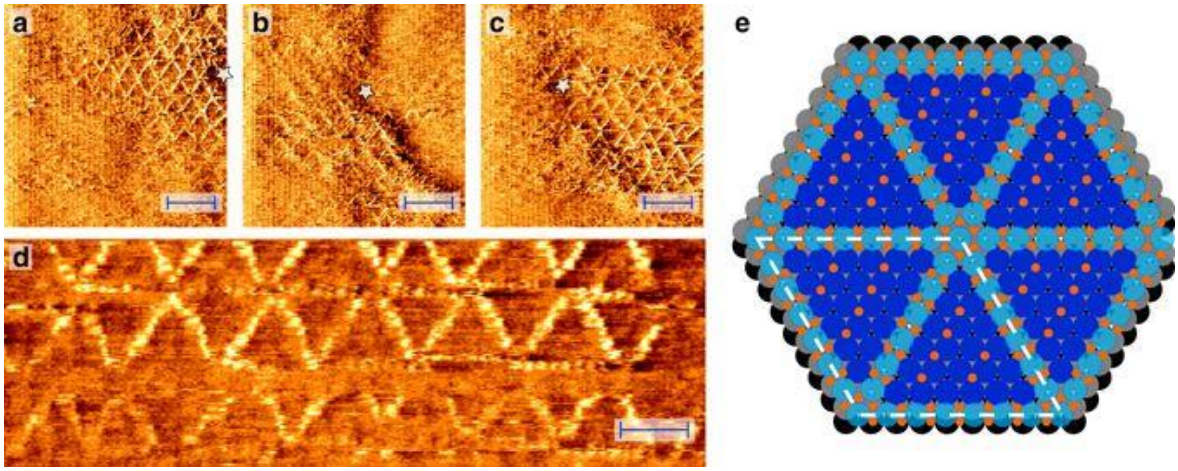


Figure 1.8: Structure of spoked-wheel surface oxide at 1 bar $O_2$ at 529 K. a)-c) Scale bar corresponds to 4 nm. d) Scale bar corresponds to 2 nm. e) Ball model of spoked wheel structure, where light blue corresponds to oxidized Pt, and dark blue, grey and black to Pt surface. Orange corresponds to oxygen. Figure from [61].

### 1.3.7 Oxygen on Rh (111)

A variety of oxygen-induced structures can be observed on Rh(111) when varying the oxygen pressure and temperature (Figure 1.9). The structure with the lowest coverage is a (2 × 2)-O overlayer (Figure 1.9 a)) with atomic oxygen in three fold hollow fcc sites and a coverage of 0.25 ML [62-65], similar to what is observed on Pt(111) [47]. By increasing the $O_2$ pressure, a (2 × 1)-O chemisorbed structure forms (Figure 1.9 b)) [63, 65, 66], with a coverage of 0.5 ML and all oxygen atoms in fcc sites. Dosing $O_2$ at higher temperatures result in a $\left(2\sqrt{3} \times 2\sqrt{3}\right)$R30 chemisorbed structure (Figure 1.9 c)) [67]. Oxygen atoms are located in both fcc and hcp sites with a total coverage of 0.67 ML. The structure is kinetically stabilized in the temperature range 400 - 700 K and at $1 \times 10^{-3}$ mbar oxygen. Above these

conditions, a surface oxide forms, as will be described later. In co-existence with the $(2\sqrt{3} \times 2\sqrt{3})$R30 structure, it is shown that a (2 × 2)-3O structure forms [67] (Figure 1.9 d)). This structure has a coverage of 0.75 ML with all oxygen atoms in fcc sites, but has been shown to have a short lifetime [63].

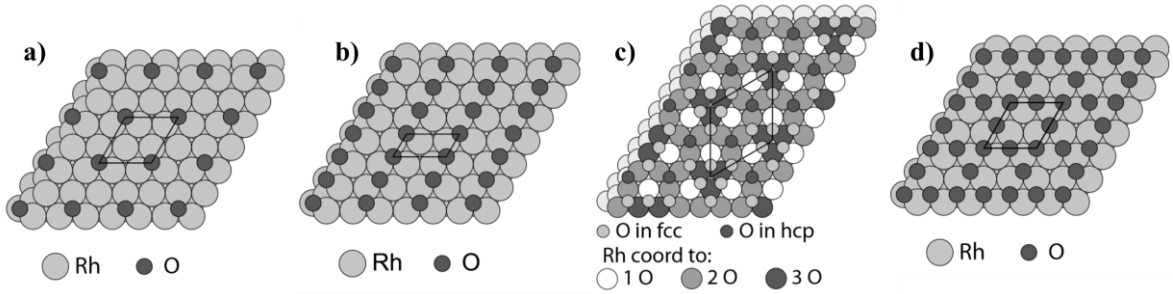


Figure 1.9: Oxygen-induced structure on Rh(111) starting with a) (2 × 2)-O structure, b) (2 × 1)-O structure, c) $(2\sqrt{3} \times 2\sqrt{3})$R30 structure, an d) (2 × 2)-3O structure. Adapted from [63].

Growth of an ultra-thin $RhO_2$ surface oxide with a (9 × 9) overlayer structure (Figure 1.10 a)) starts in the temperature and pressure range 700-800 K and $2 \times 10^{-4} - 1 \times 10^{-3}$ mbar [63, 68]. The growth is initiated at step edges due to easier penetration of oxygen compared to the terraces. The surface oxide on the hexagonal Rh(111) substrate result in a moiré pattern that can be seen by means of LEED and STM (Figure 1.10 b-c)) [68-70]. Upon surface oxidation, STM images reveal formation of Rh ad islands [63]. This is due to a decrease in Rh density for the surface oxide structure compared to bulk Rh.

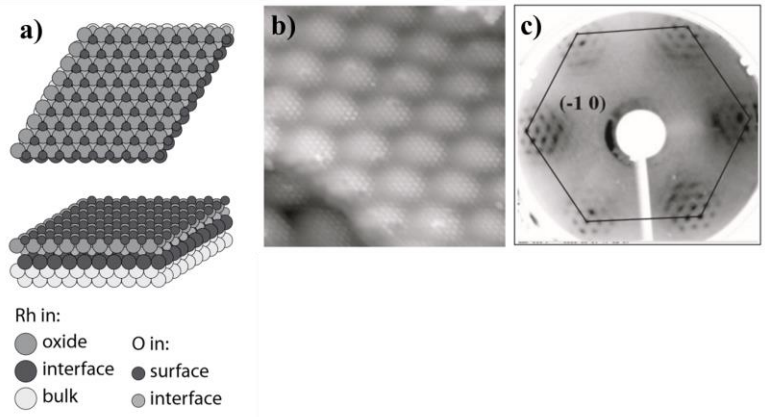


Figure 1.10: Illustration of (9 × 9) RhO2 surface oxide on Rh(111). b) STM image revealing that surface oxide forms a moiré pattern, where white dots show oxygen atoms and larger dots indicate moiré pattern. c) Moiré pattern obtained by LEED. Adapted from [71] and [62].

Due to kinetic hindrance, the $RhO_2$ surface oxide is stable up to about 1 mbar $O_2$ [68]. To study the oxidation of Rh(111), *in-situ* surface X-ray diffraction (SXRD) measurements were performed while increasing pressure and temperature [63]. In 1 bar $O_2$ at 548 K, formation of a bulk-like oxide starts. Temperature and pressure increase resulted in formation of a well-ordered $Rh_2O_3$ bulk oxide, taking the corundum structure. It has also been shown that by using atomic oxygen it is possible to grow a bulk-

like oxide film of $Rh_2O_3$ terminated with a (0001) facet on Rh(111) [69], that can co-exist with the $RhO_2$ surface oxide. A recent study by Farber et al. [70] showed that the thermodynamically stable oxygen induced phases on Rh(111) after deposition of atomic oxygen are the (2 × 1)-O adsorbed structure and the $RhO_2$ surface oxide. An overview of the expected oxygen-induced structures are depicted in Figure 1.11, both from density functional theory (DFT) calculations in a) and from experimental results in b).

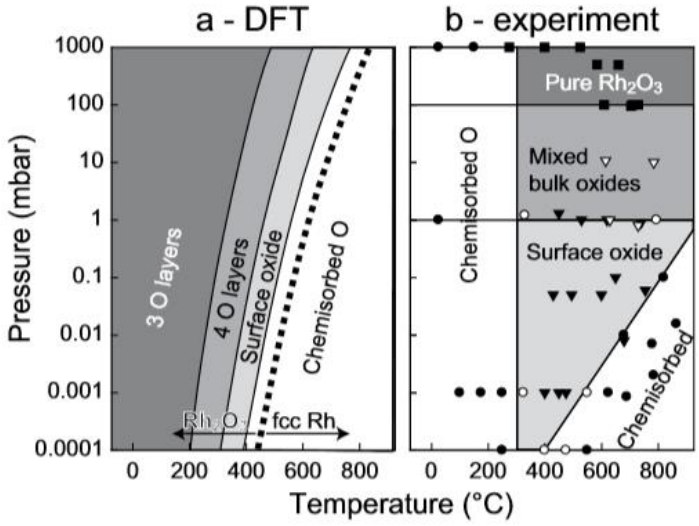


Figure 1.11: Overview of the expected oxygen-induced species on Rh(111) at various pressures and temperatures based on a) DFT calculations, b) experiments. Figure from [63].

A way of identifying the oxygen-induced structures on Rh(111) is by means of XPS. O 1*s* and Rh $3d_{5/2}$ spectra of the various oxygen-induced structures is shown in Figure 1.12. The bulk Rh $3d_{5/2}$ component is expected at a binding energy of approximately 307.1 – 307.3 eV [63, 67, 69, 71], while uncoordinated Rh surface atoms are found at -0.52 eV relative to the bulk component [63]. Among the chemisorbed structures, Rh can be coordinated to one, two or three oxygen atoms, which Gustafson et al. have reported to give a component at 307.0 eV, 307.5 eV and 307.86 eV, respectively [63]. The (9 × 9) surface oxide give rise to two new components corresponding to Rh in the oxide at +0.79 eV, and Rh in the interface at -0.22 eV, relative to the bulk component [68]. The bulk-like $Rh_2O_3$ (0001) surface show presence of a component at +1.04 eV relative to bulk [69].

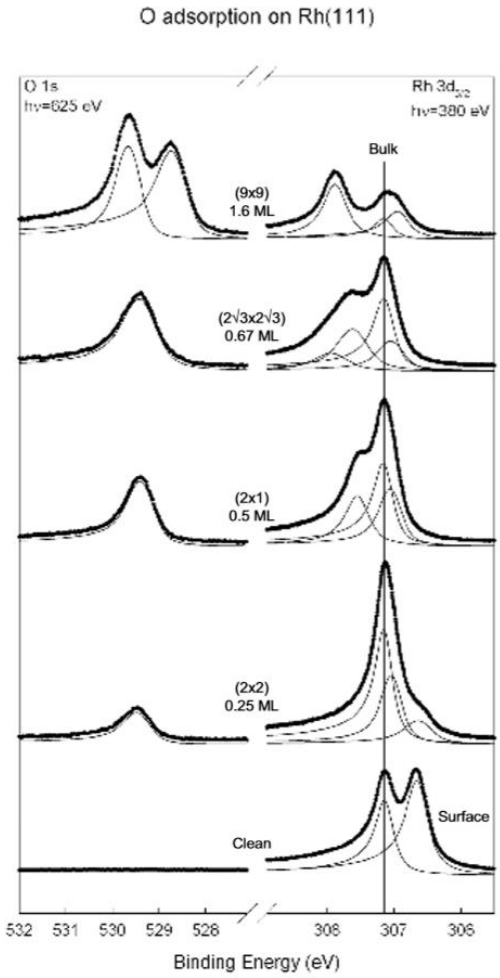


Figure 1.12: Overview of XP spectra of O 1*s* and Rh 3$d_{5/2}$ peak for oxygen-induced structures on Rh(111). Adapted from [63].

### 1.3.8 Overview of Pt(111) and Rh(111) Exposed to Oxygen

An overview of the oxygen-induced structures on Pt(111) and Rh(111) is displayed in Table 1.2. The oxygen coverage, overlayer structure, and temperature and pressure upon dosing is presented. If not stated otherwise, molecular $O_2$ was used as oxygen source. In addition, the characterization techniques used are listed.

Table 1.2: Overview of oxygen-induced structures on Pt(111) and Rh(111). When other oxygen sources than molecular $O_2$ is utilized, the source is stated under "Dosing Pressure" column.

| System | Coverage, ML | Overlayer Structure | Dosing Temp., K | Dosing Pressure | Characterization | Ref. |
|---|---|---|---|---|---|---|
| **$O_2$ on Pt(111)** | - | Molecular $O_2$ | < 120 | 5 L | EELS, TDS, UPS | Gland [45] |
| | 0. 25 | (2 × 2)-O | 150 – 500 | 5 L | | |
| | 0.25 | (2 × 2)-O | 300 | $5\times10^{-7}$ Torr for 15 min | LEED | Joebstl [46] |
| | 0.6 – 1 | Chemisorbed | 570 | $10^{-3}$ Pa for 300 s | XPS, TPD | Derry [49] |
| | 0.25 | (2 × 2)-O | 300 | 5 L (Atomic O) | XPS, CAICISS, LEED | Parkinson [50] |
| | - | Subsurface oxide | 300 | 50 L (Atomic O) | | |
| | 0.75 | Chemisorbed | 400 | - ($NO_2$) | AES, LEED, UPS, HREELS, TPD | Parker [53] |
| | < 0.75 | Chemisorbed | 450 | - (Atomic O) | TDP, XPS, EELS, LEED | Weaver [51] |
| | 0.75 - 2.9 | Pt oxide | 450 | | | |
| | 1.2 - 2.4 | Pt oxide particles | 300 | 20 L (Ozone) | TPD, AES, LEED | Saliba [52] |
| | 0.25 – 0.4 | (2 × 1)-O | 573 | - ($NO_2$) | TPD, STM | Devarajan [55] |
| | 0.4 – 0.75 | Pt oxide chains on (2 × 1)-O | 450 | | | |
| | - | α-PtO2 nanocluster | 1250 – 1350 cooled to 300 | $5 \times 10^{-5}$ mbar for 5 – 30 min | STM, LEED | Krasnikov [57] |
| | 2 | α-$PtO_2$ | 520 - 880 | 500 mbar | SXRD, XRR | Ellinger [58] |
| | 0.5 – 1.1 | PtO surface oxide | 420 - 620 | 0.5 Torr | XPS, XAS | Miller [56] |
| | 2.1 | α-$PtO_2$ | 720 | 5 Torr | | |
| | - | Surface oxide | 300 – 650 | 1 mbar for 265 – 430 min | NAP-XPS | Fantauzzi [60] |
| | - | Surface oxide (spoked-wheel) | 530 | 1.0 - 5 bar | STM | van Spronsen |

| | | | | | | |
|---|---|---|---|---|---|---|
| | - | Surface oxide (lifted-row) | 530 | 2.2 - 5 bar | | [61] |
| **$O_2$ on Rh(111)** | 0.25 | (2 × 2)-O | 300 | 0.6 L | LEED | Wong [64] |
| | 0.25 | (2 × 2)-O | 273 | 0.7 L | LEED | Schwegmann [62] |
| | 0.25 | (2 × 2)-O | 320 cooled to 60 | 1.5 L | STM, LEED | Marchini [65] |
| | 0.5 | (2 × 1)-O | 300 | 30 L | | |
| | 0.5 | (2 × 1)-O | - | 20 L | LEED, MPRI | Reimann [66] |
| | 0.67 | $(2\sqrt{3} \times 2\sqrt{3})R30$ | 400, or 550 cooled to 400 | $1 \times 10^{-3}$ mbar for 300 s | HRCLS, STM, DFT | Köhler [67] |
| | 0.75 | (2×2)-3O | | | | |
| | - | $RhO_2$ surface oxide | 700 | $1 \times 10^{-3}$ mbar | HRCLS, LEED, STM, DFT | Gustafson [63] |
| | - | $RhO_2$ surface oxide | 800 | $2 \times 10^{-4}$ - 10 mbar | HRCLS, LEED, STM, DFT | Gustafson [68] |
| | . | Bulk $Rh_2O_3$ | 800 | 500 mbar | | |
| | - | $RhO_2$ surface oxide | 723 | $5 \times 10^{-7}$ mbar for 10 min (Atomic O) | HRCLS, LEED, STM, DFT | Blomberg [69] |
| | - | Bulk oxide film $Rh_2O_3$ (0001) | 653 | $5 \times 10^{-7}$ mbar for 60 min (Atomic O) | | |

## 1.4 Motivation

In the NAFUMA research group at Department of Chemistry, UiO, we have a long tradition in synthesizing or grow new functional materials in form of coatings, powders (nm-µm range) and single crystals. The new materials are subsequently explored in terms of atomic arrangement, chemical and physical properties to achieve fundamental insight with potential relevance for technology. The last few years, the NAFUMA research group has also moved in a direction of taking use of surface sensitive tools as STM and XPS as well as high resolution TEM, with the ambition to operate these techniques at the conditions the materials are intended to be used at, for example within catalysis. Concretely, the NAFUMA group invested in a Reactor STM in 2016, which can be operated up to 6 bar and 575 K, and that is optimized to withstand the corrosive $NH_3$-based chemistry. Further, for decades the NAFUMA group have collaborated with Yara International and K. A. Rasmussen on ammonia-based chemistry, and last years, the partners have focused on chemistry connected to ammonia oxidation for both $HNO_3$ production and NOx abatement with funding via the SFI center iCSI (https://www.ntnu.edu/icsi).

In this MSc project, our motivation is to utilize surface sensitive techniques to understand the role of how elemental mixing and morphology of bimetallic Pt-Rh alloyed surfaces affects interaction with oxygen. In order to reach this goal we will focus on the two complementary mirror systems; Pt deposited on Rh(111) and Rh deposited on Pt(111), and systematically collect lacking data from both systems to gain new insight. We will combine STM, XPS and LEED, operated at UHV, with NAP-XPS and Reactor STM operated in variable oxygen atmospheres ($10^{-3}$ mbar – 1 bar).

In the first part, we will apply a systematic approach for preparing surfaces with well-defined Pt-Rh nanostructures by depositing Pt on a Rh(111) single crystal and create a synthesis strategy roadmap. Preparation parameters as deposition temperature, post-annealing time and temperature as well as coverage (ML Pt deposited) will be systematically varied in order to describe growth pattern and morphology. Surfaces will be characterized utilizing LEED and STM at UHV. Obtained findings will be correlated to the corresponding findings already reported for the inverse system, Rh deposited on Pt(111) [37].

In the second part we aim to harvest and analyze XPS and NAP-XPS (in oxygen) data obtained at Hippie MAX-IV for surfaces where Rh is deposited on Pt(111) following recipes already established and published elsewhere [72]. The motivation behind this activity is to expand the reported synthesis roadmap for the preparation of Rh/Pt(111) surfaces as well as achieving insight into differences in oxide structures reached due to variable extent of Pt-Rh alloying.

Finally, the third interesting aspects of this project is to clarify, by means of Reactor STM, how tuning degree of Pt alloying of Pt/Rh(111), can alter oxidation of the surface and how oxygen pressure range spanning over 6 orders of magnitude leads to different oxidation results. In particular, the findings will be correlated to oxide structures reported for Rh(111) in low pressure oxygen ($pO2 = 1 \times 10^{-3}$), and the spoked-wheel structure reported for Pt(111) at 530 K and pO2 = 1 bar [61].

# 2 Method and Theory

In this chapter, some of the relevant theory of surface structures and preparation of surfaces is described. In addition experimental techniques used in this project are described in section 2.3.

## 2.1 Surface Structure

Solids like metals and oxides are typically crystalline, meaning that they have a periodic atomic arrangement. A crystal structure can be described by its crystal lattice and a basis [73] (p. 4). A lattice is a mathematical concept describing an infinite array of points, and the basis is a group placed on each lattice point, typically an atom, a group of atoms or a molecule. The unit cell is defined as the smallest repeating unit of the crystal structure, and is described by basis vectors **a, b** and **c.** A large group of metals, including Pt and Rh, have a fcc (also known as cubic close-packed (ccp)) lattice. The fcc structure has a stacking sequence of ABCABC (Figure 2.1 a)) and is one of two structures with the densest packing of spheres [73] (p. 16). The other is the hcp with stacking sequence ABABAB.

Planes in a crystal are described by Miller indices, *h*, *k* and *l* [74] (p. 106). When written in brackets (*hkl*) they represent the set of all parallel planes. The values *h*, *k* and *l* correspond to the reciprocal values of the fraction where the plane intersect with the unit cell edges, *a*, *b* and *c*, respectively. A Miller index of 0 then corresponds to a plane parallel to the cell edge. For the fcc structure, the (111) plane is the closest packed plane [73] (p. 16) (Figure 2.1 b)), and it is the most stable plane followed by (110) and (100). On the fcc(111) surface, two types of straight steps can be found; A steps having (100) microfacets, and B steps having (111) microfacets (Figure 2.1 c)) [75].

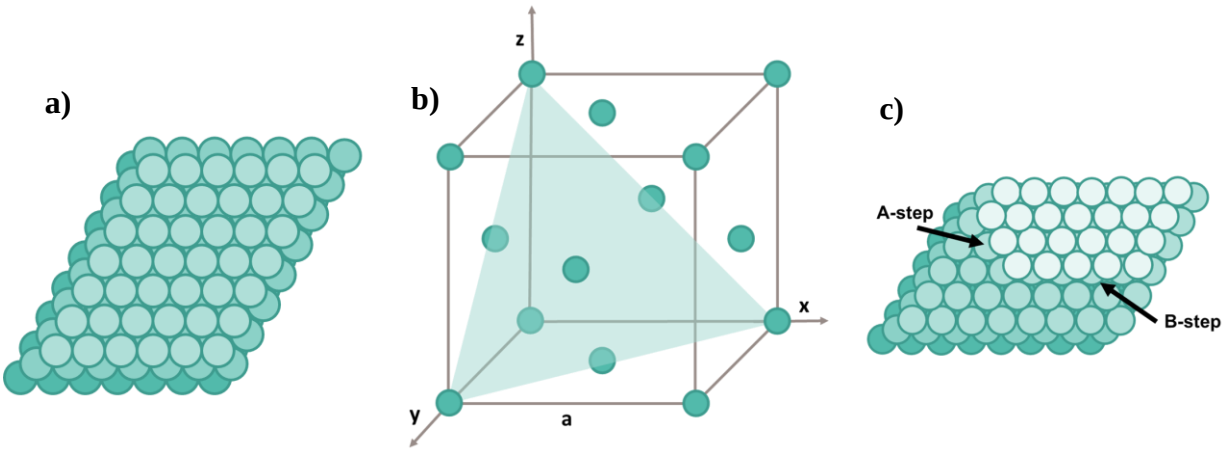


Figure 2.1 a) Top view of atoms stacked in the fcc (ccp) structure. b) (111) plane in the fcc unit cell. c) Top view of (111) surface displaying A-step and B-step.

A surface or an interface is defined as an area where there is an abrupt change in the system properties [76] (p. 3). An abrupt change can indicate change in aggregation state, symmetry, crystal structure or chemical composition. The interfaces considered here are solid-gas interfaces, where the solid is a crystal with well-defined structure. For the outermost atoms of the solid, relaxation will occur resulting in a slight change in spacing relative to the bulk phase [76] (p. 16). The bonding of the surface atoms will differ from the bulk, which will alter the electronic and chemical properties at the surface [77] (p. 3). When discussing surface structures, we can make a division been structure of clean surfaces and of surfaces with adsorbates [77] (p. 9), as will be discussed further in section 2.1.1 and 2.1.2.

### 2.1.1 Clean Surface Structure

To simplify the study of surfaces and their interactions with molecules, crystals are often cut along a specific crystal plane. In our case, metal surfaces of Rh and Pt were cut in the (111) direction. However, even the single-crystal surface will not have a completely flat closed-packed structure. Some defects (increase in entropy) will naturally be incorporated to the surface in order to stabilize it [6] (p. 39). The crystal surfaces are described with the terrace-ledge-kink-model (TLK) [78], and consist of step-like discontinuities made up of terraces and steps-edges (ledges) with kinks, as illustrated in Figure 2.2. In addition, point defects such as adatoms and vacancies can occur.

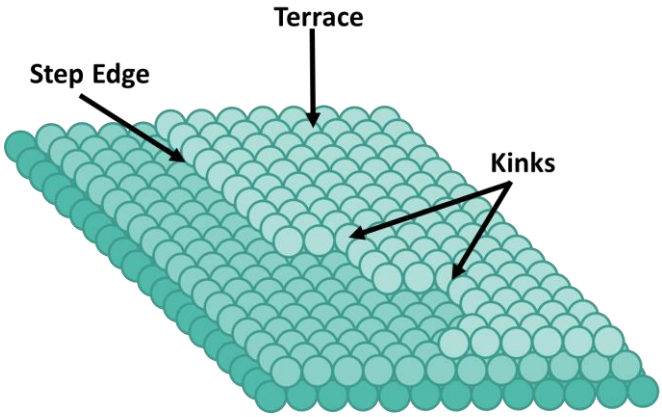


Figure 2.2: Illustration of a clean crystal surface with step edges, kinks and terraces.

The atoms located at step edges and kinks experience different surroundings compared to atoms on terraces, hence their electronic properties and chemical reactivity will differ [3] (p. 183) [77] (p. 14). The atomic structure of a surface can dictate the rate of a reaction since step edges and kinks can act as active sites in catalytic reactions [3] (p. 171). An example of this is the high reaction rate for the iron (111) and (211) faces, compared to the (100), (210), and (110) faces due to presence of distinct sites in the (111) and (211) surfaces [3] (p. 177). In addition, the surface will try to minimize the energy of the defects by spreading out the electrons in a way that smoothens the step. This is known as Smoluchowski smoothing [79].

### 2.1.2 Adsorbate Structure

Upon exposing a clean crystal surface to air or by evaporation of a species, atoms will absorb to the surface, which results in changes of the surface properties [63]. Depending on the bonding type between the substrate and the adsorbed species, we distinguish between *physisorption* and *chemisorption*. In physisorption there is no change in the electronic structure upon absorption, and weak bonds like van der Waals interactions or hydrogen bonds occur. For chemisorption substantial changes in the electronic structure occur and stronger bonds, typically metallic, covalent or ionic, form. $O_2$ adsorbs on most metals by chemisorption, and due to the strong bonding to the substrate, the intra-molecular forces in $O_2$ are weakened, and the oxygen molecule dissociate [63]. If the adsorbed species form a condensed phase on the substrate, it is referred to as heterogeneous nucleation [76] (p. 294). The nucleation site of adsorbents depend on several parameters such as deposition temperature and deposition rate. At higher temperatures, the adatoms have increased mobility which allows them to diffuse to the low-energy sites. High concentrations of impurities can lead to lower mobility, as these may act as pinning sites for the adatoms [80].

The symmetry of the adsorbents relative to the underlying surface can be random, commensurate or incommensurate [77] (p. 22-23). Wood's notation is used to describe ordered absorbent structure relative to the substrate structure. The substrate structure is defined by unit cell vectors $a_1$ and $a_2$, and the unit cell vectors of the two-dimensional overlayer is described relative to $a_1$ and $a_2$. If the unit cell of the overlayer is rotated relative to the substrate, this is also indicated by including the rotation angle [81] (p. 64-65). Figure 2.3 a) shows an example of a unit cell with a (2 × 2) reconstruction. If the surface structure has a different structure than the substrate, it is often referred to as a superlattice [6] (p. 44). As illustrated in Figure 2.3 b), adsorbed atoms on the (111) surface plane can be placed on an fcc or a hcp site. If the adatom is placed on a hcp site, the adatom is placed right above the atom in the second layer of the substrate, following an ABAB stacking. If the adsorbed atom is placed on a fcc sites, the stacking sequence follows an ABC pattern [5].

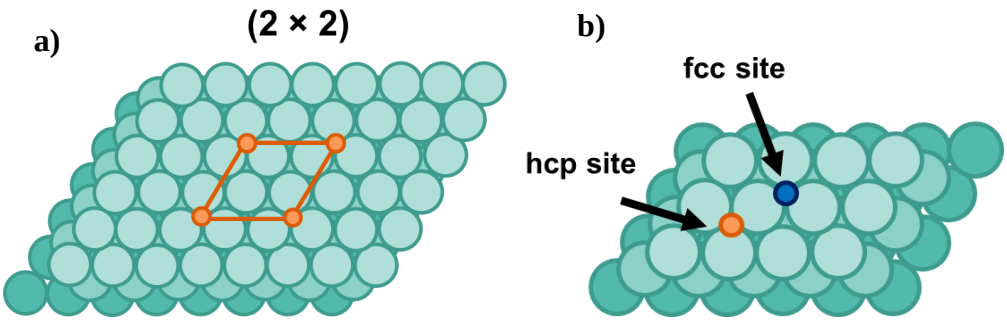


Figure 2.3: a) Adsorbate in orange with (2 × 2) overlayer structure on the (111)-plane. b) Illustration of hcp and fcc site for an adsorbate on a (111) surface.

### 2.1.3 Metal on Metal Surfaces

When depositing metal on a metal substrate, most metals form an (1 × 1) overlayer on the substrate [6] (p. 60). The deposited metal structure matches that of the substrate structure and uses it as a template, and this is referred to as epitaxial growth. Deposited metals can also form alloys under appropriate conditions by interdiffusion. Interestingly the surface alloy phase can be ordered, while the corresponding metals can have a lack of long-range ordering in the bulk phase [6] (p. 60).

The deposited metal will typically grow in one of three modes. The first one is two-dimensional (2D) growth (or layer-by-layer growth, or Frank-van der Merwe growth) where each monoatomic layer will be completed before a new layer starts to grow (Figure 2.4 a)). The second mode is the three-dimensional (3D) island growth (or Volmer-Weber) growth where island formation occur from the start of deposition (Figure 2.4 c)). The third growth mode is an intermediate mode between these two, called quasi-2D growth (Stranski-Krastanov), where growth of a new layer will start before the preceding is fully grown (Figure 2.4 b)) [6] (p. 60).

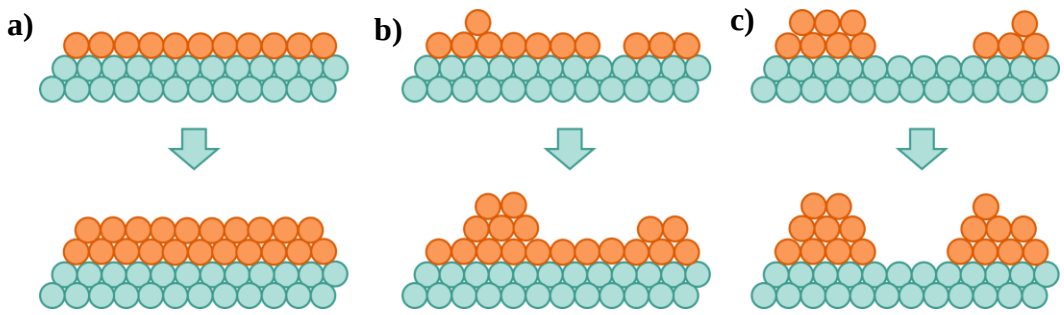


Figure 2.4: Growth modes for deposition of metal on a metal substrate. a) 2D growth, b) quasi-2D growth, c) 3D growth.

## 2.2 Preparation of Surfaces

### 2.2.1 Cleaning of Single Crystals

As previously mentioned (section 1.1) single crystal surfaces are used as model catalysts to facilitate the fundamental studies of how the catalyst behaves. For this, low contamination levels and well-ordered surfaces are required. After production, the single crystal surface looks perfectly flat and clean at macroscopic scale. However, the surface is still considered rough at microscopic scale and may have high contamination levels. In order to obtain a properly clean and flat crystal surface, a number of cycles of sputtering and annealing is performed.

Sputtering is the process of bombarding the sample surface with energetic particles [82] (p. 1). It changes the surface morphology by roding it and removing surface atoms. It has been shown that using noble gas ions, such as Ar+, in the energy range from 100 eV to a few keV, smoothens out the surface. If the energy of the ions is above a few keV, however, defects such as grain boundaries, pyramids, etch pits and steps can be formed. Hence, the energy of the ions is an important parameter to obtain the right surface structure [82] (p. 5).

After sputtering, the surface is annealed to flatten it out. The metal is heated up to a high temperature, usually about 1/3 of the melting temperature. It is kept at the high temperature for a certain time, before cooling down. It results in decrease in dislocation density, and hence releases lattice strain energy and brings the crystal to a more perfect state [83]. These processes require high energy to overcome the activation barrier for diffusion of atoms. Since the diffusion of atoms is facilitated by the high temperature, impurity atoms will also more easily diffuse to the surface, which then can be sputtered away in the subsequent sputtering cycle. In addition, introduction of oxygen at high temperature will drive carbon species up which then are removed by reacting with the oxygen.

### 2.2.2 Deposition of Metal

Metal is deposited onto the single crystal surface by using an electron beam evaporator (EBE). EBE is a type of physical vapor deposition (PVD) where metals are evaporated in vacuum and deposited on a substrate [84]. An electron beam is formed by heating a tungsten filament, which then hit the target material. The target material is typically in a crucible or the tip of a metal rod. Rods are typically used for materials with high melting temperature [84]. The EBE can have multiple pockets, and some EBE can be operated in a manner that several materials can be evaporated simultaneously. The energy transfer from the electron beam to the target material results in evaporation of the metal. The metal vapor is directed towards the substrate where it deposits to create a film. The system is simultaneously cooled with water. [85] (p. 206-208)

### 2.2.3 Oxidation of Surfaces

As previously mentioned (section 1.1 and 1.3), many catalysts have an oxide as support material, or the active component of the catalyst is an oxide. Hence it is useful to be able to form these oxide phases to get a better understanding of the catalysts. In order to form a surface oxide on a single crystal, the surface is exposed to increased partial pressures of oxygen through a leak valve. Higher temperature will facilitate the process, but the required pressure and temperature depends on the material. An example is formation of an $Al_2O_3$ film on a NiAl single crystal. Mom and coworkers prepared and studied Re and

Co-Re metallic nanoparticles on an $Al_2O_3$/NiAl support where the alumina film was grown through oxidation cycles of NiAl to $5\times10^{-6}$ mbar $O_2$ at 600 K for 10 min [8]. This resulted in a 5 Å thick $Al_2O_3$ film. Although $Al_2O_3$ is an insulator, which would complicate the study for UHV techniques like STM and XPS, the film thickness of only 5 Å allows for sufficient electrical conductivity. One should be aware of possible bulk oxide formation at high oxygen pressures or at high substrate temperatures [63].

## 2.3 Characterization

The main work of this thesis is centered on preparation of nanostructures and their characterization by surface sensitive tool, such as STM and XPS. Therefore, these techniques are thoroughly described in the following. In addition, a brief introduction to LEED and mass spectrometry (MS) is given.

### 2.3.1 Scanning Tunneling Microscopy

The primary characterization technique used in this thesis is scanning tunneling microscopy. The STM was first introduced in 1982 by Binning, Rohrer, Gerber and Weibel [86]. They received a Nobel Prize in physics for their pioneering work in 1986 [87], and STM has since then been a well-established characterization technique in surface science.

#### 2.3.1.1 Principles

The technique is based on tunneling of electrons. At the atomic scale an STM consists of an atomically sharp metal probe that is scanned so close to a conducting surface that there is an overlap in wave functions and electrons can tunnel across a potential barrier as shown in Figure 2.5 [88] (p. 12). By applying a bias voltage $V_b$ between the sample and tip, the electrons will tunnel in one direction creating a current referred to as the tunneling current $I_t$. The outstanding high resolution of STM is a result of the exponential dependency of the tunneling current $I_t$ onto distance $d$ between tip and sample surface, given by equation 2.1:

$$I_t \propto eV \exp(\kappa d) \qquad 2.1$$

$\kappa$ is a constant depending on the material of the surface. Small changes in the tip-sample distance results in large changes in the tunneling current, which usually has a value between 10 pA and 10 nA [89] (p. 167).

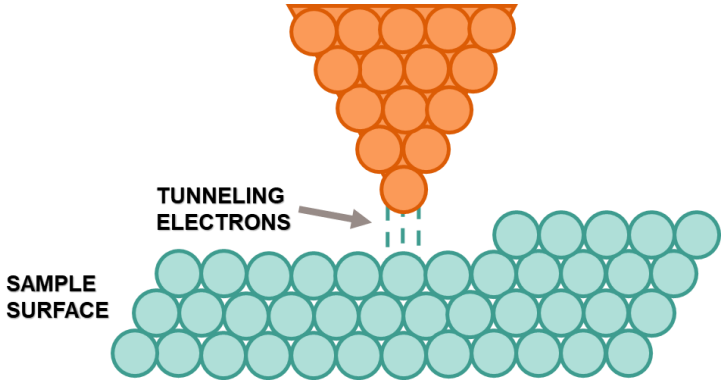


Figure 2.5: Principle of STM with an atomically sharp tip scanning above a sample surface at a small distance allowing electron tunneling.

By changing the sign of the applied bias one can determine the direction of the electron flow [77] (p. 66). A negative sample bias will cause electrons to tunnel from the sample to the tip, while with a positive sample bias tunneling will occur from the tip to the sample. This is illustrated in Figure 2.6.

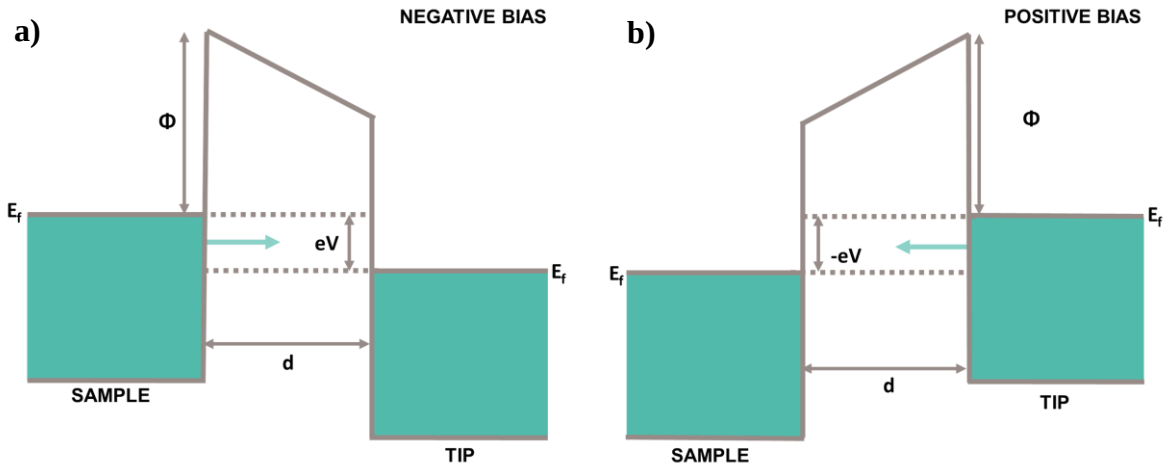


Figure 2.6: Illustration of energy levels of sample and tip upon applying bias voltage. The sign of the voltage determine the direction of the tunneling current indicated by the arrow. a) With negative sample bias electrons tunnel from sample to tip. b) With positive sample bias electrons tunnel from tip to sample. Illustration based on figure from [77] (p. 65).

By measuring the tunneling current as a function of movement in x and y direction one can map out the local density of states (DOS) [88] (p. 12). Since the DOS is correlated to the position relative to nuclei, the image will give position of atoms [77] (p. 66). Therefore, an STM image will also provide topographical information of a sample, and show terraces, step edges and islands on a crystal surface. Advances during the last decades have made it possible to achieve vertical and lateral resolution of images in the sub-Å range [90] (p. 563), [77] (p. 66).

#### 2.3.1.2 Instrumentation

A schematic illustration of the STM instrument and its main components is presented in Figure 2.7. As previously mentioned, the STM instrument has an atomically sharp probe typically made of W or Pt-Ir alloys with its apex facing the sample. The probe is attached to a scanner with a positioning system consisting of three orthogonal piezoelectric tubes that contract and extend according to the scanning voltage. This determines the position of the probe relative to the sample, and the scanner needs an accuracy of 1 pm to obtain atomic resolution [89] (s. 165). Tunneling currents below the order of nA can be detected by a current amplifier, and the signal from the current amplifier is processed in a computer system to generate a STM image.

In order to obtain high resolution images the instrument need a vibration isolation system to remove disturbance from its surroundings. Isolation is commonly done by mounting the instrument on springs or air-damped feet. Sound isolation can be done by using an isolation box around the STM head. In principle, the STM can work in both liquid and gas atmospheres, still the working environment should be somewhat controlled. This is to avoid contaminations on sample and tip, surface oxidation or temperature fluctuations that can cause structural contraction or elongation on atomic scale. Therefore, most STMs operate in UHV with pumping systems, and at a controlled temperature. Low-temperature scanning ensures less thermal drift, but to image surfaces under more realistic conditions, temperatures at RT and above is preferred. [91] (p. 8-9), [89] (p. 165 – 168).

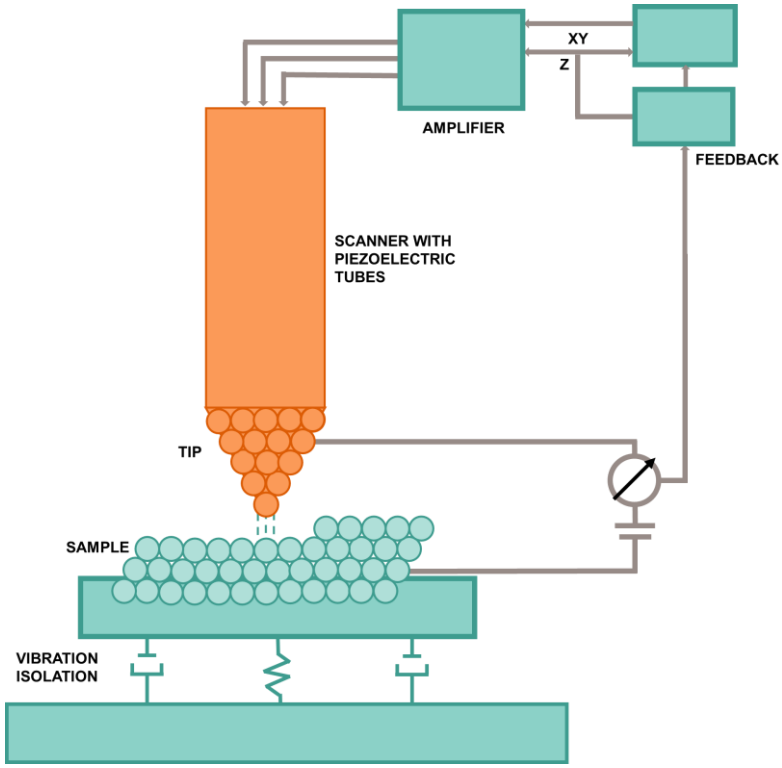


Figure 2.7: A schematic illustration of the STM instrument with its main components. Illustration based on figure from [92].

#### 2.3.1.3 Operational Modes

The STM can be operated in a number of modes. The most common mode for operating the STM is the *constant current mode* [93] (s.302). Here the current is kept constant, while the distance between the tip and the sample is varied to keep a fixed current value. A feedback loop is used to adjust the height of the probe to maintain a constant tunneling current [91] (p. 8). This mode usually gives quite accurate topographical images [89] (p. 168). The other imaging mode in STM is the *constant height mode*. In this mode the tip scans at a constant height above the surface, while the current varies due to changes in density of states. It allows for scanning at higher rates and is used to study dynamic processes. A requirement when working in the constant height mode is to use atomically flat surfaces, since a step edge will cause tip-sample distance to increase by several Å. Also, the chance of crushing the tip is fairly high, so precautions have to be taken [93] (p. 303). Intermediate speed for STM is typically 10 frame/s with a pixel resolution of 100 × 100, while high-speed STM has a rate of 10 frame/s with a resolution of 256 × 256 pixels [94]. To capture dynamic processes on STM, video-rate scanning can be performed, where the scanning rate must be a minimum of 25 frames/s for 256 × 256 pixels.

The *spectroscopic mode* can be used to measure electronic structure, and is also known as scanning tunneling spectroscopy (STS) [77] (p. 67). The STM image depend not only on the topography, but also on the bias voltage applied. One can measure current *I* versus voltage *U* simultaneously as the position on the surface to get images of the local density of states. The fourth mode is *manipulation mode*. In this mode, atoms on the surface can be removed or relocated. In vertical manipulation, the adatom is attached to the tip and pulled up from the surface, and then moved to another location through voltage pulses. When performing lateral manipulation, the adatom stays on the surface while being moved by the tip. [89] (p. 168-169).

#### 2.3.1.4 Image Interpretation

Some obstacles can complicate the interpretation of STM images. Firstly, it is important to ensure that the instrument is calibrated with respect to the length scale in both x-y and in z-direction. For calibration in x-y direction, highly oriented pyrolytic graphite (HOPG) or order grids can be used. Calibration in z-direction is slightly more challenging, and one of the preferred technique is to use single atomic stepped gold samples, but also HOPG can be used here [88] (p. 47). STM images show the surface topography, but since it is the density state that is probed, the images may be altered by the bias voltage. An example of this is the effect of changing the sign of the bias voltage. An adsorbed oxygen atom on n-type GaAs (111) may look like a protrusion or depression depending on the sign as shown in Figure 2.8 a)-b) [95]. Possible formation of Moiré patterns should be taken into account when studying surfaces with a film

on the substrate with different structure or orientation. A Moiré pattern is formed when two periodic structures are superimposed, creating a third pattern, shown in Figure 2.8 c).

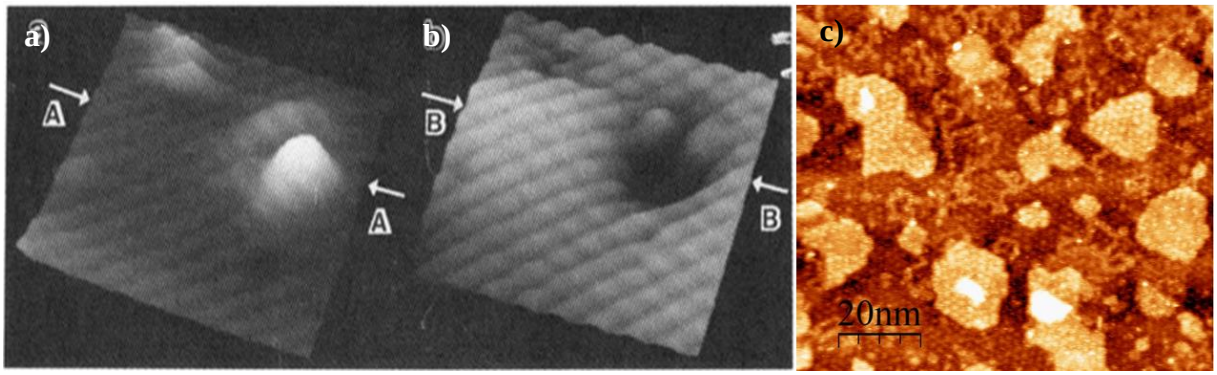


Figure 2.8: STM image of oxygen vacancy on GaAs obtained at sample voltage of: a) -2.6 eV b) 1.5 eV. Image from [95]. c) STM image of oxidized Pt/ Rh(111) displaying a moiré pattern due to formation of ultra-thin surface oxide.

#### 2.3.1.5 Scanning Tunneling Microscopy Operating at Ambient Conditions and Beyond

Both the pressure gap and the temperature gap described in section 1.1 indicate that there is a significant discrepancy between how catalytic surfaces behave in UHV or at low pressures, compared to their behavior under industrial conditions. A simple interpolation of results obtained at UHV is not sufficient to get an accurate understanding of their properties. To overcome this problem development of surface characterization techniques operating at ambient conditions and above, have gained much attention in the recent years [1, 3]. Pushing the limits of the conditions in which the STM can operate allows us to reveal new characteristics of the surfaces in more realistic conditions. Design of the instruments have grown into two different directions, STM operating at high temperatures (HT-STM), and STM operating at high pressures (HP-STM).

In principal, there are no issues with performing STM at high temperature or pressure conditions. Since the tip-sample distance is only a few Å, the vacuum gap between the two components remain even at higher pressures. Still, STM working at either high pressures or high temperature present challenges when it comes to obtain images of sufficient resolution. In addition, due to instrumental limitations it is not possible to perform measurements with simultaneous high pressure and high temperature. The Kalrez O-ring used to seal the high pressure cell does not have sufficient thermal resistance.

The main challenge when performing HT-STM measurements is thermal drift induced by contraction and expansion of materials. Due to the macroscopic size of the elements in the STM, just a small temperature variation will cause significant thermal drift on microscopic scale. This issue can be overcome by using materials with low expansion coefficients. Some STMs have been designed to

compensate for thermal drift, allowing for temperature change from 300 to 1200 K without requiring mechanical adjustments of tip [96, 97]. Upon studying graphene growth at 1200 K, a spatial resolution of 1 nm was achieved [97]. In addition, the piezo tube need to be below the Curie temperature to preserve its piezo electric properties. This is achieved by mounting a radiation shield around the piezo tube [96, 98].

There are mainly two types of designs for HP-STM. The first design was developed by McIntyre and coworkers at Lawrence Berkeley Laboratory in 1992 [99]. It used a reaction cell with a volume of 2 L with a quadrupole mass spectrometer (QMS) used to analyze the gases coming from the cell for operando measurements. Other designs based on this were developed, all having the microscope *inside* the high pressure reactor [100-102]. However, a large reactor volume allows for gas to easily absorb onto and react with the reactor walls, as well as other components in the instrument. In addition, the small surface area of sample to rector volume ratio is not optimal for operando measurements due to very low conversion rates, creating a long response time [1] (p. 6). Further loss of resolution can occur upon heating due to heat transport via the gas phase, which form convection flows where there are large temperature differences between the sample and the piezo tube [1] (p. 7).

These obstacles were taken into account when developing the Reactor STM in Leiden in 1998 [103], [1] (p. 6). The Reactor STM combine a STM instrument and a small flow reactor with a volume of only 0.5 mL place in a UHV chamber [104], and can be operated from RT to 600 K, and from UHV up to 6 bar, which makes it state of the art. Only the tip and its holder is located in the high pressure cell, as seen in Figure 2.9. This allows for study of reaction rate while simultaneously observing the structural changes in the STM images. The response time of 10 s or less make operando measurements possible by analyzing the composition of gases leaving the cell with QMS or gas chromatography (GC). The reactor is confined between the sample and the STM scanner, and sealed off with two Kalrez O-rings. It has two gas channels; one for inlet connected to a gas system to control flow, mixing and pressure, and one for outlet connected to a backpressure controller and a QMS. Heating of the sample is done from the upper side. In addition, inert materials are used to avoid reaction of gases with instrumental parts. These specifications meet the requirements to obtain atomic resolution of catalytic surfaces at pressures of 1 bar and above, and at high temperatures of at least 400 K. The instrument used at UiO in this MSc thesis is based on the design of the Reactor STM in Leiden.

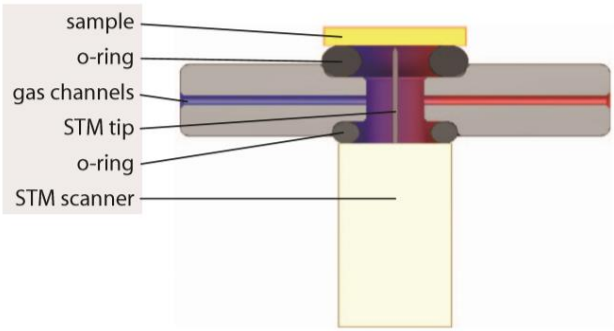


Figure 2.9: Reactor cell showing the small gas volume that is exposed to the sample, tip and tip holder. Also shown are O-rings used to seal of the gas environment and gas inlet and outlet channels. Illustration from [104].

In addition, samples should be clean well-defined model catalysts. To ensure no exposure to air to sample when transferring it from preparation stage to STM imaging, a UHV preparation chamber is situated next to the STM chamber with easy transfer by a manipulator arm. Also, the sample preparation chamber is combined with LEED and Auger electron spectroscopy (AES) for surface characterization, and a separate chamber is dedicated to XPS, all of which require an UHV environment. A schematic illustration of UHV systems with the three chambers is shown in Figure 2.10.

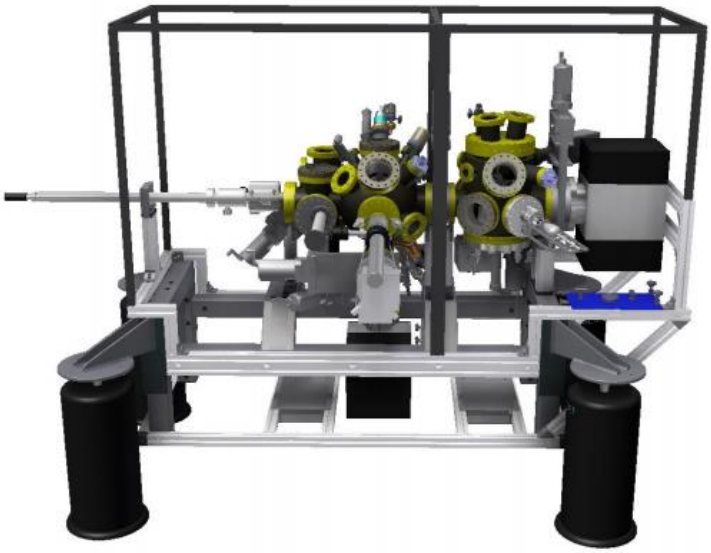

Figure 2.10: Schematic illustration of the Reactor STM showing the UHV chambers with preparation chamber combined with LEED and AES on the left side, and the STM chamber to the right. Image from [105].

### 2.3.2 X-Ray Photoelectron Spectroscopy

#### 2.3.2.1 Principles

X-ray photoelectron spectroscopy is a characterization technique used for chemical analysis of surfaces. Most of the pioneering research done on XPS was performed by the Swedish Siegbahn group in the

years following World War II, and a comprehensive study of the technique was published in 1967 [106]. XPS is based on the photoelectric effect, which was first explained by Einstein in 1905 [107]. When a photon of energy *hv* hits a material, electrons will absorb the photon energy and be excited and emitted from the material with a kinetic energy $E_K$. These electrons are referred to as *photoelectrons* [89] p. 221, and a schematic illustration of the process can be seen in Figure 2.11.

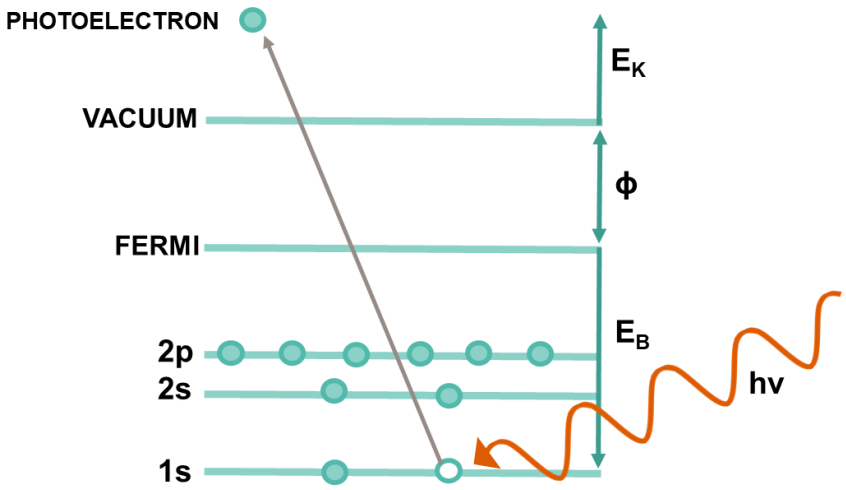


Figure 2.11: Schematic illustration of emission process of a photoelectron. The incoming X-ray hit an electron from the 1s shell, which emitted out as a photoelectron. The photoelectron is denoted 1s. Illustration based on figure from [89] (p. 222).

For the photoelectrons to be emitted, the energy of the photons must be above a certain value referred to as the work function ($\phi$), which is the minimum energy required to remove an electron from the Fermi level out to vacuum. In addition, the photoelectrons will have a specific binding energy $E_B$, measured from its shell to the Fermi level, which can be calculated from the kinetic energy value by equation 2.2 [89] p. 221:

$$E_B = hv - E_K - \phi \qquad 2.2$$

The characteristic binding energies make up the XPS spectra and are used for analysis of elements, chemical and electronic properties of the sample. A process that may occur after photoelectron emission is the formation of *Auger electrons*, which will also form peaks in the XPS spectra. As an X-ray hits an electron in a low lying shell and excites it, a second electron from a higher lying shell will relax down to the empty shell. But since the energy in the lower lying shells is higher, energy compensation has to be made, and a third electron from a high lying shell will be excited and emitted out. This third electron being sent out in order for the second electron to be allowed into the high energy state, is the Auger electron, and the process can be seen in Figure 2.12 [89] (p. 222).

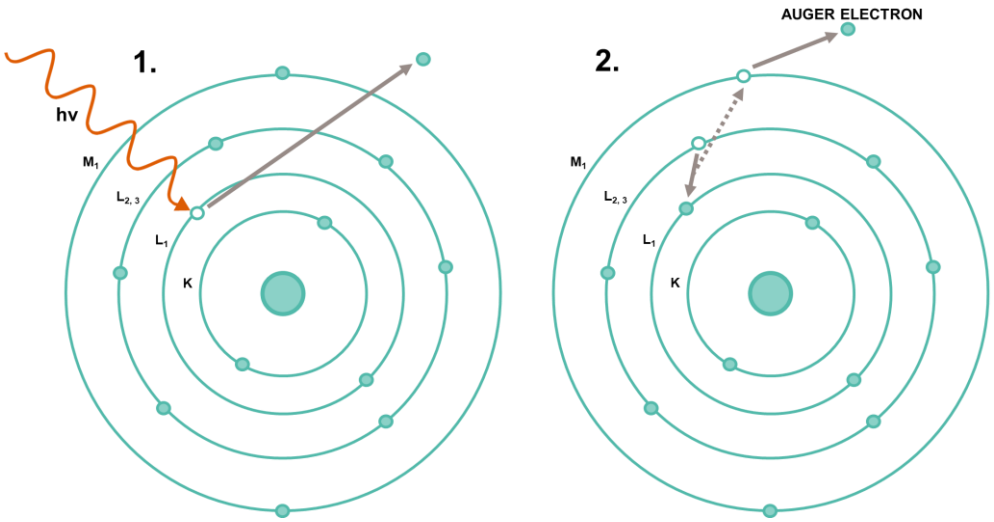


Figure 2.12: Schematic illustration of Auger emission process. In scheme 1 an electron from $L_1$ shell is excited out from the photon, and in scheme 2 an $L_{2,3}$ electron relaxes down, and an Auger electron from $M_1$ shell is emitted out to compensate for energy difference. The Auger electron is denoted $L_1L_{2,3}M_1$. Illustration based on figure from [89] (p. 192).

The strength of XPS in regards to surface science is the high surface sensitivity. Only electrons from the very upper part of the sample, from 10 nm and below, escape the surface since electrons scatter very strongly in matter [89] (p. 221) [1] (p. 33). In addition, the escape depth of the photoelectrons can be tuned by adjusting the energy of the incident X-rays. Since higher photon energy results in higher kinetic energy for electrons (equation 2.2), deeper or shallower surface layers can be probed by employing higher or lower photon energy. Importantly, with increasing kinetic energy the electron scattering cross section decreases [1] (p. 33).

#### 2.3.2.2 Instrumentation

The conventional instrument used for XPS analysis is called an electron spectrometer, and can combine both XPS and AES analysis in a single chamber. An overview of the instrument can be seen in Figure 2.13. To prevent electrons from scattering with gaseous species on their path to the detector there is a requirement for a UHV environment in the range $10^{-8}$ - $10^{-10}$ mbar [89] (p. 225). This is important since high levels of gaseous species results in decrease of signal intensity and increase of background noise. UHV environment is also important to avoid gas molecules from absorbing onto the sample surface, which is especially troublesome when performing surface chemical analysis. To ensure UHV, different types of pumps are used, such as diffusion pumps, sputter ion pumps, and turbo molecular pumps. In addition baking of the instrument to high temperature is necessary to ensure removal of internal gas molecules [89] (p. 225-227).

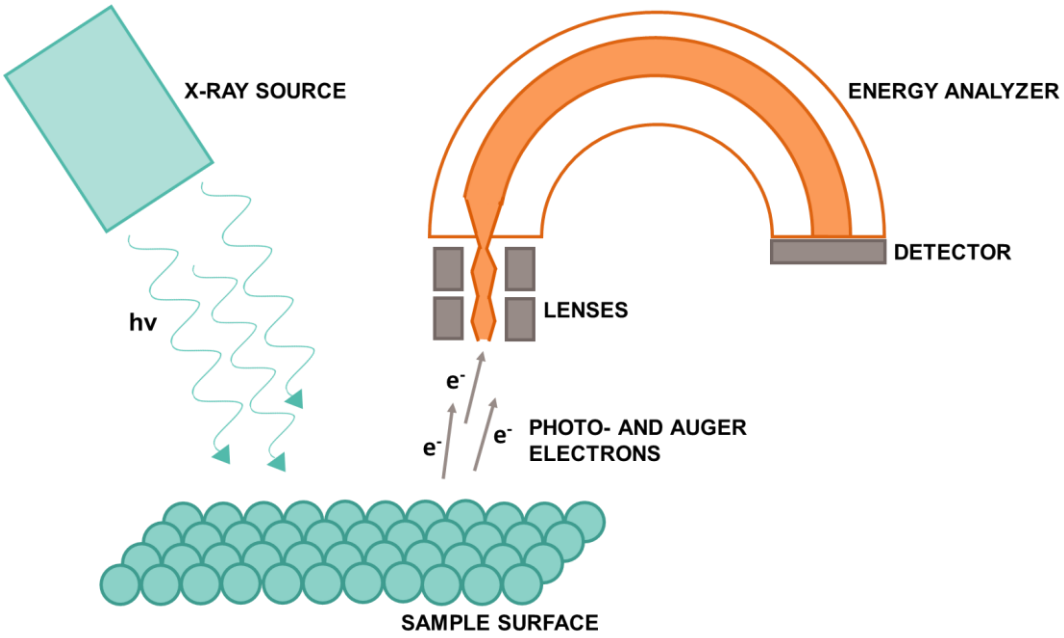


Figure 2.13: Schematic illustration showing electron spectrometer for both XPS and AES analysis. An X-ray source sends photons towards sample surface, where photo- and auger electrons are ejected. Electrons are focused by lenses before they enter the hemispherical energy analyzer which separated based on energy. Finally they are detected by the electron detector. Illustration based on figure from [108] (p. 100).

The sample is placed on a sample stage inside the analysis chamber. The X-ray tube is also directed into the analysis chamber. The X-ray tube is an important element of the spectrometer, where the X-rays are produced by high-energy electrons hitting a metal anode, which typically is made out of Al or Mg. One can find both monochromatic, where the continuous X-rays are filtered out and only photons with fixed energy are used, as well as nonmonochromatic sources, where both characteristic lines and continuous background is included. However, monochromatic X-ray sources provide spectrums with less background noise. [89] (p. 227-229).

In order to focus the electrons coming of the surface sample and into the electron energy analyzer, a set of electrostatic collection lenses are placed right after the specimen stage. To analyze the energy of the incoming electrons, an electron energy analyzer consisting of two concentric hemispheres is used. The hemispheres are biased, which allows only electron with a certain kinetic energy, referred to as “pass energy”, to reach the electron detector [1] (p. 32). The electron detector is located at the end of the hemispherical electron energy analyzer, and is typically a phosphor screen with camera or an electron multiplier. [1] (p. 32).

#### 2.3.2.3 Analysis of X-ray Photoelectron Spectra

As with other spectroscopic techniques, an XPS spectra provides average information, not area specific. Still, XPS is a surface sensitive technique, so the electrons reaching the detector are from the top part of the sample (ca. 10 nm). By detecting the energy of the electrons, a spectra is formed. An example of an XP (X-ray photoelectron) spectra is given in Figure 2.14, which is expressed by photoelectron intensity versus binding energy ($E_B$). There are mainly three peak types that make up the XP spectra; photoelectrons from core-levels and photoelectrons from valence-levels, both labelled with the corresponding orbital they originate from, and Auger electrons emitted by X-rays which are labelled with letters from the shells involved in the Auger process. Another feature of the XPS spectra is the background with its step-like shape that increases with binding energy. It usually arises from inelastic scattering of photoelectrons, as well as from excitation of electrons caused by the continuous X-rays.

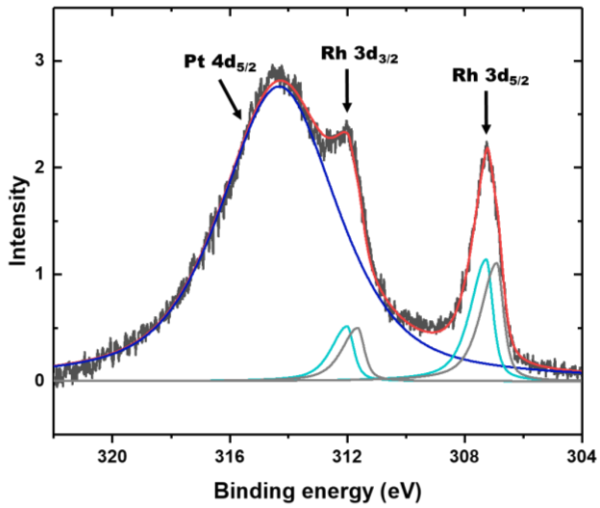


Figure 2.14: Example of fitted XPS spectra from Rh on Pt(111). Spectra show photoelectron peaks from Rh 3*d* and Pt 4*d* orbitals.

In addition, spectral features like shake-up satellites, multiplet splitting and plasmon loss can be observed. Shake-up satellites arise when a photoelectron interact with a valence, which results in a small loss of kinetic energy for the photoelectron and creates a small satellite peak close to the core-level peak. Multiplet splitting may be seen in the core-level peaks when the compound has unpaired electron in the valence-level. Plasmon loss peaks results from the kinetic energy loss of photoelectrons due to excitation of phonons. They typically complicate the spectrum rather than providing useful information. [89] (p. 231-233)

##### 2.3.2.3.1 Qualitative information

XPS is used for chemical analysis of surfaces, and can reveal elemental composition, as well as chemical and electronic properties of the sample by identifying the peaks. Peak position can also be affected by

instrumental factors, and the binding energy needs to be calibrated before use. It should also be noted that peak identification can be difficult in XPS due to presence of Auger peaks. Peaks from the core-level electrons are used for elemental analysis by looking at the peak position and the corresponding binding energy.

The peak position of an element is sensitive to its chemical environment, which will cause small peak shifts referred to as chemical shifts. Chemical shifts are used to determine the chemical and electronic structure, and the valence-level electrons with low binding energy are used for this. Oxidation state of an element can be determined with chemical shifts. Higher oxidation state of an element results in a shift to higher binding energies for the electron, hence a shift in the peak. This is because oxidation involves removal of valence electrons, so the remaining electrons feel a stronger Coulombic interaction with the nucleus, and thus have a higher binding energy. This information is very useful upon inspection of possible oxidation of an element. An example is the oxidation of Rh, where formation of a $RhO_2$ surface oxide results in a component shifted to +0.75 eV relative to the bulk species, and a component at +1.04 eV corresponds to $Rh_2O_3$ bulk oxide [69]. Shifts can also cause peak overlap, which then need to be resolve when doing data analysis.

A challenge with XPS is that investigating insulating materials, a positive charge build-up will occur on the surface. This causes a change in surface potential, which will affect the peak position. To overcome this issue, an electron flood gun is used. Mapping of elements can be done by using a monochromatic X-ray gun to scan over the sample area, and images are formed. In addition, depth profiling is possible by sputtering layer by layer with an ion gun. [89] (p. 235-243, 247).

#### 2.3.2.3.2 Quantitative information

XPS can also provide quantitative information about the sample. By using the peak area and peak width, the relative concentrations of different species can be determined. The expected accuracy is between 5-10 %, but larger errors may occur due to e.g. inaccurate background subtraction and large variations in concentration in the sample area analyzed [109]. The relative intensity of a photoelectron peak can be expressed through equation 2.3 [89] (p. 246):

$$X_i = \frac{I_i/S_i}{\sum I_j/S_j} \qquad 2.3$$

Where $X_i$ is the atomic fraction of element i, $I_i$ is the peak area of element i, $S_i$ is the sensitivity factor of element i, and the denominator is the sum of all contributions. The sensitivity factor is element specific and can be determined experimentally. It also varies with instrument and sample surface, so usually the sensitivity factor is measured for a standard sample in a specific instrument. [89] (p. 246).

#### 2.3.2.4 Ambient Pressure X-ray Photoelectron Spectroscopy

In order to perform experiments under more realistic conditions, development of the first ambient pressure XPS (AP-XPS) was initiated by the Siegbahn group in 1973, who also developed the first XPS [110]. They obtained spectra under liquid and gaseous environments, and developed the differential pumping system. However, due to low count rate and poor signal-to-noise ratio, these early developed AP-XPS instruments were not widely used [3]. Development of a new AP-XPS with improved design was initiated in 2002 at Lawrence Berkeley National Library, and the use of high-flux synchrotron radiation as X-ray source and a differential-pumped electrostatic lens system was implemented [3] (p. 200).

In recent years, AP-XPS has become a well-established technique world-wide. AP-XPS endstation have been installed at most of the major synchrotron light source facilities [3], and as of 2019 around 30 synchrotrons and laboratory based instruments were in operation [111]. These include installations like ALS (USA), Soleil (France), Alba (Spain), Bessy (Germany), MAX-IV (Sweden) and Photon Factory (Japan). This is also reflected in the large increase of AP-XPS publications in recent years [14]. In this MSc thesis the HIPPIE beamline at MAX-IV was used in the AP-XPS experiments.

The main motivation for developing XPS operating at higher pressures, is to close the pressure gap in materials research. Most of the research done in surface science has been done in a UHV environment, and results are often extrapolated and compared to results of in-situ UHV measurements and ex-situ measurements at higher pressures [3] (p. 198). The reality, however, can be very different from the extrapolated results, and there is a need for in-situ measurements at elevated pressures to get a more correct understanding of reactions happening at ambient pressures.

As mentioned above, there are challenges to overcome when introducing a gaseous environment inside the analysis chamber. Firstly, photoelectron scatter strongly with gas molecules, which reduces the inelastic mean free path (IMFP) of the photoelectrons and hinders them from reaching the detector. The IMFP is as short as 1 mm in 1.3 mbar of water vapor, while the electron path in the instrument is the order of a meter [1] (p. 33). Another obstacle to overcome is discharging through the gas with high voltage differences, as in the electrostatic lens system. This issue can be overcome by proper lens system design and sufficient pumping [1] (p. 33).

As previously mentioned, the modern AP-XPS systems developed use a differential-pumped electrostatic lens system in order to capture and focus the electron as quickly as possible, while simultaneously pumping out the gas to avoid scattering events. In addition, the chamber consists of a high pressure sample cell and the electron analyzer. The differential-pumping stages are separated by

millimeter sized apertures to minimize the gas flow, but allow electrons to pass through [1] (p. 35). The improvements that have been achieved so far allow for experiments to be carried out at maximum pressure of 13 mbar [1] (p. 34). Simultaneous detection of gas evolution with a MS allows for operando measurements. By following changes in chemical state of components, and measured gas formed in MS, catalytic processes can be monitored and understood while they are happening. Specifics of MS can be found in section 2.3.4. A schematic of the AP-XPS system at Photon Factory with differential pumping can be seen in Figure 2.15.

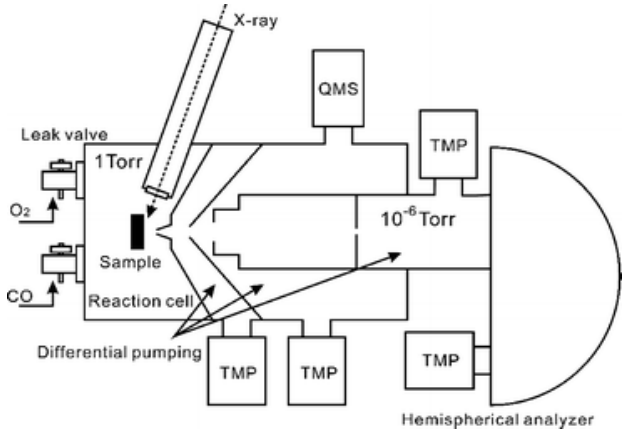


Figure 2.15: Schematic of analysis chamber of XPS at Photon Factory with X-ray gun, high pressure sample chamber, differential pumping system and electron energy analyzer. Image from [3].

### 2.3.3 Low-energy Electron Diffraction

#### 2.3.3.1 Principles

In 1927, Davisson and Germer were the first to display a diffraction pattern upon firing low energy electrons towards a nickel crystal [112]. This finding along with other similar experiments, provided a direct observation the wave-like nature of electron. The relation between wavelength and momentum was first formulated by de Broglie in 1924, and is shown in equation 2.4. Due to the wave-like nature of electrons they can be used as probes to study crystal structures.

$$\lambda = \frac{h}{p} \qquad 2.4$$

LEED was then developed further by Germer at Bell Telephone Laboratories in the USA [113]. The concept of LEED is similar to that of X-ray diffraction, but the scattered electrons only arise from the topmost atomic layers. The diffraction process can be understood by assuming an electron wave with wave vector $\mathbf{k_0}$ scattering with a two-dimensional array of scattering sites, defined by lattice vectors **a**,

**b** (**a, b, c** for three-dimensional lattice). The interaction between the electron wave and the two-dimensional lattice is simplified by considering the reciprocal lattice with lattice vectors **a***, **b***, **c***. For constructive interference of the scattered waves to occur, the change in wave vector of the electron upon diffraction must coincide with the reciprocal lattice vector **g** as seen in equation 2.5:

$$(\boldsymbol{k'} - \boldsymbol{k_0}) = \boldsymbol{g} = h\boldsymbol{a^*} + k\boldsymbol{b^*} + l\boldsymbol{c^*} \; (h, k, l, = 0, 1, 2, \ldots) \qquad 2.5$$

The amplitude of the wave vector does not change due to elastic scattering process, only the direction, so $k' = k_0$. The criterion for constructive interference can be illustrated by using the Ewald sphere, which is a sphere with a radius $2\pi\lambda\text{-}1 = k0$ constructed in the reciprocal lattice. Since we are considering a two-dimensional lattice, this means c approaches infinity and c* approaches zero, the reciprocal lattice consists of a series of rods in a two-dimensional array, as seen in Figure 2.16. If the reciprocal lattice rods intersects with the Ewald sphere, the diffraction condition $(\mathbf{k'} - \mathbf{k_0}) = \mathbf{g}$ is fulfilled and a diffraction beam is observed. The detector screen where we see the diffraction pattern in LEED represents the Ewald sphere. Since the scattered electron do not strictly come from one atomic layer, a combination of a two- and three-dimensional effect is present. So for any wave number of the electron wave, the rods are present, but their intensity will vary periodically [76] (p. 8-9).

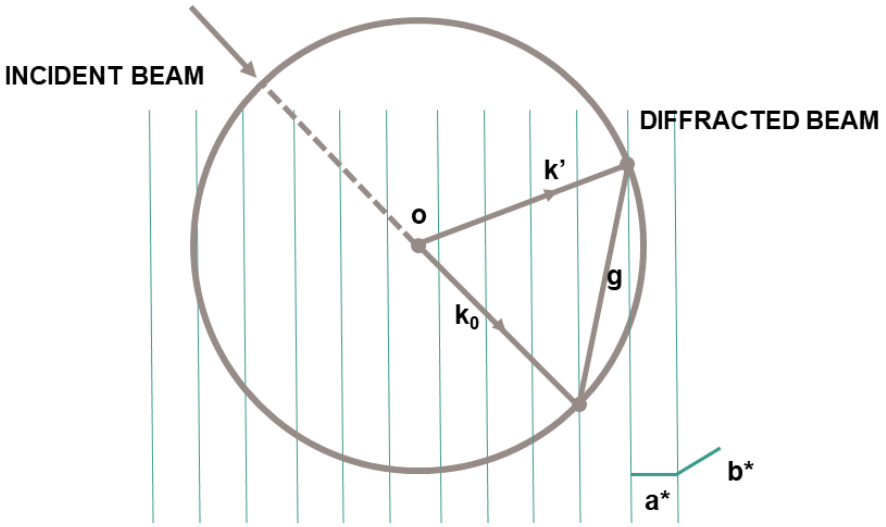


Figure 2.16: Schematic illustration of Ewald sphere showing reciprocal lattice in two-dimensions. The incident beam scatter at origin, and constructive interference occur since diffraction condition of $(k_0\text{-}k') = g$ is met. Illustration based on figure from [76] (p. 10).

What distinguishes LEED from other diffraction techniques is the use of electrons in the low energy regime for structural characterization. The energy of the electrons is in the order of 20-500 eV, resulting in a de Broglie wavelength of 0.05-0.3nm [114]. This is in the interatomic spacing regime, which then satisfies the diffraction condition. Since the penetration depth of the low energy electrons used in LEED

is around 0.5 to 2 nm, compared to X-rays on the order of $10^5$ nm [76] (p. 6), only electron coming from the topmost atomic layers will escape the sample surface and give rise to the diffraction pattern [113]. This is what makes LEED an excellent tool for surface crystallography.

#### 2.3.3.2 Instrumentation

Since low-energy electrons interact strongly with matter, it is necessary to have a UHV environment, and a maximum pressure of $1\times10^{-7}$ mbar is required. The main components of the LEED apparatus are an electron gun, a specimen manipulator and a detector screen with grids, as shown in Figure 2.17 a). Electrons are generated from a heated W filament cathode and accelerated to an anode, which has a positive potential relative to the cathode. The electron beam is perpendicular to the sample surface, and the electrons are diffracted with an angle depending on energy of the beam and the interatomic distance in the material. There are several grids located in front of the hemispherical detector screen. The first grid is grounded to capture backscattered electrons, while the second and third grids are biased to deflect inelastically scattered electrons. The fourth grid is also grounded, and is used to shield the screen from the field, since the screen is biased to high voltages to reaccelerate the elastically scattered electrons [114]. Elastically scattered electrons are detected on the fluorescent screen where the diffraction pattern can be observed, similar to what is shown in Figure 2.17 b).

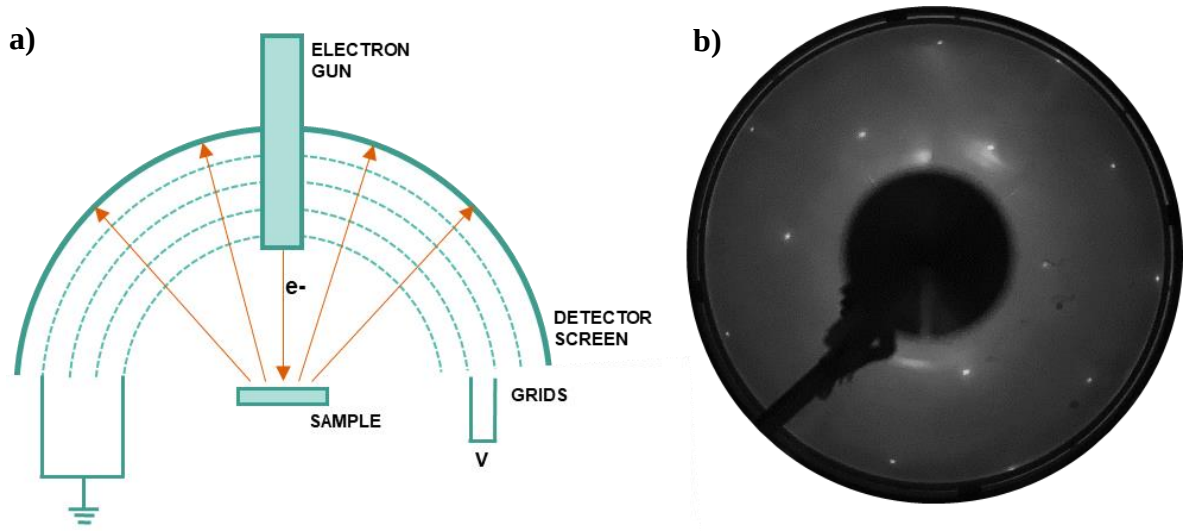


Figure 2.17: a) Instrumentation of LEED with main components: electron gun, sample holder, grids and detector screen. Illustration based on figure from [114]. b) Example of LEED diffraction pattern of 0.65 ML Pt/Rh(111) obtained on detector screen at an energy of 197.7 eV.

#### 2.3.3.3 Analysis

From the diffraction pattern, the crystal structure of the sample surface can be determined from spot position. Information about size, symmetry and atomic positions can be extracted, as well as unit cell

dimensions of absorbates with respect to the substrate unit cell. Construction of so-called I-E spectra can be used to analyze the structure, where the spot intensity is plotted against the incident electron beam energy [114]. Experimental curves can then be compared to theoretical curves to determine if the structure is close to what is expected.

### 2.3.4 Mass Spectrometry

Mass spectrometry is used to determine the weight of a molecule and molecular fragments. By breaking apart the molecules and measuring the weight of the constituents, some structural information can be obtained as well [115] (p. 424-425). The spectrometer consists of three units: an ionization source, a mass analyzer and a detector, as seen by Figure 2.18. The sample to be investigated is vaporized and sent through the ionization source to ionize the sample gas molecules. This is done by bombarding them with high-energy electrons. During this process, some of the ionized molecules can fragment into smaller pieces. If these retain a charge, they will be detected. If they are neutralized however, they will be not go through the mass analyzer. The ionized molecules then move through a strong magnetic field that is curved. Depending on their mass-to-charge (m/z) ratio their trajectories will-bend to a certain angle and be detected separately. Since most molecules have charge +1, the value of (m/z) often means simply the mass [115] (p. 425).

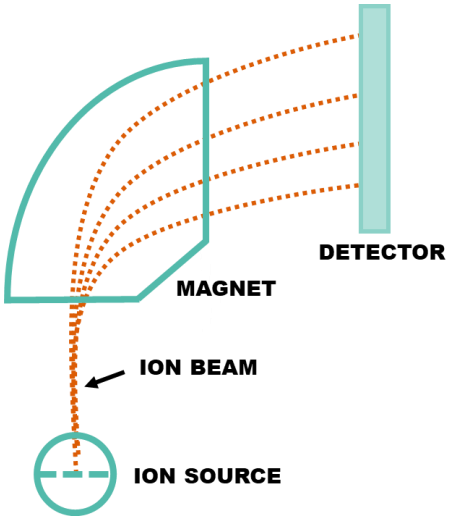


Figure 2.18. Schematic illustration of a mass spectrometer showing the ion source ionizing the molecules, which are then curved by a magnetic field in the mass analyzer, and then detected. Illustration based on figure from [116].

In the mass spectrum, the intensity or relative abundance (m/z) is plotted against the mass-to-charge ratio (m/z). The most intense peak in the spectrum is referred to as the base peak, while the peak of the unfragmented ionized molecule is called the parent peak [115] (p. 426). MS is used in combination with both STM and XPS to conduct operando measurements, and measure the gas product formed during a reaction.

# 3 Experimental

The experimental work described in this MSc thesis was performed using two different instrumental set-ups. STM imaging and LEED were performed in a commercial Reactor STM at the University of Oslo [117]. NAP-XPS was performed at the HIPPIE endstation at MAX-IV, Lund [118].

## 3.1 Sample preparation

### 3.1.1 Rh(111) and Pt/Rh(111) Sample Preparation and Oxidation in Reactor STM

For the STM imaging and LEED, a single crystal of Rh cut in the (111) direction with a base diameter of 10 mm and height of 2 mm produced by Surface Preparation Laboratory (SPL, NL) was used. Sample preparation was performed in the preparation chamber of the Reactor STM with a base pressure of $1 \times 10^{-9}$ mbar. Since the Rh(111) single crystal came directly from producer when this MSc work started, repetitive cycles of sputtering and annealing was performed before the first imaging. Another fifteen cycles were performed before evaporation of Pt. Sputtering was performed using a SPECS IQE 11/35 ion source. $Ar^+$ (5.0, Westfalen) sputtering was performed at 1.5 kV for 15 min, at a pressure of 1.6 - $1.8 \times 10^{-5}$ mbar and a sample current of ~5μA. Subsequent annealing was performed in UHV at 1100 – 1130 K for 10 min. Every third cleaning cycle included oxidation in $1 \times 10^{-7}$ mbar $O_2$ (5.0, Westfalen) at 923 K for 5 min followed by UHV annealing for 10 min. Prevac HEAT-PS3 power supply was used to control sample heating, either in automatic or manual mode. Temperatures of 800 K and lower were reached with radiative heating, and higher temperatures were reached using combined radiative and e-beam mode. To ensure reproducible readout of sample temperature, a K-type thermocouple was used in combination with a Micro-Epsilon TIM 1M IR thermal imaging camera. Emissivity value of 0.43 was used for the polished Rh surface. Figure 3.1 a) show the Rh(111) single crystal during annealing. Cleanness of surface was verified by means of LEED (Figure 3.1 b)) and STM (atomic resolution was achieved, Figure 3.1 c)).

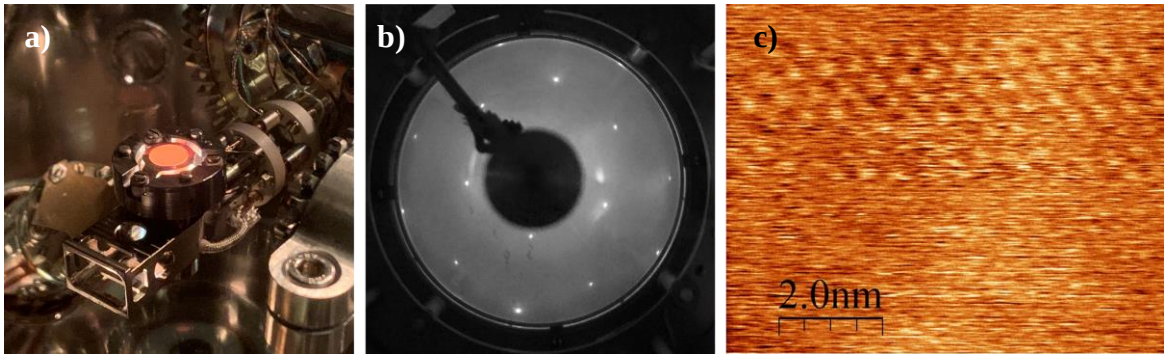


Figure 3.1: a) Visible camera image showing the Rh(111) single crystal during annealing. The crystal is mounted on the sample holder and heated with a combination of radiative and e-beam heating. b) LEED of Rh(111) at

250eV after repetitive cycles of cleaning. c) STM image taken at a sample bias of -0.05 V and tunneling current of approximately 1 nA, showing clean Rh(111) after repetitive cycles of cleaning with atomic resolution.

Between experiments, the crystal was cleaned in three cycles, including oxidation during the second cycle. After deposition of larger amounts of Pt on Rh(111) sputtering was kept for longer than 15 min, with a sample current between 6 - 8 µA. Deposition of Pt (Goodfellow 99.95%) on Rh(111) was performed in UHV using a SPECS four pocket electron beam evaporator EBE-4. The EBE-4 was operated at a high voltage of 1.5 kV, a flux of 12 nA or 20 nA, resulting in a rate of approximately 0.04 ML/min. Deposition was performed at sample temperatures in the range 300 - 700 K for 5 - 100 min, with heating performed in radiative mode. Subsequent PA was performed at 600 – 700 K for 5 – 10 min. Oxidation was performed by exposing to surfaces to $1 \times 10^{-3}$ mbar of $O_2$ for 20 min while keeping the temperature at 700 K. To avoid contaminations from the hot cathode filaments used in the vacuum gauges, they were shut off during oxidation and the pressure was monitored with the full range magnet gauge. An overview of experiments performed and presented in Chapter 4 are shown in Table 3.1.

Table 3.1: Summary of sample preparation conditions and STM measurements. Thick horizontal line separates metallic as-prepared (AP) and PA surfaces (above the line), and oxidized surface (below the line). A star (*) indicate that the experiment was repeated more than once. Below the line STM images were taken for almost all AP, PA and oxidized surfaces, where two stars (**) indicate that PA surface was not imaged.

| **Sample** | **Evap. Temp., K** | **Evap. Time, min** | **Evap. Flux, nA** | **PA Temp., K** | **PA Time, min** | **Oxygen Pressure, mbar** | **Oxidation Temp., K** | **Oxidation Time, min** |
|---|---|---|---|---|---|---|---|---|
| Pt/Rh(111) | 335 | 5 | 12 | 700 | 5 | - | - | - |
| Pt/Rh(111) | 385 | 5 | 12 | - | - | - | - | - |
| Pt/Rh(111) | 400 (*) | 5 | 12 | 600 | 5 | - | - | - |
| Pt/Rh(111) | 425 (*) | 5 | 12 | 600 | 5 | - | - | - |
| Pt/Rh(111) | 450 | 5 | 12 | 600 | 5 | - | - | - |
| Pt/Rh(111) | 475 | 5 | 12 | - | - | - | - | - |
| Pt/Rh(111) | 500 | 5 | 12 | 600 | 5 | - | - | - |
| Pt/Rh(111) | 600 | 5 | 12 | 600 + 650 | 5 + 5 | - | - | - |
| Pt/Rh(111) | 425 | 30 | 12 | 600 | 5 | - | - | - |
| Rh(111) | - | - | - | - | - | $1 \times 10^{-3}$ | 700 | 20 |
| Pt/Rh(111) | 425 | 5 | 12 | 700 (**) | 10 | $1 \times 10^{-3}$ | 700 | 20 |
| Pt/Rh(111) | 425 | 12.5 | 12 | 700 (**) | 10 | $1 \times 10^{-3}$ | 700 | 20 |
| Pt/Rh(111) | 425 | 25 | 12 | 700 | 10 | $1 \times 10^{-3}$ | 700 | 20 |
| Pt/Rh(111) | 425 | 80 | 12 | 700 | 20 | $1 \times 10^{-3}$ | 700 | 20 |

| | | | | | | | | |
|---|---|---|---|---|---|---|---|---|
| Pt/Rh(111) | 475 | 5 | 12 | - | - | 1000 | 300 - 485 | *In-situ* |
| Rh(111) | (*) | - | - | - | - | 1000 | 300 - 470 | *In-situ* w/ heat tracing |

### 3.1.2 Pt(111) and Rh/Pt(111) Sample Preparation for NAP-XPS

For NAP-XPS measurements, a Pt(111) single crystal (SPL) with a diameter of 10 mm was used. Sample preparation was performed in the preparation chamber of the HIPPIE endstation at MAX-IV. The crystal was cleaned in repetitive cycles of $Ar^+$ sputtering at an energy of 1 kV for 10 min followed by annealing at 1150 K, both in $O_2$ ($5 \times 10^{-7}$ mbar for 2 min) and in UHV (5 min). Crystal quality in terms of cleanness was verified by XPS. Rhodium (99.9%, Goodfellow) was subsequently deposited onto the Pt(111) single crystal using the e-beam evaporator. The depositions were done at 360 K in UHV at a pressure less than $2 \times 10^{-9}$ mbar, using a flux of 0.08 ML/min for 4-15 min. Subsequent PA was performed for all surfaces. Duration of PA was inversely proportional to temperature used, but in the range 5-20 min for 600-770 K, respectively.

## 3.2 Characterization

### 3.2.1 Scanning Tunneling Microscopy

Analysis by means of STM was performed to study the morphology of nanostructured Pt/Rh(111) surfaces. All STM images were taken in the Reactor STM system at the University of Oslo, based on the design of the Reactor STM built at Leiden University [104]. All UHV measurements were conducted at RT, with a base pressure of $1 \times 10^{-9}$ mbar. To avoid mechanic noise interference turbomolecular pumps were disabled prior measurements, and the instrument was pumped with ion pumps only. STM was conducted with manually cut $Pt_{80}It_{20}$ 0.25 mm diameter tips (Goodfellow). The CAMERA 4.3 software package was used for data recording. Images were recorded in constant current mode, with a sample bias between -0.05 and -0.5 V for metallic surfaces, and -1.0 V for oxidized ones. The tunneling current was typically 0.1 – 0.2 nA for large scale images, while 1 nA was used to obtain atomic resolution. For *in-situ* measurements, a flow reactor of 0.5 mL sealed with a Kalrez ring was used. The measurements were performed at a total pressure of 1 bar of Ar and/or $O_2$ (6.0 Praxair, now Nippon gases), and temperatures from 300-485 K.

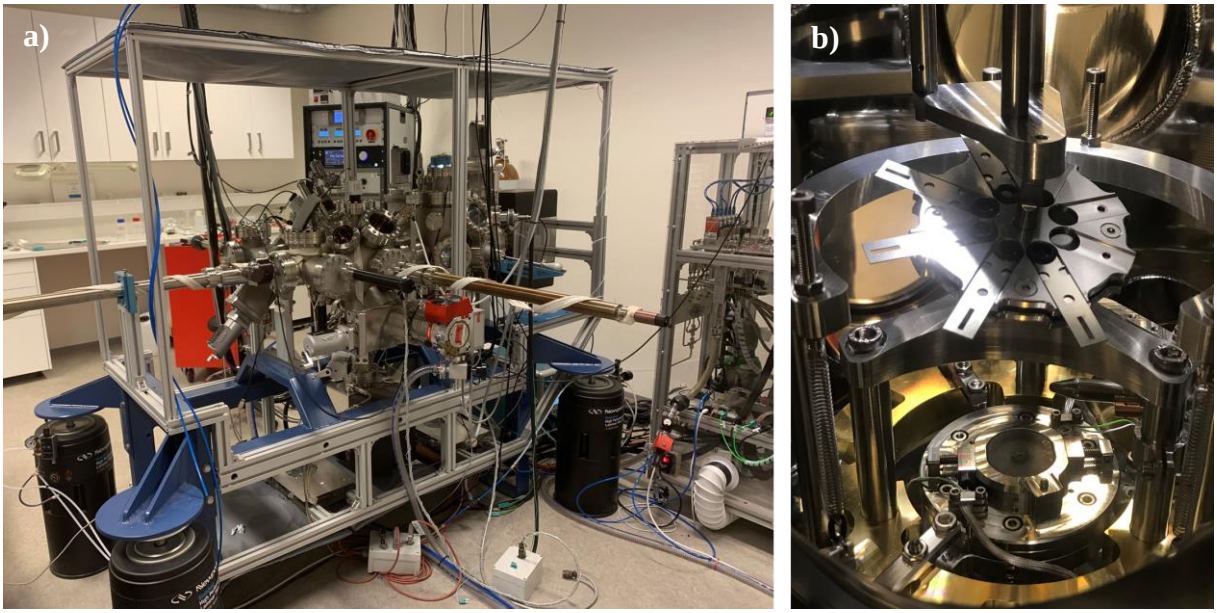


Figure 3.2: a) Image of the Reactor STM instrument at the University of Oslo. The machine is suspended on floating legs. The left chamber is the preparation chamber where cleaning, deposition and, LEED was performed. To the left the manipulator is used for moving samples between library, preparation chamber, and STM chamber. To the right is the STM chamber where scanning was performed. The gas cabinet with bottles is partially visible on the right side of the image. b) Image of STM stage without the sample. The tip is located in the middle of the circle on the bottom, and the sample is mounted above. Kalrez rings used for high pressure *in-situ* measurements are stored in the carousel at the top.

### 3.2.2 Low-Energy Electron Diffraction

To check the cleanness, crystallinity and structure of the surfaces, LEED was performed using an ErLEED from SPECS. The cathode current was set to 2.3 A and the fluorescent screen to 5000 V. Using a remote controller the energy of the electron beam was tuned between 0 and 400 eV. LEED pattern at various energy values were taken using a phone camera.

### 3.2.3 Near-Ambient Pressure X-ray Photoelectron Spectroscopy

All NAP-XPS experiments were carried out at the HIPPIE endstation of MAX-IV, Lund using an ambient pressure cell (Lund design) capable of operation up to 30 mbar. During the *in-situ* measurements at 1 mbar $O_2$ (5.0, Linde), the sample surface was heated to 600 K using laser. Spectra were recorded with a beamline monochromator exit slit of 60 µm. For O1*s*, pass energy of 100 eV was used, while for Rh 3*d* Pt 4*d* 50 eV was used, and 20 eV for Pt 4*f*. More surface sensitive measurement was performed at electron kinetic energy of 200 – 300 eV, and more bulk sensitive measurement at 500 – 600 eV. The Fermi level was used to calibrate the binding energy for all spectra, and was measured at the same photon energy.

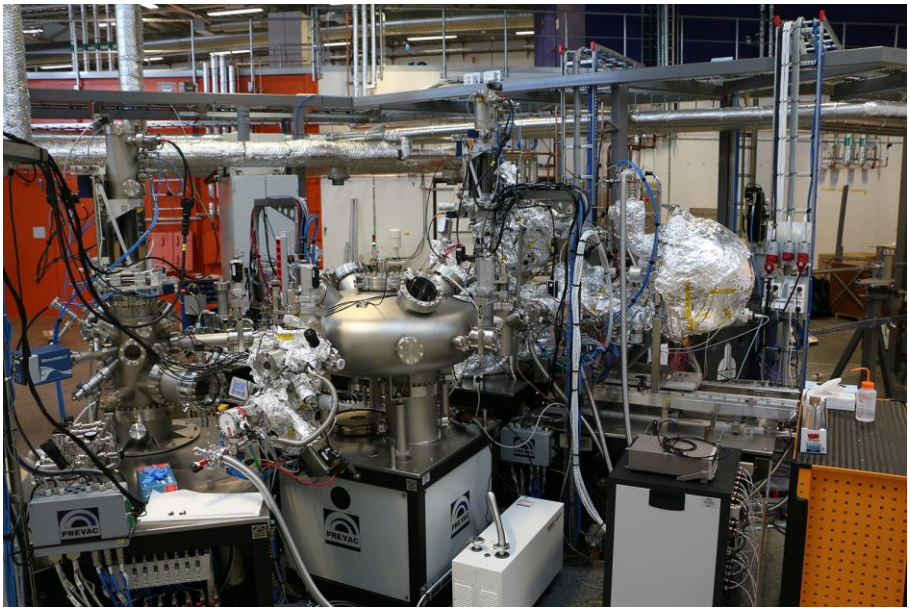

Figure 3.3: Image of the HIPPIE endstation at MAX-IV. Preparation chamber is located to the left, and XPS chamber is located to the right [119].

## 3.3 Data Analysis

### 3.3.1 Gwyddion

Analysis of STM images was performed in Gwyddion 2.55, a software for scanning probe microscopy (SPM) data analysis [120]. For calculations of coverages and island size distributions, the steps shown in Figure 3.4 were followed. Images were corrected for horizontal scars, polynomial background was removed and row alignment was performed. In addition, to facilitate automatic island detection, the image was cut in such a way that only islands residing on the same terrace were within the frame. Grains were marked by height threshold, and from the distribution of grains the projected area was extracted. The sum of projected area divided by the total area of the frame corresponded to the coverage, and the distribution of island sizes could also be extracted from this data. For each experiment the coverage and island size distribution were calculated for several frames, and an average is reported.

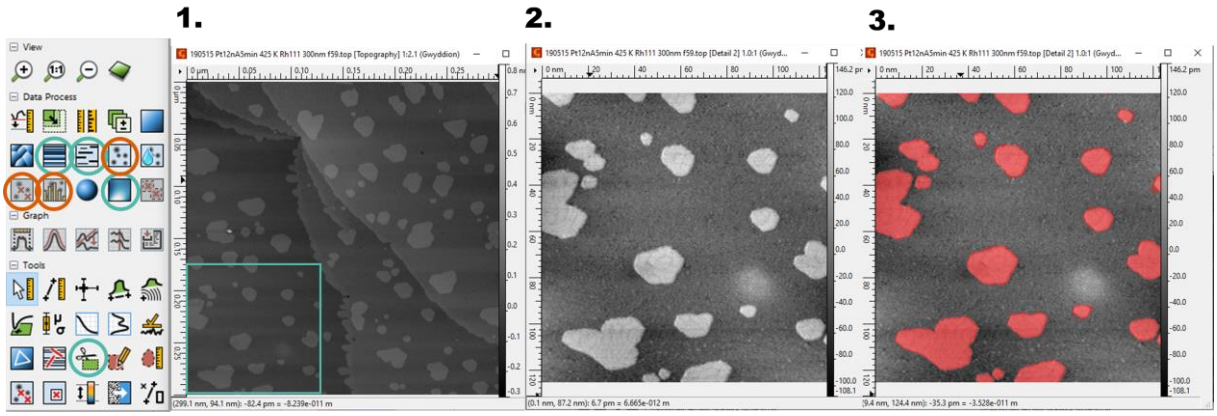


Figure 3.4: Screenshot of Gwyddion program used for calculation of coverage and island size distributions. Image 1. show initial frame where green rectangle correspond to area seen in image 2. Tools with green circles are used to remove scars, background and align rows before image is cut. All islands in image 2. are located on the same terraces. Then tools marked with an orange circle are used to obtain masked image in 3.

### 3.3.2 WSxM

For analysis of height profiles, and to export the STM images for the thesis, the SPM analysis software WSxM 5.0 was used [121].

### 3.3.3 WinSpec

Fitting of XPS spectrums was done in the least square curve-fitting program WinSpec 2.09, developed at the LISE laboratory at the University of Namur, Belgium. Shirley background was subtracted from all spectrums. Pt 4*d* and O 1*s* core levels were deconvoluted with mixed singlet peak shape, which is a mix of Gaussian and Lorentzian functions. Deconvolution of Rh 3*d* and Pt 4*f* core levels were done with asymmetric peak shape, which is similar to a Doniach-Sunjich line shape. The values for peak width and mixing ratio were kept relatively constant. Error in peak position was estimated to be approximately ±0.1 eV.

# 4 Results

## 4.1 Low coverage Pt/Rh(111) surfaces

In this section we present the results from the preparation of various Pt/Rh(111) surfaces, whereof Pt was deposited by e-beam evaporation at a rate of 0.04 ML/min on a clean Rh single crystal cut in the (111) direction. The as-prepared surfaces had a coverage in the range 0.1 – 0.2 ML. Included to the experiments is an evaluation of the reproducibility in the preparation of a specific nanostructured Pt/Rh(111) surface. The results are summarized in a "synthesis strategy roadmap" describing how to prepare well-defined Pt-Rh nanostructured surfaces.

In order to get a full overview how Rh(111) substrate temperature induces morphological transitions occurring as a result of different surface mobility, deposition was done with step-wise increment in temperature starting from RT going up to 600 K. Additional post-annealing in the range 600 - 700 K was performed for most surfaces. Post-annealing was done in order to create new morphologies where mixing of Rh and Pt and surface alloying was facilitated. This is desirable since ammonia oxidation catalyst gauzes used in industry utilizes alloyed Pt-Rh [21]. Keeping the post-annealing temperature constant also allows isolating how initial deposition temperature affects the final surface.

### 4.1.1 Morphology of Pt/Rh(111) As-Prepared at Room Temperature

Deposition of 0.2 ML Pt on Rh(111) at RT resulted in nucleation and growth of small dendritic islands on terraces as can be seen in Figure 4.1 a). The height of the islands was 0.23 nm, corresponding to one atomic layer of Pt on the Rh(111) as can be seen in Figure 4.1 b). This is in contrast to the two and three-layered islands that Zheng et al. observed for 0.2 ML Rh/Pt(111) at 300 K [37]. The island size distribution was narrow as Figure 4.1 c) and d) shows, with island diameters ranging from 1 - 6 nm. A small amount of islands also nucleated along step edges, but there seemed to be no strong preference for this. This was also reported for Pt/Pt(111) deposited at 205 K [31]. The low deposition temperatures resulted in reduced mobility for adatoms, causing islands to nucleate where the adatoms first met the surface.

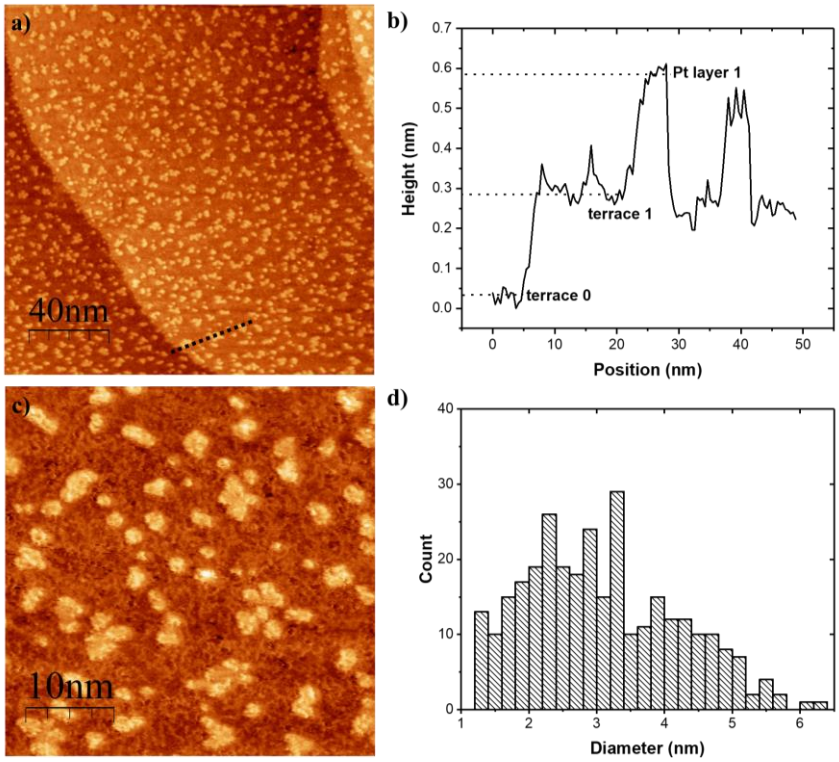


Figure 4.1: a) STM image of 0.2 ML Pt/Rh(111) deposited at RT at large scale showing terraces, step edges and islands. Dotted line corresponds to height profile in b). b) Height profile across step edge and onto islands, indicating monolayered islands. c) STM image at small scale of 0.2 ML Pt/Rh(111) deposited at RT, showing islands with narrow size distribution. d) Distribution of Pt islands sizes where diameter is plotted against counts.

### 4.1.2 Morphology of Pt/Rh(111) As-Prepared at 335 K and Post-Annealed to 700 K

Deposition of Pt on Rh(111) was then performed at 335 K. At this temperature the islands formed were dendritic (Figure 4.2 a)), similar to what was observed for Co/Re(0001) [41] and Au/Ru(0001) [42] at 300 K. By observing the larger islands, is was evident that islands followed three growth directions, and all islands were pointing in the same direction. Pt nucleated both on terraces, as well as along step edges. The average island size for Pt/Rh(111) at 335 K was significantly larger than for the islands grown at RT, and the size range was also broader. Coverage calculations indicate that 0.2 ML of Pt was formed on Rh(111). The height profile from Figure 4.2 b) shows a Rh step height of ca. 0.23 nm and Pt island height of slightly below 0.2 nm, corresponding to a bit less than one atomic layer of Pt.

The surface prepared at 335 K was PA to 700 K. Figure 4.2 c) shows how all the Pt went sub-surface and no islands were visible after annealing. This is similar to what is reported for Rh on Pt(111) [37], where PA to high temperature led to coverage loss and Rh went subsurface at 700 K. The height profile in Figure 4.2 d) shows a step edge height of ca. 0.21 nm for the Rh(111) surface.

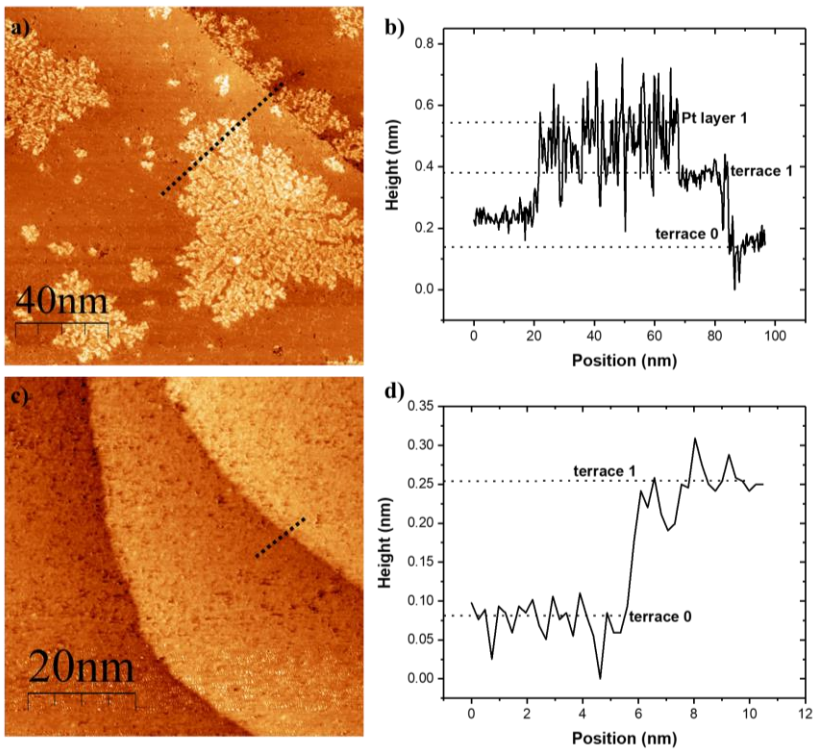


Figure 4.2: a) STM image showing 0.2 ML Pt/Rh(111) deposited at 335 K with dendritic islands. Dotted line corresponds to height profile in b). b) Height profile across dendritic island and step edge indicating monoatomic islands. c) STM image of 0.2 ML Pt/Rh(111) deposited at 335 K and PA to 700 K, all islands have gone subsurface. Dotted line corresponds to height profile in d). d) Height profile across step edge for Pt/Rh(111) showing step

### 4.1.3 Morphology of Pt/Rh(111) As-Prepared at 385 K

Deposition of Pt on Rh(111) was performed at 385 K. A transition from dendritic to more compact structures occured at around 385 K. A similar transition has been reported for Pt/Pt(111) [34]. The STM images in Figure 4.3 a) and b) show uniform nucleation and growth of Pt on Rh(111) on terraces and along step edges. Most of the islands had no defined shape, nor any clear facets. A few adopted a more triangular shape, similar to what was observed for Pt/Pt(111) deposited at 400 K [34]. The islands were smaller and had a narrower size distribution compared to the islands formed at 335 K. As shown by the island size distribution in Figure 4.3 d), the diameter ranged from approximately 1 - 12 nm, and a total coverage of 0.2 ML was calculated. As shown by the height profile in Figure 4.3 e), the islands were monoatomic, indicating a 2D growth mode. In addition, the islands seemed to have a somewhat lamellar domain structure as presented in Figure 4.3 c), with corresponding height profile in Figure 4.3 f). The height profile indicates an interlinear distance of around 0.4 nm and a height of around 0.06 ± 0.02 nm.

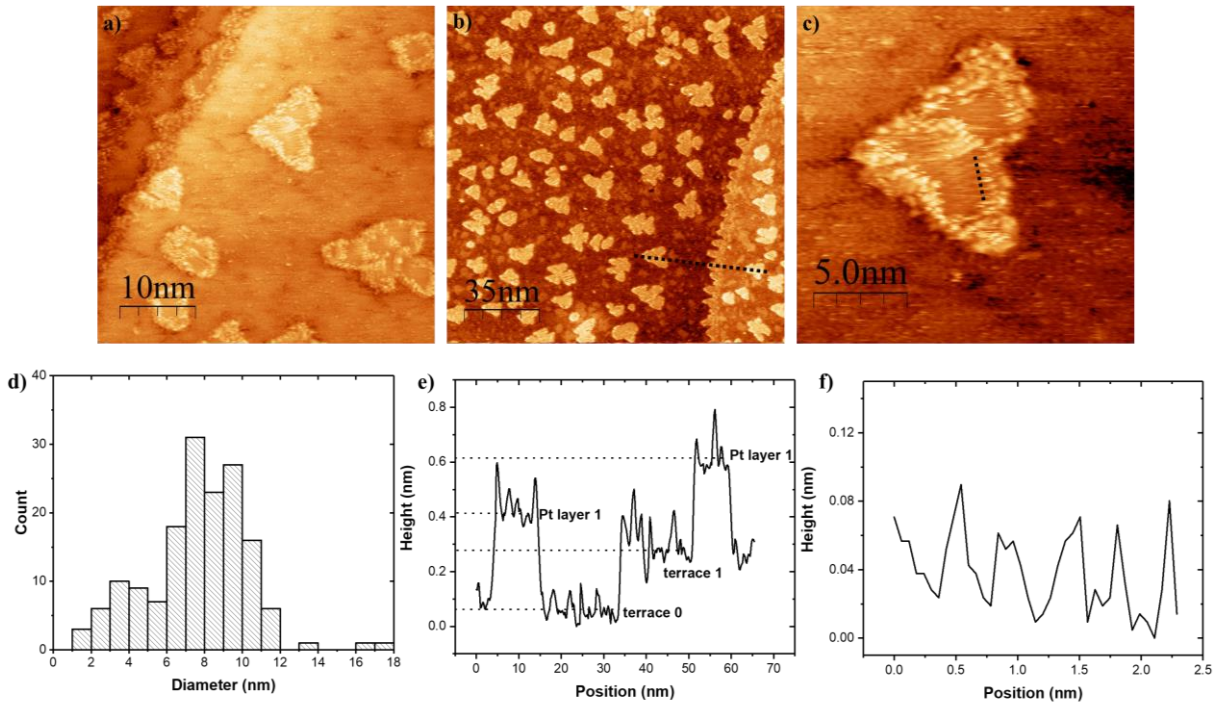


Figure 4.3: STM image 0.2 ML Pt/Rh(111) deposited at 385 K showing a) compact islands and step edges, b) overview of terraces and step edge, with narrow size distribution of islands, and nucleation along step edge. Dotted line corresponds to height profile in e). c) Lamellar domain structure inside a Pt island. Dotted line correspond to height profile in f). d) Distribution of Pt islands sizes showing diameter vs counts. e) Height profile across Pt islands and step edge. f) Height profile of lamellar domain structure showing a periodicity of ca. 0.4 nm and height of 0.06±0.02 nm.

### 4.1.4 Morphology of Pt/Rh(111) As-Prepared at 400 K and Post-Annealed to 600 K

Pt deposited on Rh(111) at 400 K resulted in more compact and faceted islands (Figure 4.4 a). Some of the islands were somewhat hexagonal, while most islands still had a slightly branched structure. Islands nucleated and grew both on terraces and along step edges, with monoatomic height, as indicated by height profile in Figure 4.4 b). This is in contrast to the Rh/Pt(111) system [37], where deposition of Rh at 400 K yielded both single- and double-layered islands. Compared to the islands formed at 385 K the size distribution was broader, with island sizes in the range 2 - 14 nm in diameter (Figure 4.4 c)). Coverage calculations yielded a coverage of 0.14 ML, which was less than for the lower temperature surfaces. As observed on the Pt/Rh(111) surface at 385 K, the islands exhibited a lamellar domain structure as can be seen in Figure 4.4 d), with height profile of the lamellar structure in Figure 4.4 e) showing a line separation of around 0.4 nm and a height of 0.04 ± 0.02 nm.

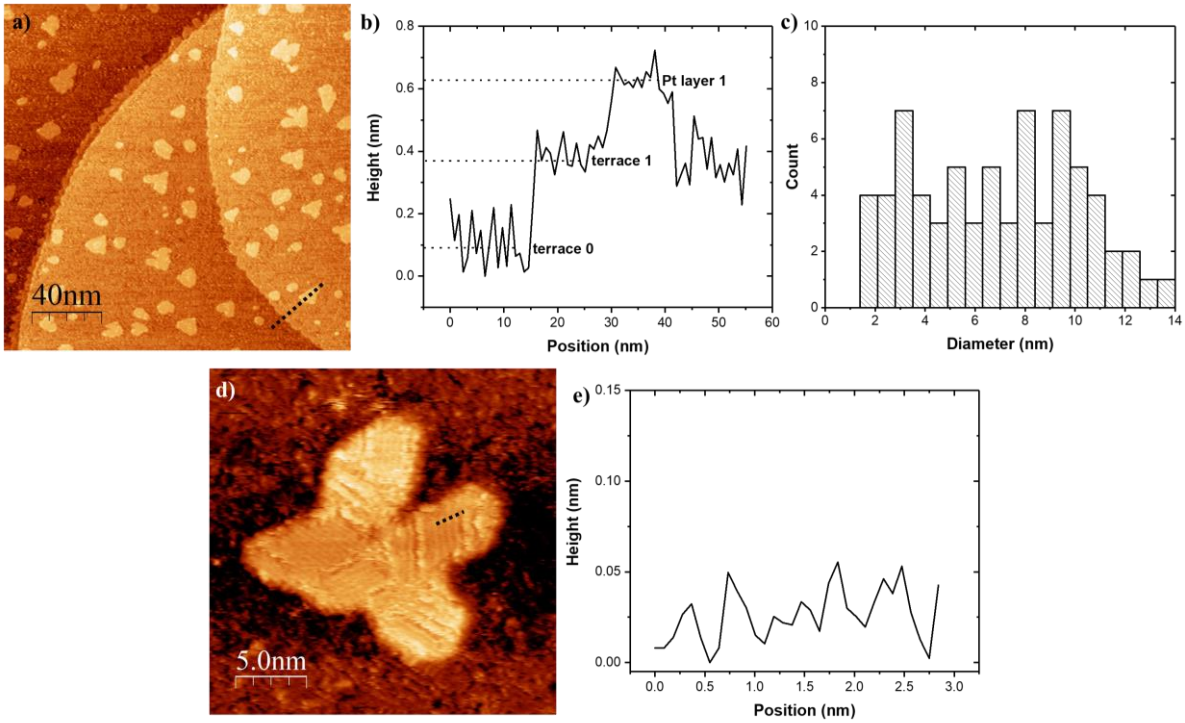


Figure 4.4: a) STM image of 0.14 ML Pt/Rh(111) deposited at 400 K, with overview of terraces, islands and step edges. Dotted line corresponds to height profile in b). b) Height profile across step edge and island, indicating monoatomic Pt islands. c) Size distribution of Pt islands, diameter is plotted against counts. d) STM image of lamellar domain structure of Pt/Rh(111) at 400 K. Dotted line corresponds to height profile in e). e) Height profile of lamellar structure showing a periodicity of ca. 0.4 nm and height of 0.04±0.02 nm.

Post-annealing to 600 K resulted in clear morphological changes. Pt islands became more compact with hexagon-like shape and were larger compared to the as-prepared sample (Figure 4.5 a)). This is similar to what was observed for the reverse system of Rh/Pt(111) at 400 K with PA to 700 K [37], where PA led to a restructuring to a hexagonal island shape. Most of the islands had increased in size, resulting in a broader size distribution (Figure 4.5 b)) with diameters in the range 2 - 20 nm. The step edges had gone from being rough to being smoother, due to healing of kinks. The Pt coverage had remained constant at ca. 0.14 ML, indicating no substantial subsurface diffusion at this temperature.

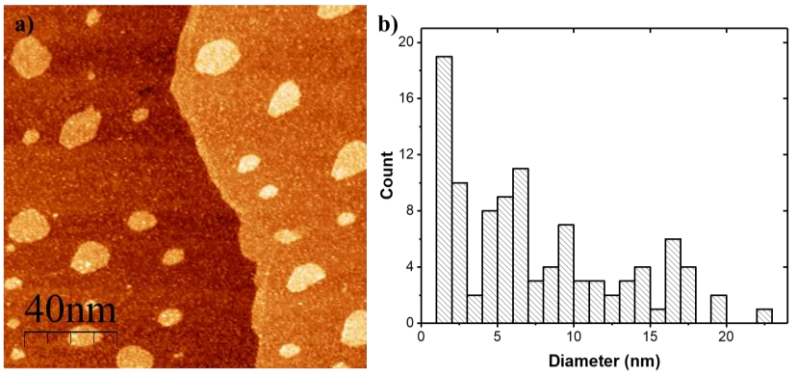


Figure 4.5: a) STM image of 0.14 ML Pt/Rh(111) deposited at 400 K with PA to 600 K, showing terraces, islands and step edges. b) Size distribution of island sizes showing a broader size distribution than for the as-prepared sample. Diameter is plotted against counts.

### 4.1.5 Morphology of Pt/Rh(111) As-Prepared at 425 K and Post-Annealed to 600 K and 700 K

Upon deposition of Pt on Rh(111) at 425 K, the resulting islands were hexagonal with nucleation occurring both on terraces and along step edges as Figure 4.6 a) shows, with a calculated coverage of 0.19 ML. This is somewhat similar to Rh/Pt(111) at 400 K, where a mix of island morphologies was obtained, including hexagons. Hexagonal islands was also reported for Pt/Pt(111) [34], but at a temperature of 455 K. The apparent height of the steps was about 0.23 nm (Figure 4.6 b)). At this temperature the islands grew in a 2D manner and some of the islands started to coalesce along certain facets to form larger islands. This was in contrast to Pt on Pt(111) [31] and Rh/Pt(111) [37], where islands showed a 3D growth mode at 425 K, and the onset for coalescence was reported to be at higher temperatures [31].

There was a slight variation in island sizes, but they typically ranged from 3 - 25 nm in diameter and they were overall larger than the islands obtained at 400 K and lower. The size distribution was also broader as indicated by Figure 4.6 c). Figure 4.6 d) shows how the lamellar domain structure was clearly seen at this temperature, and it is evident that the domain lines were parallel with the facets of the islands. Height profile for the lamellar structure is shown in Figure 4.6 e). As with the previous surfaces, the distance between lines was around 0.4 nm, but the height of lines was lower for this sample compared to the others, measured to be around 0.02 nm. This experiment was repeated four times, and the surface presented here was the first to be prepared. They will be compared in section 4.1.10 that elaborates on reproducibility of surfaces.

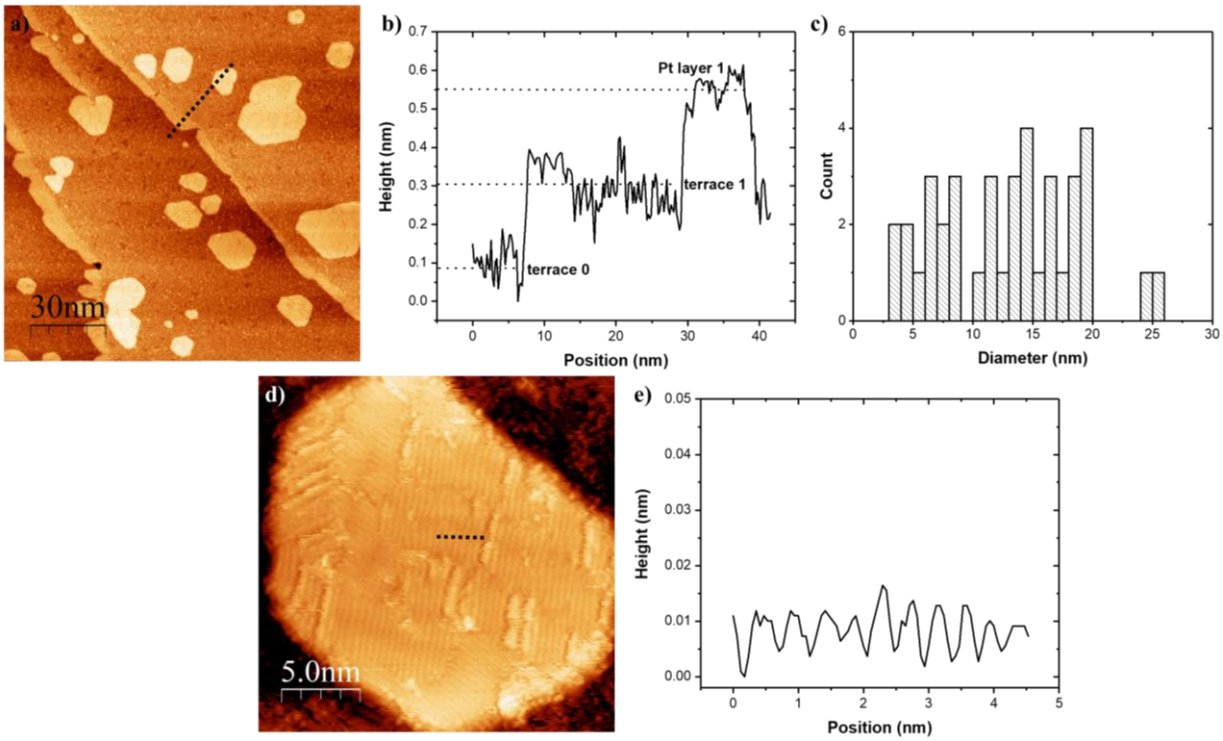


Figure 4.6: a) STM image of 0.19 ML Pt/Rh(111) at 425 K with islands, step edges and terraces. Dotted line corresponds to height profile in b). b) Height profile across step edge and island indicating monoatomic islands. c) Size distribution of islands with diameter plotted against counts. Indicates a broader size distribution, as well as larger islands. d) STM image of lamellar structure inside Pt islands. Dotted line corresponds to height profile in e). e) Height profile across lamellar structure, indicating interlinear distance of 0.4 nm, and a height of around 0.02 nm.

Upon post-annealing to 600 K, the islands became more rounded and smoothening along the step edges occurred (Figure 4.7 a)), indicating higher stability of compact islands. The island diameters were in the range 3 - 30 nm, indicating that some islands grew in size, and the size distribution was broader as seen in Figure 4.7 b). The coverage, however, remained constant upon PA. The island growth could be a result of further coalescence. This was similar to Rh/Pt(111) [37], where PA led to more rounding of islands and increase in island size. The stability of an island shape and coverage was also manifested in the lamellar structure, which remained visible upon PA (Figure 4.7 c)). Figure 4.7 d) shows the height profile of the lamellar structure, with line width of approximately 0.4 nm, as previously obtained, and a height of around 0.05 ± 0.01 nm. This was higher than for the AP surface, but more similar to what was observed for surfaces where Pt was deposited at lower temperatures.

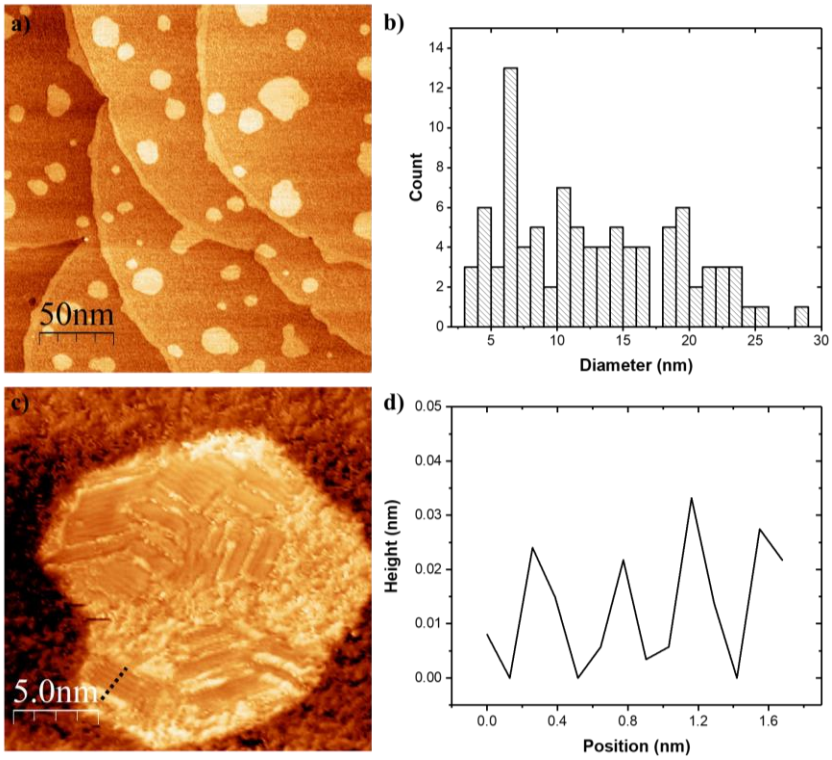


Figure 4.7: a) STM image of 0.19 ML Pt/Rh(111) at 425 K after PA to 600 K. Overview of terraces, islands and step edges. b) Size distribution of islands with diameter plotted against count. c) STM image of lamellar domain structure. Dotted line corresponds to height profile in d). d) Height profile for lamellar structure indicating interlinear distance of 0.4 nm, and a height of around 0.05 ± 0.01 nm.

To explore the effects of post-annealing to higher temperatures, a sample prepared at 425 K was post-annealed to 700 K. As Figure 4.8 a) shows, further rounding of islands and smoothening of edges was observed. But in contrast to the Pt/Rh(111) surface deposited at 335 K with PA to 700 K, Pt islands remained on the surface, similar to what was reported for Rh/Pt(111) with PA to 750 [37]. The island size was also increasing, with a very broad size distribution of 5 – 45 nm (Figure 4.8 b)). The lamellar structure was not be observed on this surface.

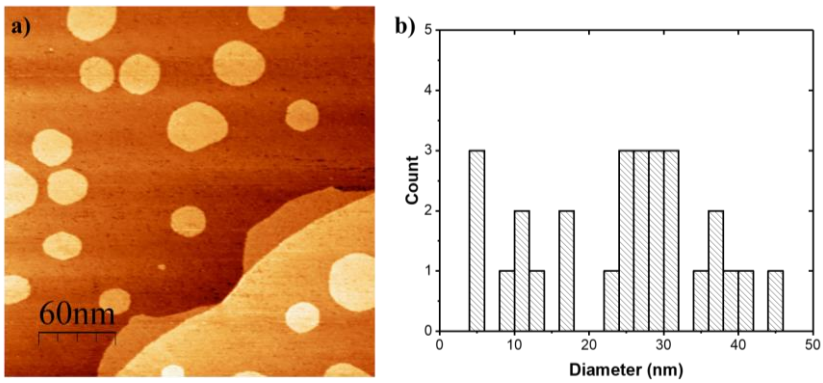


Figure 4.8: a) STM image of Pt/Rh(111) at 425 K after PA to 700 K, showing overview of islands, step edges and terrace. b) Size distribution of islands with diameter plotted against counts, showing a broad size range than AP or upon PA to 600 K.

### 4.1.6 Morphology of Pt/Rh(111) As-Prepared at 450K and Post-Annealed to 600K

Upon increasing deposition temperature from 425 K to 450 K, a change in island shape from hexagonal to triangular occurred as shown in Figure 4.9 a). A similar transition from hexagonal to triangular island was reported for Pt/Pt(111) [34] and Ru/Pt (111) [33], revealing preference of growth along a certain facet due to faster diffusion along one step edge compared to the other [34]. The nucleation and growth of Pt/Rh(111) at 425 K mainly occurred on the terraces with some growth along step edges. The average island size remained similar to what was observed at 425 K, from around 5 - 30 nm in diameter and a coverage of approximately 0.19 ML. The height profile in Figure 4.9 b) indicate formation of monoatomic Pt islands on Rh(111). Coalescence of islands, which was observed at 425 K, also occurred at 450 K (Figure 4.9 a)). Also at this temperature, the lamellar structure inside the islands was present, as seen in Figure 4.9 c). It had a periodicity of around 0.4 nm in width as previously seen, and a height of 0.03 ± 0.01 nm (Figure 4.9 d)).

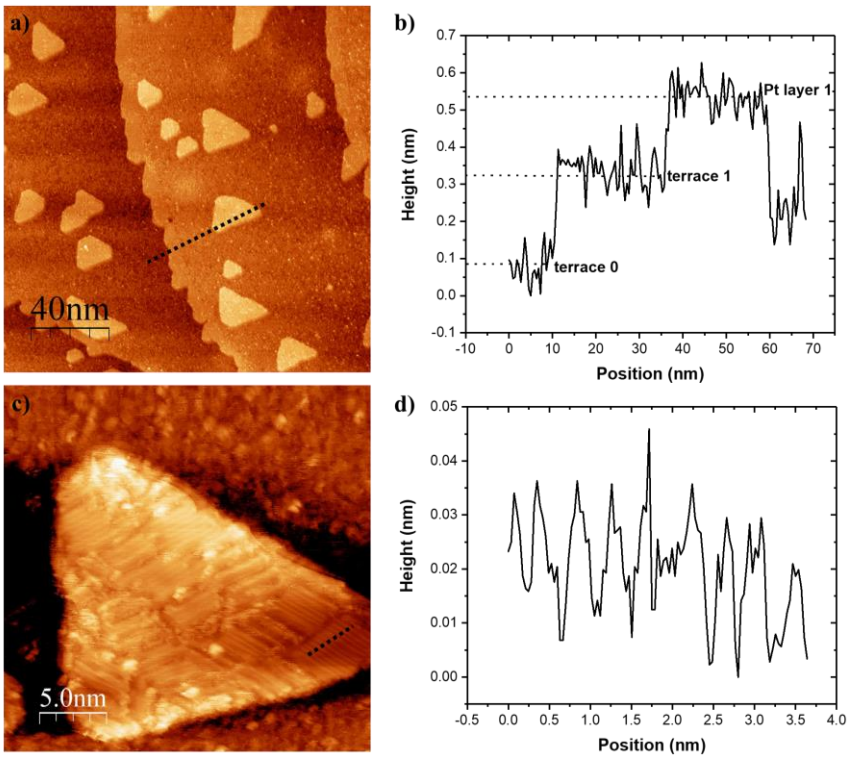


Figure 4.9: a) STM image of 0.19 ML Pt/Rh(111) at 450 K with islands, step edges and terraces. Dotted line corresponds to height profile in b). b) Height profile across step edge and island indicating monoatomic islands. c) STM image of lamellar structure on Pt/Rh(111) at 450 K. Dotted line corresponds to height profile in d). d) Height profile across lamellar structure, showing a distance between lines of ca. 0.4 nm and a height of around 0.03 ± 0.01 nm.

Post-annealing of the surface to 600 K led to a transition in island morphology from triangular to more round, with a lack of facets (Figure 4.10 a)). Pt residing along step edges was still visible, but the edges

had gotten significantly smoother with healing of kinks. Both island size distribution and surface coverage were in the same range as for the as-prepared surface. The lamellar domain structure was stable upon post-annealing to 600 K, shown in Figure 4.10 b). The height profile for the lamellar structure is presented in Figure 4.10 c), showing an interlinear distance of approximately 0.4 nm and a height of around 0.03 ± 0.01 nm.

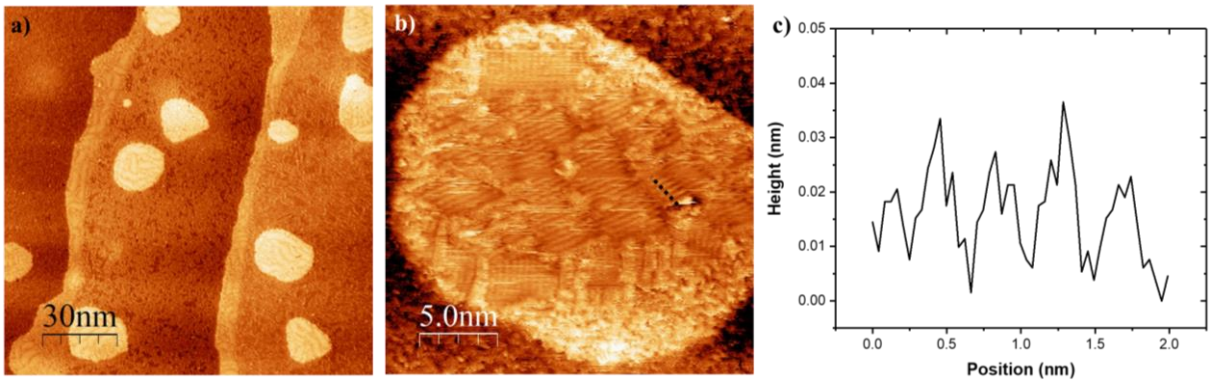


Figure 4.10: a) Pt/Rh(111) at 450 K with PA 600 K. Overview of terraces, islands and step edges. b) Lamellar domain structure remains upon PA. Dotted line corresponds to height profile in c). c) Height profile across lamellar structure with a interlinear distance of approximately 0.4 nm and a height of around 0.03 ± 0.01 nm.

### 4.1.7 Morphology of Pt/Rh(111) As-Prepared at 475K

The islands obtained upon deposition of Pt at 475 K were truncated triangles, all pointing in the same direction (Figure 4.11 a)). The islands were mostly located on the terraces. Some nucleation and growth of Pt along step edges could be observed, but the high temperature ensured smooth edges with healing of kinks. Coverage calculations gave approximately 0.09 ML, which was only half of what was obtained at lower temperatures. We believe this to be an outlier. As the height profile in Figure 4.11 b) shows, islands were monoatomic in height. The island size distribution was broad, with island diameters varying from 8 - 40 nm. For the surface prepared at 475 K, the lamellar structure in the islands was observed, and is depicted in Figure 4.11 c). Furthermore, the height profile across the lamellar structure in Figure 4.11 d) yields approximately the same values as previously obtained, with an interlinear distance of around 0.4 nm and a height of 0.03 ± 0.01 nm.

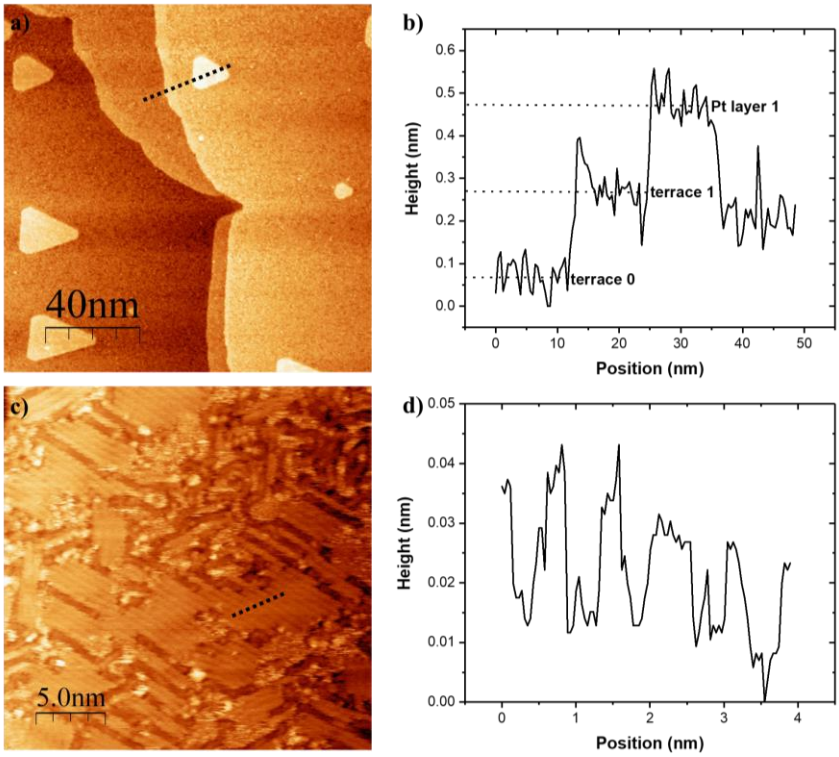


Figure 4.11: a) STM image of Pt deposited on Rh(111) at 475 K, with overview of terraces, islands and step edges. Dotted line corresponds to height profile in b). b) Height profile across step edge and island indicating monoatomic Pt islands. c) STM image of lamellar domain structure in Pt island. Dotted line correspond to height profile in d). d) Height profile across lamellar structure, showing interlinear distance of approximately 0.4 nm and a height of 0.03 ± 0.01 nm.

### 4.1.8 Morphology of Pt/Rh(111) As-Prepared at 500K and Post-Annealed to 600 K

Deposition of Pt on Rh(111) at 500 K led to similar triangular islands as obtained at 450 K and 475 K (Figure 4.12 a)). This was in contrast to Rh on Pt(111) [37] where an equilibrium hexagonal shape formed at this temperature. The islands mainly nucleated and grew on terraces, with some step decoration. No lamellar structure could be observed within the islands. It is uncertain whether it cannot be observed simply due to poor tip quality, or if it actually does not form at this temperature. The islands were quite large in size, ranging from 8 - 40 nm in diameter with a total coverage of approximately 0.17 ML, which was slightly lower than for lower temperatures (except 475 K). Unlike Rh on Pt(111) where multilayered islands can be found [37], Pt on Rh(111) at 500 K only forms single layered islands as can be seen in the height profile in Figure 4.12 b). As observed at 450 K, some of the islands coalesced together to larger units, which can clearly be seen in Figure 4.12 a).

Upon post-annealing, the islands remained somewhat triangular, but got slightly more rounded at the corners as can be seen in Figure 4.12 c). This is similar to what was obtained upon PA of 450 K surface. The coverage remained at ca. 0.17 ML and the island size distribution was in the range 10 - 40 nm in

diameter. The step edges got smoother, with healing of kinks. Although the lamellar domain structure could not be observed in the as-prepared surface, it was visible in the post-annealed surface. Although it was difficult to see in the images and the lines were blurry, the domain boundaries were visible, see Figure 4.12 d). A possible explanation is that only the domain boundaries were formed on this surface, and that the interior was flat, or it could simply be poor tip quality that enables us to observe the lines.

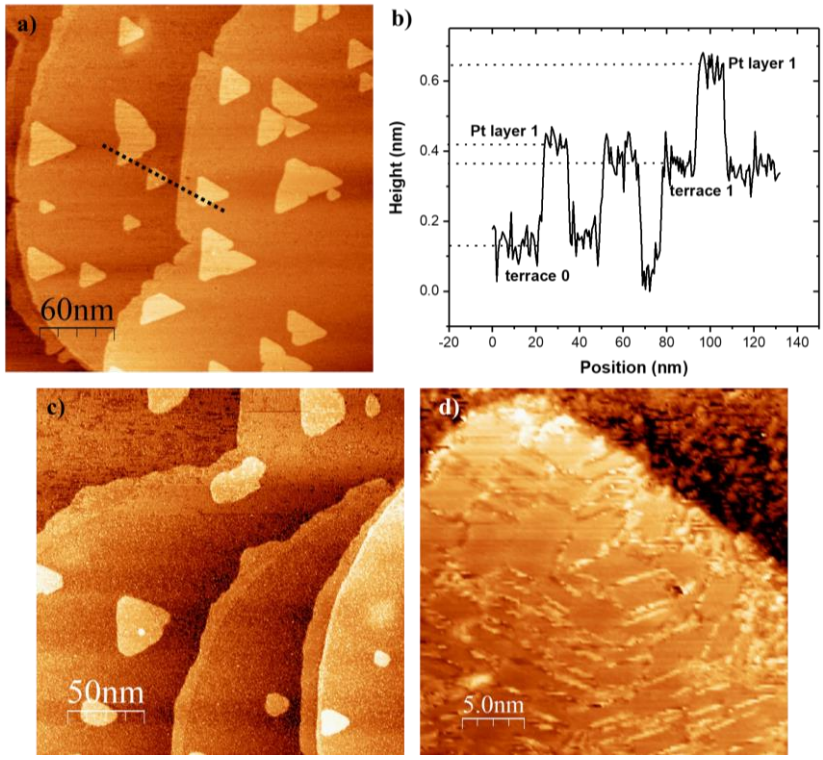


Figure 4.12: a) STM image of 0.17 ML Pt/Rh(111) at 500 K. Overview of islands, terraces and step edges. Dotted line corresponds to height profile in b). b) Height profile across islands and step edge indicating monoatomic islands. c) STM image of 0.17 ML Pt/Rh(111) deposited at 500 K and PA to 600 K. d) STM image of lamellar domain structure for PA surface. Lines cannot be seen, but domain boundaries are visible.

### 4.1.9 Morphology of Pt/Rh(111) As-Prepared at 600 K and Post-Annealed to 600K and 650 K

The highest deposition temperature used was 600 K. The island shape differed significantly from islands obtained at lower temperatures. No defined structure nor faceting of island edges was observed at 600 K, but large, worm-like structures formed, as shown in Figure 4.13 a). In addition, the number of islands on terraces had significantly been reduced and the coverage was around 0.07 ML. At this temperature there was a strong preference for step decoration, also forming worm-like features. In the Rh/Pt(111) system, Zheng et al. [37] explained that the reduction of Rh coverage on Pt(111) terraces was a result of increased subsurface diffusion of Rh, and this effect may also have played a role in the Pt/Rh(111) system. The height profile in Figure 4.13 b) shows that the islands formed were monoatomic in height.

The lamellar domain structure could be observed in some parts of the islands as indicated by Figure 4.13 c), but it was not as visible as in the surfaces prepared at lower temperatures. However, some structuring with a height of around 150 pm was observed on the Rh(111) terraces, and a linear structure was observed in the background; see Figure 4.13 d) – e). The height profile for the lines is shown in Figure 4.13 f), which had an interlinear distance of approximately 0.4 nm and a height of around 0.07 nm, somewhat similar to the values obtained for the lamellar domain structure. These lines, however, all seemed to follow the same direction, and no clear domains were formed.

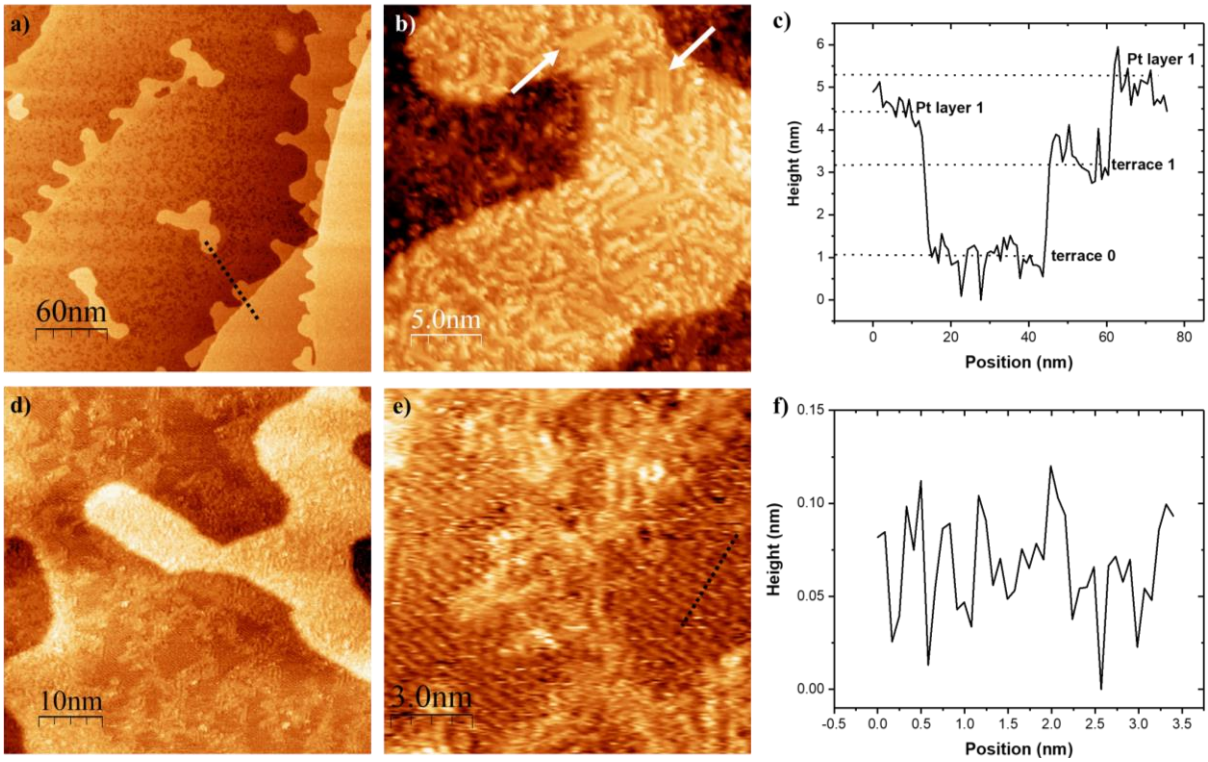


Figure 4.13: a) STM image of 0.07 ML Pt/Rh(111) at 600 K, overview of islands, terraces and step edges. Dotted line corresponds to height profile in c). b) STM image showing close-up of Pt island with arrows indicating small domains of lamellar structure. c) Height profile across Pt island and two step edges. d) STM image of Pt island with background structure on Rh(111) terrace. e) STM image of lines on Rh(111) terraces. Dotted line corresponds to height profile in f). f) Height profile of linear structure on Rh(111) terrace showing periodicity of ca. 0.4 nm and height of around 0.07 nm.

Post-annealing was performed at 600 K and STM images collected (see Figure 4.14 a)), then the same surface was post-annealing a second time at 650 K before new STM images were collected (see Figure 4.14 b)). The first post-annealing led to rounding of islands, and smoothening of step edges, and the second PA brought even further smoothing of edges and islands. The coverage seemed to remain at around 0.07 ML and the island were in the range 15 - 50 nm in diameter. No clear lamellar domain structure could be seen on these surfaces, neither could the linear background structure that was observed in the AP surface.

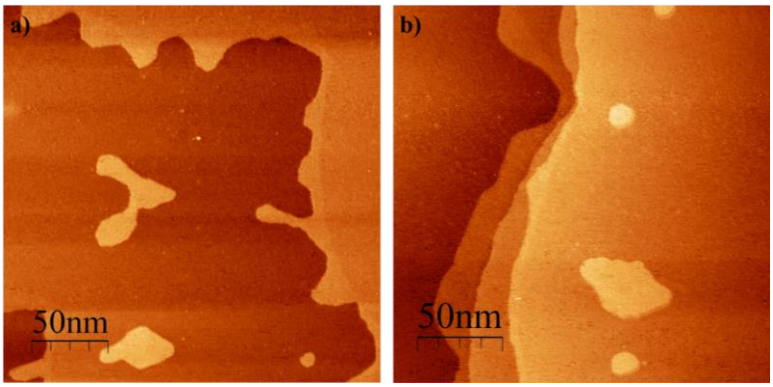


Figure 4.14: STM images of PA surfaces of 0.07 ML Pt/Rh(111) deposited at 500 K. a) PA at 600 K. b) Same surface as in a) after a second round of PA to 650 K.

### 4.1.10 Reproducibility in Surface Preparation Using the Reactor STM

As previously mentioned, the deposition of Pt on Rh(111) at 425 K was repeated four times. This was done to check the reproducibility of surface preparation by using the Reactor STM, and to see if using the same apparent conditions would produce the same morphology and surface coverage. Figure 4.15 a)-d) show the four surfaces prepared. The common feature for all surfaces was that islands formed were not very dendritic, but rather compact. In addition, all surfaces showed nucleation and growth along step edges. The main difference was the average island size, especially the surface prepared in November 2019 (Figure 4.15 b).

Overall, the surfaces prepared in May 2019, November 2019 and February 2020 (Figure 4.15 a) and c)-d)), yielded similar surface morphologies with faceted, hexagon-like shaped islands, with some nucleation and growth along step edges. Island sizes and coverage were in the same range for the May 2019 and November 2019 experiment, with diameters ranging from 5 - 25 nm, and coverages of 0.19 ML and 0.18 ML, respectively. The February 2020 had smaller islands, and a lower coverage of 0.14 ML. The surface from September 2019, shown in Figure 4.15 b) had larger, but fewer islands and more branched structures. This is similar to what is typically observed for deposition at lower temperatures. In addition, the step edges were much rougher. Differences in morphology can be explained by surface cleanliness and quality of UHV during preparation, or possible inaccurate temperature readout due to poor thermocouple connection. The only surface where the lamellar structure could be observed was the one from May 2019.

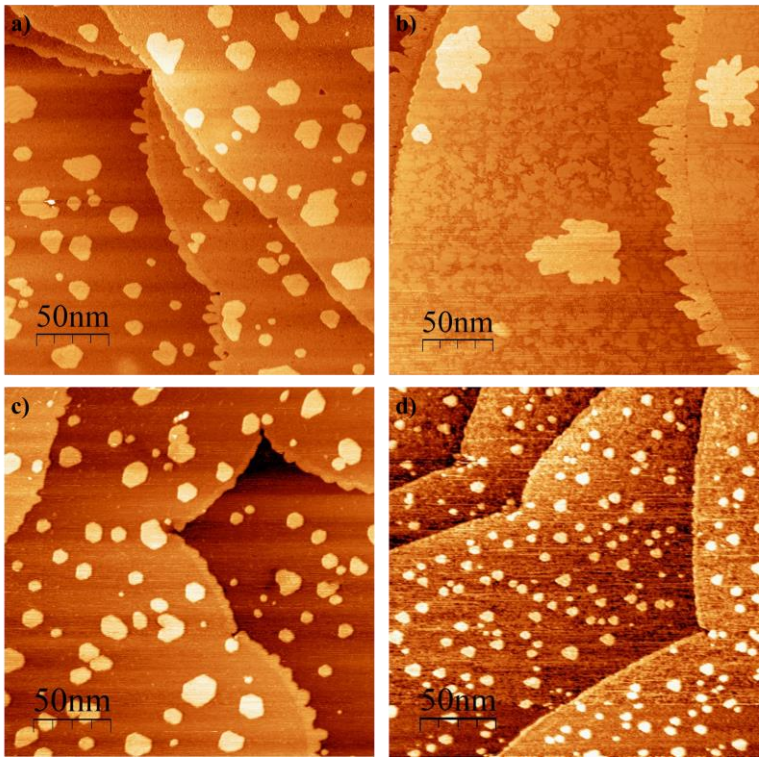


Figure 4.15: STM images of four surfaces prepared at the same conditions; Pt deposited on Rh(111) for 5 min at 425 K. Surface prepared in: a) May 2019, b) September 2019, c) November 2019, d) February 2020.

One of the challenges with these experiments is to obtain the exact same conditions when wanting to reproduce an experiment. Changes in conditions such as pressure, contaminations on surface, and temperature readout will alter the outcome of the experiment, and surfaces that supposedly should look the same can end up a bit different. In addition, viewing fine details such as lamellar structure heavily depend on tip quality. The variation in the surfaces prepared indicate that we are working in a temperature range where there are transitions in surface morphology, and hence the surface structure heavily depends on the real temperature used upon deposition. Although there are outliers we see that there are many similarities between the surfaces, which allows us to conclude that it is possible to reproduce the surfaces.

### 4.1.11 Synthesis Strategy Roadmap for Preparing Pt-Rh Surfaces

A “synthesis strategy roadmap” (Figure 4.16) was created to guide preparation of well-defined Pt-Rh nanostructured surfaces. It indicates the preparation conditions used, and explores the effects of deposition temperature and post-annealing. The results are also summarized in Table 4.1. As the roadmap and the table indicates, the deposition temperature strongly influences the resulting island morphology, including shape and size. It also affects the resulting coverage, as shown in Figure 4.17. Post-annealing also shows a strong influence on the surface morphology. Effects of evaporation rates and coverages were not explored when creating the roadmap.

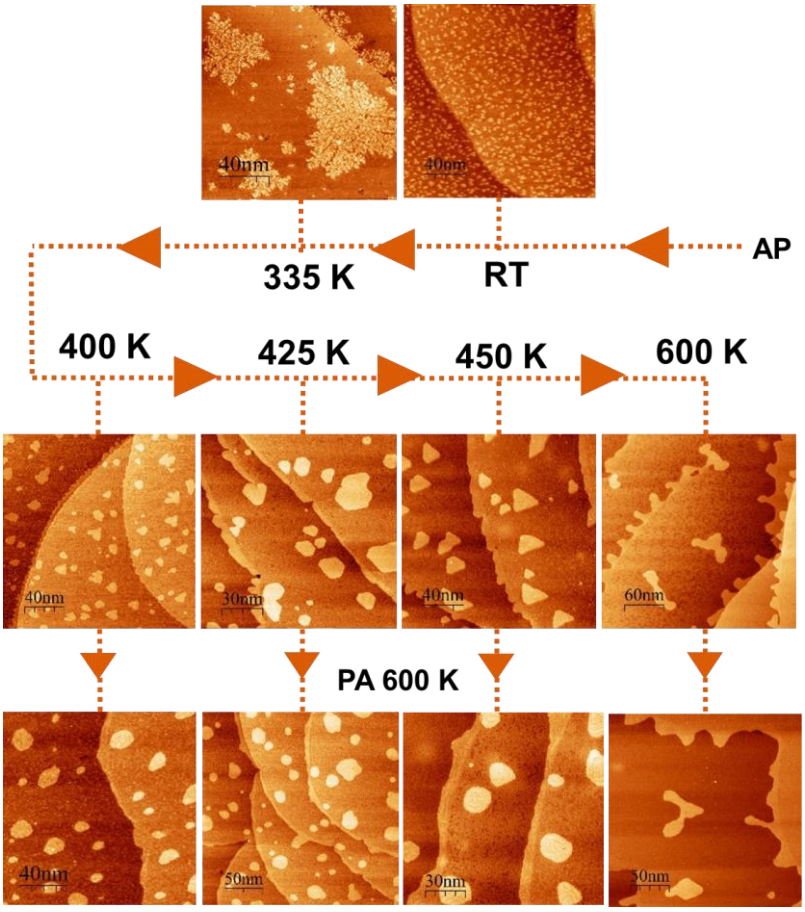


Figure 4.16: Roadmap for Pt/Rh(111) surfaces. Deposition temperature strongly influences the obtained surface morphology. PA also plays a crucial role in surface preparation.

Table 4.1: Summary of Pt/Rh (111) surfaces obtained by varying deposition temperature and post-annealing.

| **Deposition Temp., K** | **Island Shape, As-Prepared** | **Island Size, Diameter, nm** | **Island Shape, PA to 600 K** | **Island Size, PA to 600 K, Diameter, nm** |
|---|---|---|---|---|
| RT | Small branched | 1 – 6 | - | - |
| 335 | Dendritic | - | - | - |
| 385 – 400 | Branched compact | 1 – 14 | Hexagonal | 2 – 20 |
| 425 | Hexagonal | 3 – 25 | Hexagonal/Round | 3 – 30 |
| 450 – 500 | Triangular | 5 – 40 | Hexagonal/Round | 10 – 40 |
| T > 600 | Worms | 20 – 60 | Worms/Round | 15 – 50 |

As indicated by Figure 4.16 and Table 4.1, the island shape is strongly influenced by deposition temperature, starting with dendritic islands at low temperature. In the temperature range 385 - 400 K the islands become more compact, and a transition occur at around 425 K, resulting in well-defined, faceted islands. These are retained until 600 K, where worm-like structures form. At all deposition temperatures, Pt decoration along step edges was seen, and islands showed 2D growth. As indicated by Figure 4.17, coverage decreases as deposition temperature increases. It should be noted that the amount of Pt

nucleated along the step edges were not part of the calculated coverage. STM images indicate that there is a increased tendency to nucleate here with increased coverage, explaining the apparent coverage drop with temperature. Mobility increases with temperature, and hence diffusion of Pt to step edge before nucleation might be energetically more favorable.

PA led to a reshaping of the islands, resulting in a mix of hexagonal and rounded islands. Cluster growth occurred on all surfaces, but there was no apparent change in coverage, as indicated by Figure 4.17. The lack of coverage loss for the compact islands upon PA reveals the high stability of the surfaces. A high stability is important for operando studies so that reconstructions can be attributed to gas species present. It could also be suggested that there is some alloying with Rh, where Rh diffused to the surface, as was observed for the reverse system (Rh/Pt(111)) [37]. This process would not necessarily be observed by STM, since the coverage loss of Pt would be replaced by increased Rh at surface. However, literature have reported that surface segregation is excepted for Pt on Rh(111) [38], so we expect Pt to remain at the surface and not go subsurface. XPS is needed to confirm this.

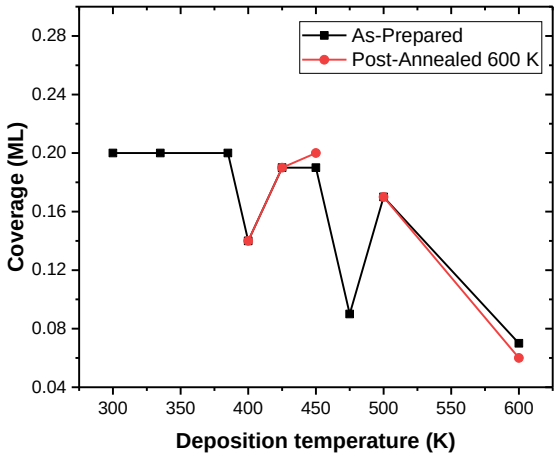


Figure 4.17: Evolution of coverage (ML) with deposition temperature. Grey line corresponds to AP surfaces, and red line to surfaces upon PA to 600 K. Graph indicate a gradual loss of surface coverage with increasing deposition temperature, but PA does not seem to have an influence on coverage.

Although the compact islands were thermally stable, the dendritic islands formed at lower temperatures were unstable upon PA. The dendritic islands formed at 335 K underwent complete subsurface diffusion upon PA to 700 K, while the more faceted, compact Pt islands obtained upon deposition at 425 K, were still visible after PA to 700 K. Hence in order to form thermally stable islands of Pt on Rh(111) deposition should be performed at sufficiently high temperatures. Comparison of the surface prepared by direct deposition at 600 K and of the surfaces PA to 600 K shows that the two preparation routes yield very different structures. Direct deposition at 600 K led to worm-like structures, while the islands obtained upon PA to 600 K were more faceted. Also islands PA to 700 K show strong deviation from high temperature depositions.

## 4.2 High Coverage Surfaces

In this section we describe the surface morphology of high coverage surfaces of Pt/Rh(111). This was done in order to explore how increased Pt coverages on Rh(111) affected growth and morphology. Deposition was performed at 425 K with a flux of approximately 0.030 ± 0.005 ML/min for all surfaces. All surfaces (except 0.43 ML) were PA to view its effect on morphology. In addition, the high coverage surfaces were used to study how increased Pt coverages on Rh(111) altered oxidation. The oxidized surfaces are described in section 4.3. STM images of the AP and PA surfaces are shown in Figure 4.18.

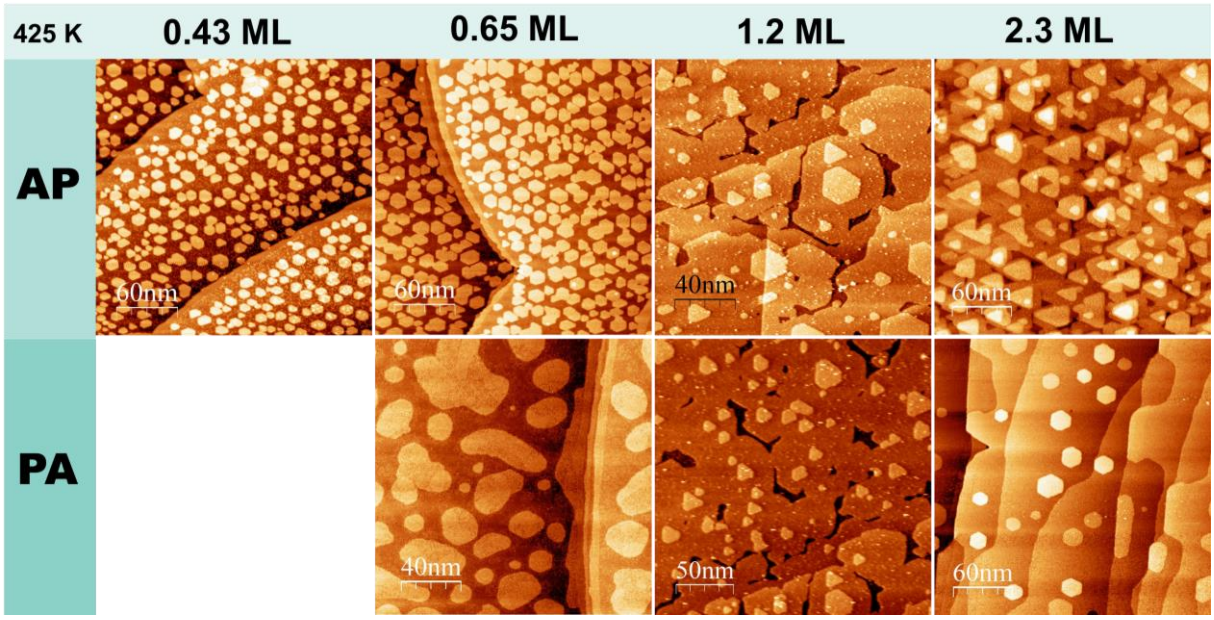


Figure 4.18: Overview of surfaces obtained by depositing Pt on Rh(111) at 425 K with coverages of 0.43, 0.65, 1.2 and 2.3 ML. Upper panel shows AP surfaces, and lower panel shows PA surfaces.

The coverage of the AP surfaces (upper part of Figure 4.18) was measured to 0.43 ± 0.03 ML, 0.65 ML ± 0.05 ML, 1.2 ± 0.2 ML and 2.3 ± 0.3 ML. The 0.43 – 1.2 ML surfaces showed growth of mostly hexagonal islands. On the 1.2 ML surface some islands also had a more triangular shape. A mix of island shapes has also been reported for Rh/Pt(111) at 400 K [37] and Ru/Pt(111) at 523 K [33]. For the 2.3 ML surface, the islands formed on the 1$^{st}$ and 2$^{nd}$ layer counted from the top were mostly triangular, all pointing in the same directions. Some hexagonal islands and truncated triangles could also be seen. All islands were monolayered on the 0.43 ML surface, while on the 0.65 ML surface some double-layered islands started to form. This indicate a quasi-2D growth at 425 K, which is also seen for Pt/Pt(111) [31]. For both the 1.2 ML and 2.3 ML surfaces, a second layer started to grow before the preceding one was completed, confirming a quasi-2D growth.

The 0.65, 1.2 and 2.3 ML surfaces were PA to 700, 600 and 700 K for 10, 5 and 20 min, respectively (lower part of Figure 4.18). For all surfaces PA promoted lateral growth and coalescence of islands to

large units. For the 0.65 ML surface, the coverage had decreased to 0.56 ± 0.03 ML and the islands had lost their defined shape, and the sharp facets had been replaced with more rounded island edges. In addition, the step edges had gotten smoother. For the 1.2 ML surface, which was annealed to a lower temperature and for a shorter time, the islands in the second layer were still present and the island shape had remained hexagonal. For the 2.3 ML surfaces the Pt islands in the lower-lying layer had coalesced further, completely covering the Rh(111) terraces. Some Pt islands were still visible on the 2.3 ML surface, but had changed from a triangular to a hexagonal shape. As shown in Figure 4.19 a – b), some of the islands were single layered and some were double layered, with the second layer completely covering the first layer. Although the lamellar structure was not observed in any of the AP surfaces, it was present for the 2.3 ML surface upon PA. The lamellar structure was observed only in a limited area along a step edge (Figure 4.19 c)).

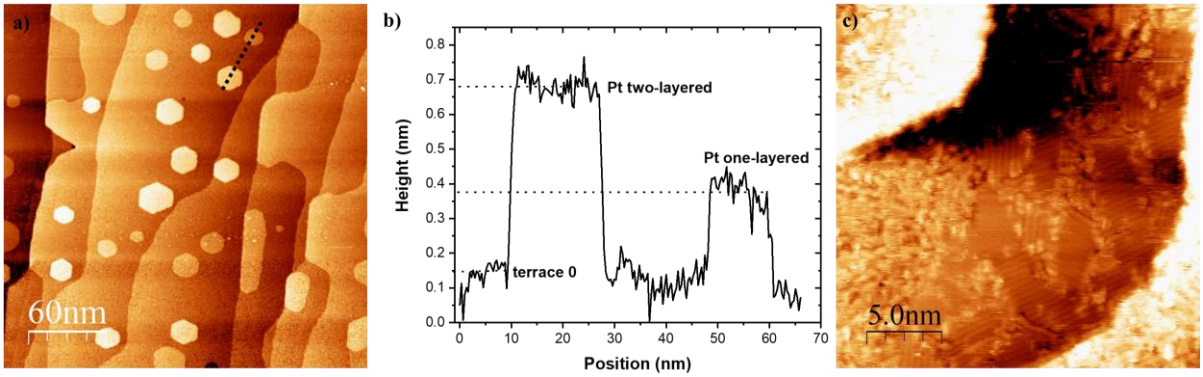


Figure 4.19: a) STM image of PA 2.3 ML Pt/Rh(111), dotted line corresponds to height profile in b). b) Height profile indicating single- and double-layered Pt islands. c) Lamellar structure observed on a limited area.

LEED of the AP and PA 0.65 ML surface in Figure 4.20 shows a hexagonal diffraction pattern with bright, sharp spots, with no changes visible upon PA. This indicates that both surfaces are crystalline with epitaxial grown Pt on Rh(111), which is representative for all surfaces described above.

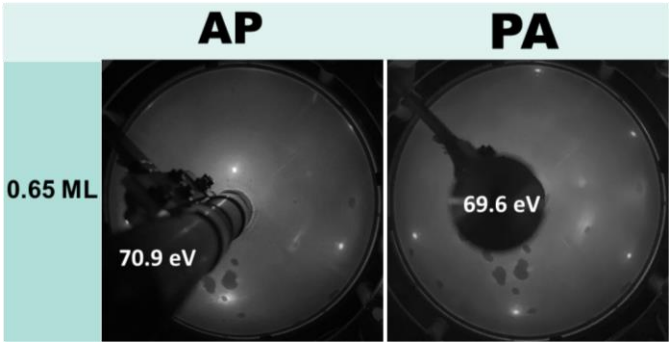


Figure 4.20: LEED of 0.65 ML Pt/Rh(111) for AP and PA surface taken at 70.9 and 69.6 eV, respectively. Diffraction pattern indicate crystalline surface with epitaxial grown Pt on Rh(111).

In order to study the influence of high deposition temperatures, 1.2 ML Pt was deposited on Rh(111) at a substrate temperature of 700 K. Comparing 1.2 ML Pt/Rh(111) deposited at 425 K and 700 K (Figure 4.21) shows that there was a shift to a more 2D growth mode by increasing deposition temperature. On the 700 K surface, no islands were visible and continuous Pt layers formed on the Rh(111) terraces.

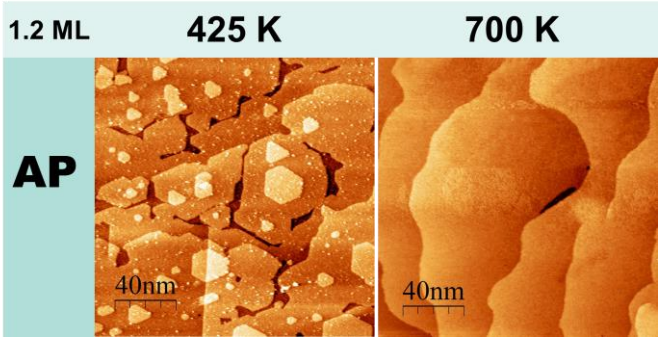


Figure 4.21: Comparison of AP 1.2 ML Pt/Rh(111) deposited at 425 K and 700 K to view influence of deposition temperature. Higher temperature makes the growth mode change to more 2D.

In conclusion we observe that by keeping the deposition temperature constant, but increasing the coverage the island morphology remains similar, and a quasi 2D-growth occurred for Pt/Rh(111) at 425 K. PA time and temperature, however, highly influence the amount of change on the surface. PA to 600 K for 5 min did not alter the surface considerably, while PA to 700 K for 10-20 min resulted in significant morphological changes. The change when going from 600 to 700 K indicates that there is a transition temperature in this range. The importance of temperature is also illustrated by changing the deposition temperature from 425 to 700 K (Figure 4.21), where the 700 K surface resulted in a completely different surface morphology than the 425 K surface.

## 4.3 Oxidation of Pt-Rh Surfaces

It is well-known that the catalytic activity of a material can be correlated to oxide species present on the surface [30, 61, 63]. Therefore, it is interesting to study the behavior and morphological changes of surfaces is oxygen atmospheres. In order to do this, we use a selection of the surfaces described in section 4.1 and 4.2, and investigate the changes in surface structure and oxidation behavior when varying the Pt coverage on Rh(111). Some of the surfaces were studied by means of UHV STM and LEED (4.3.1), and others using Reactor STM operated at 1 bar (4.3.2).

### 4.3.1 Morphology of Oxidized Pt/Rh(111) Surfaces

A number of surfaces were exposed to an oxidizing environment before characterization in UHV by means of STM and LEED. The surfaces studied were clean Rh(111) and 0.14, 0.43, 0.65 and 2.3 ML Pt deposited on Rh(111) at 425 K. All surfaces had been PA to 700 K for 10 min (20 min for 2.3 ML

surface). All surfaces were then oxidized in $1.0 \times 10^{-3}$ mbar $O_2$ at 700 K for 20 min. A more detailed description of the surfaces AP and PA is presented in section 4.1.5 and 4.2. The STM images in Figure 4.22 show the evolution of AP surfaces. The clean Rh(111) surface displayed large, flat terraces with no sign of islands. Upon deposition of 0.14 – 0.65 ML Pt on Rh(111), monolayered hexagonal islands formed, with some nucleation along step edges. Deposition of 2.3 ML Pt on Rh(111) indicated a quasi-2D growth, with formation of triangular islands in the top-most layers.

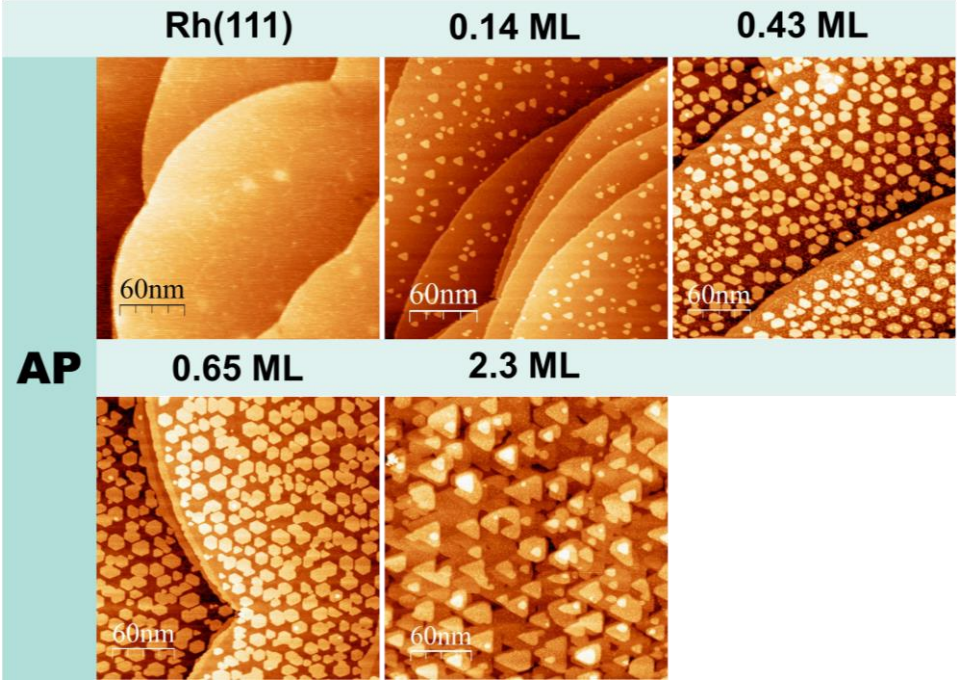


Figure 4.22: STM images of AP surfaces starting with clean Rh(111), and then Pt deposited on Rh(111) at 425 K with gradual coverage increase from 0.14 ML up to 2.3 ML.

The evolution of LEED pattern for AP, PA and oxidized surfaces can be seen in Figure 4.23. The AP surfaces displayed a hexagonal LEED pattern with sharp, bright spots indicating a clean and crystalline surface. There was no evident change in the LEED pattern upon PA for any of the surfaces. However, upon oxidation, the clean Rh(111) surface and the 0.14 – 0.65 ML Pt/Rh(111) surfaces displayed a moiré pattern formed by two superimposed hexagonal structures. This indicates that a surface oxide formed on the substrate. For the 2.3 ML surface, oxygen exposure did not result in formation of moiré pattern, and the LEED pattern was similar to what was observed for AP and PA surface. This implies that the surface oxide did not form on the 2.3 ML surface. Gustafson et al. [68], and multiple other studies [69, 70] reported formation of a ultra-thin $RhO_2$ surface oxide on Rh(111), which was obtained at the same oxidation conditions used in this experiment. Upon formation of the reported surface oxide, the LEED displayed an identical moiré pattern to the one observed for oxidized Rh(111) and 0.14 - 0.65 ML Pt/Rh(111), shown in the lower panel of in Figure 4.23. The moiré pattern was also visible in STM images. The high Pt content on the 2.3 ML surface suggests oxidation will happen via Pt, which is reported to require higher oxygen pressures, temperature and/or exposure time [56, 57, 60].

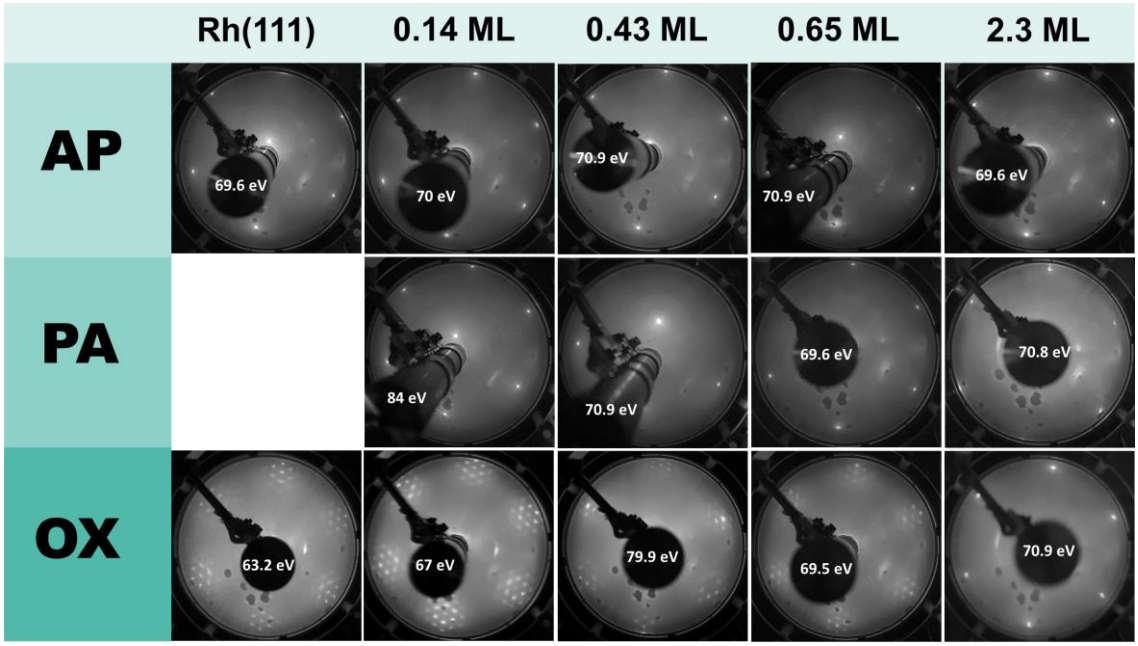


Figure 4.23: LEED of AP, PA and oxidized surfaces for clean Rh(111), and 0.14 – 2.3 ML Pt/Rh(111). All AP and PA LEED patterns were similar. Upon oxidation, a moiré pattern was formed revealing presence of a surface oxide. LEED of 2.3 ML surface after oxygen exposure did not display a moiré pattern.

The STM images in Figure 4.24 show the evolution of surface morphology upon oxidation. For 0.14 – 0.65 ML surfaces, oxidized surfaces revealed an increase in Pt island size. Islands had coalesced together and lost some of the defined shape seen in the AP surfaces. Growth was both lateral and vertical, which could be seen by formation of two-layered island. Lateral growth is expected to be initiated already upon PA to 700 K (see section 4.2) [37].

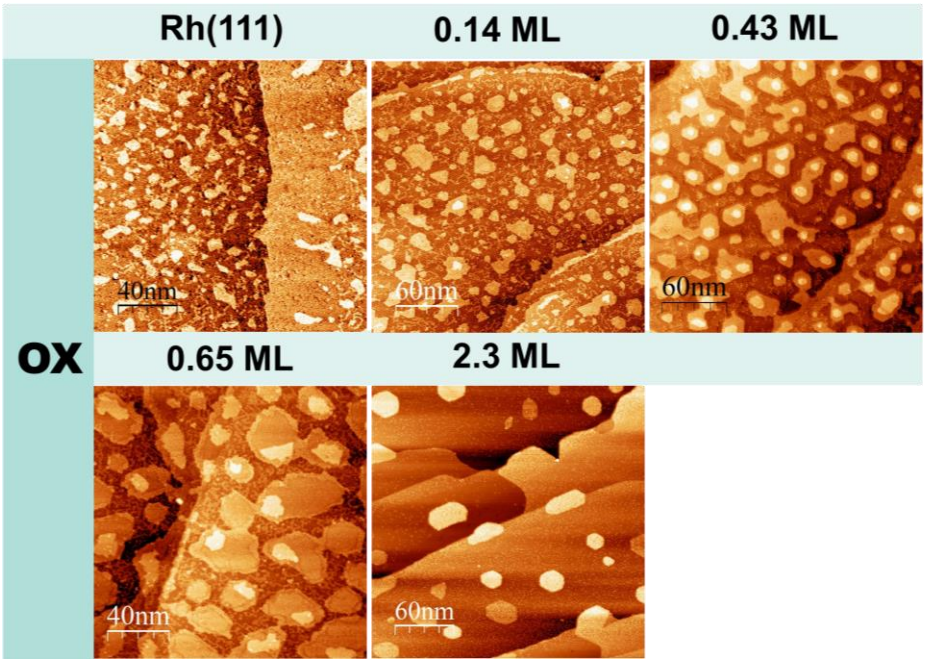


Figure 4.24: STM images of 0 – 2.3 ML Pt/Rh(111) after oxidation revealing growth of islands, both vertically and laterally. 2.3 ML surface did not change significantly compared to PA surface.

Also on the Pt-free Rh(111) surface, oxidation resulted in vertical growth, and islands were observed. This indicates that the vertical growth is a result of ad-island formation from excess Rh due to surface oxide formation. The surface oxide has a lower density compared to bulk Rh, that will drive up some of the Rh [63]. This is verified by the coverage increase for clean Rh(111) and for the 0.14 – 0.65 ML Pt/Rh(111) surfaces (Figure 4.25 a)). For clean Rh(111), 0.22 ML of the Rh(111) surface was covered by ad-islands. For the 0.14 ML surface, oxidation resulted in a coverage increased to 0.42 ML, with approximately 0.008 ML located in the second layer. On 0.43 ML surface, the total coverage had increased to 0.52 ± 0.02 ML, with the second layer of the islands covering about 0.067 ± 0.003 ML of the surface. After oxidation, the 0.65 ML surface had a coverage of 0.80 ± 0.04 ML, with the second layer covering approximately 0.081 ± 0.007 ML of the surface.

The ad-island on clean Rh(111) mostly decorated the terraces and had irregular shapes. On the 0.14 ML surface the ad-islands could be seen on terraces, along step edges, and on the Pt islands revealed by formation of two-layered islands, which were not present on the AP surface. Also here the islands had no clear shape. For the 0.43 and 0.65 ML surfaces, the lower-lying islands had lost their defined shape, but for the 0.43 ML surface the second-layer islands were hexagonal. On the 2.3 ML surface, islands had changed shape to more rounded, but there was not expected any ad-island due to the lack of surface oxide formation, as observed by LEED. The 2.3 ML surface did however show presence of two-layered islands, where the second layer completely covered the first layer, shown by the height profile in Figure 4.25 b).

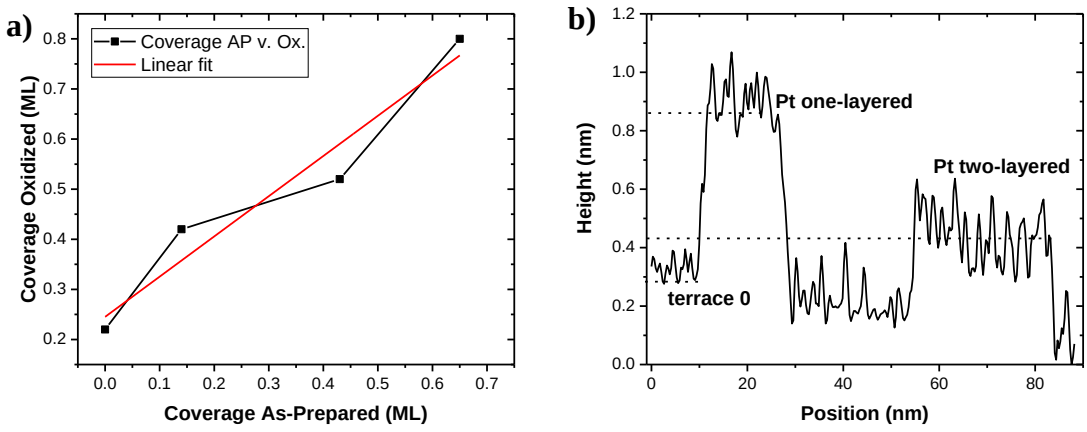


Figure 4.25: a) Nominal v. total coverage of 0 – 0.65 ML surfaces after oxidation indicating coverage increase for all four surfaces. b) Height profile of 2.3 ML Pt/Rh(111) after oxygen exposure showing presence of double-layered islands.

The evolution of moiré pattern on the oxidized surfaces can be seen in Figure 4.26. For the clean Rh(111) the moiré pattern covered the entire surface, both Rh(111) terraces and ad-islands. Upon deposition of 0.14 ML Pt, the moiré pattern still covered terraces and islands, both in the first and second island layer.

On the 0.43 ML surface, the amount of surface covered with moiré had significantly reduced and could mainly be observed on the Rh(111) terrace between the islands, and some on the island edges. However, no moiré was visible in second layer of islands. Following the trend of the 0.43 ML surface, the amount of moiré had been reduced even further on the 0.65 ML surface. The moiré was now restricted to the areas along islands edges, and there was no sign of moiré on the Rh(111) terraces between the islands. The lack of moiré along the step edges can be caused by high Pt content due to diffusion, as was observed by Duisberg et al. [43]. We see that with increasing Pt content, there is a consistent reduction of moiré pattern visible in the STM images.

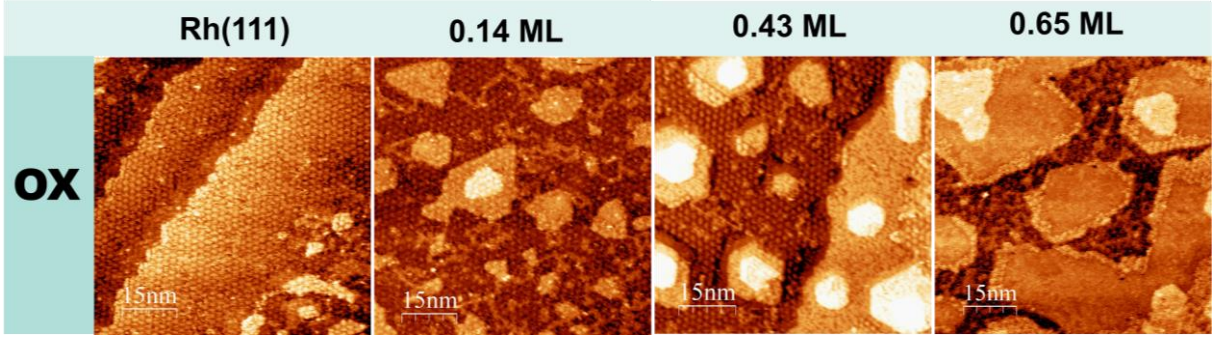


Figure 4.26: STM images showing the evolution of moiré on Rh(111), and 0.14, 0.43 and 0.65 ML Pt/Rh(111). Increased Pt content led to a loss of moiré formed. From covering entire terraces and islands (clean Rh(111) and 0.14 ML), the moiré could only be found between islands and along island edges for the 0.43 ML surface, and only on island edges for the 0.65 ML surface.

By exposing Rh-rich surfaces to low oxygen pressures ($pO_2 = 1 \times 10^{-3}$ mbar) at 700 K, a surface oxide displaying a moire pattern was formed, which was reported to be $RhO_2$ [68]. It was observed that increased Pt content hindered $RhO_2$ growth, which could easily be seen through the loss of moiré pattern. For the clean Rh(111) and 0.14 ML, moiré formed all over the surface, indicating significant enrichment of Rh in the Pt islands for the 0.14 ML surface. For 0.43 and 0.65 ML surface, the amount of moiré was significantely less. Previous literature report that Pt does not oxidize at the pressure and temperature used in this experiment [59, 60], and hence we did not expected $RhO_2$ surface oxide to form on the 2.3 ML surface due to the high Pt content. This was confirmed by the lack of moiré pattern in the STM image and LEED pattern. For all oxidized surfaces it was observed a coverage increase due to formation of Rh ad-islands, as was expected due to the decrease of Rh density in the surface oxide compared to bulk Rh [63]. Presence of moiré along island edges for the 0.43 and 0.65 ML surfaces suggests that the Rh ad-islands formed here.

### 4.3.2 Morphology of Rh and Pt/Rh(111) in 1 bar $O_2$

Previous work has shown that Pt(111) easily oxidizes at 1 bar $O_2$ at 470 K [61, 122]. In order to compare the behavior of Pt and Rh in an oxidizing atmosphere, clean Rh(111) was exposed to 1 bar $O_2$ in the

temperature range RT – 470 K, while performing *in-situ* measurements with a Reactor STM. In order to study the behavior of PtRh alloys, a surface of 0.09 ML Pt on Rh(111) was also studied in 1 bar $O_2$ at RT – 485 K.

For Rh(111) in 1 bar $O_2$ at RT, STM images revealed no formation of surface oxide, nor any clear chemisorbed oxygen structure, although they have been previously reported under these conditions [63]. By increasing the temperature a dotted structure appeared over the entire Rh(111) terraces, and it appeared as though the surfaces became rougher. The dotted structure became more visible at 470 K. To study oxidation of Pt with Rh, 0.09 ML Pt/Rh(111) was exposed to 1 bar $O_2$. The AP surface is described in section 4.1.7. At RT no surface oxide or reconstructions was observed, and the Pt islands remained visible. The surface was kept in 1 bar $O_2$ at RT overnight. The following day the temperature was increased to 370 K, and the islands could still clearly be seen. The surface did not appear dotted nor was there any sign of oxide formation or reconstructions. Temperature was then increased to 435 K, which resulted in more blurry images, but the Pt islands were still visible.

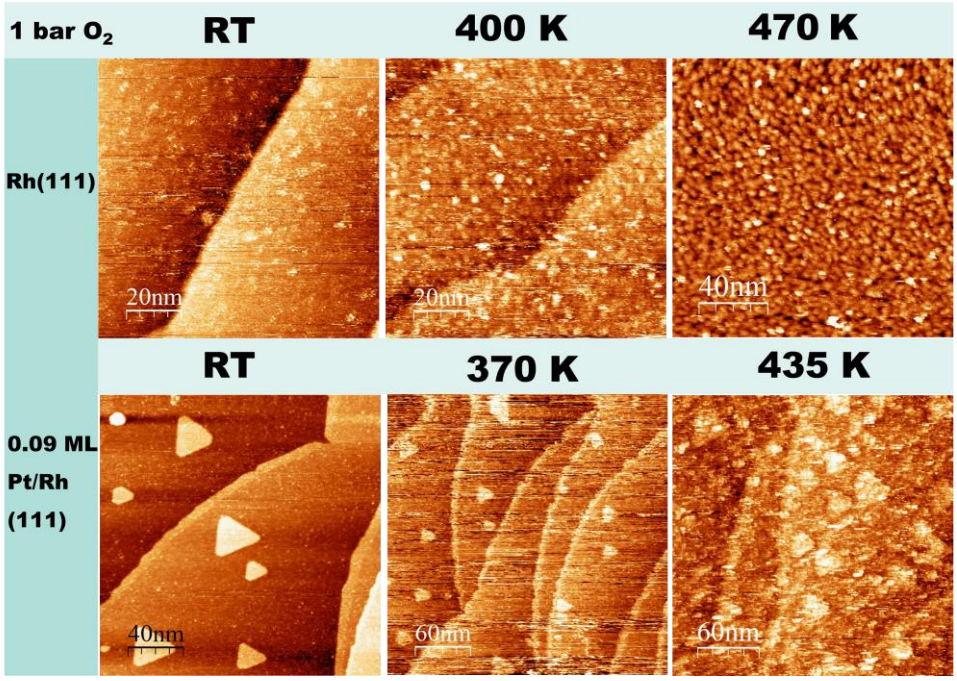


Figure 4.27: STM images showing the evolution of surfaces while increasing temperature, and under exposure of 1 bar $O_2$. Upper panel show clean Rh(111) where a dotted structure becomes more visible upon increasing temperature. Lower panel show 0.09 ML Pt/Rh(111).

Further temperature increase to 485 K did not result in any surface oxide formation on either the Pt islands, nor on the Rh(111) terraces, although Pt is expected to form a surface oxide in these conditions [61]. The surface was kept at 485 K for a certain time, and Figure 4.28 shows the evolution of the surface structure with time. As time passed, it became more difficult to observe the Pt islands on the terraces. It is uncertain whether this is because of loss of tip quality due to high temperature combined with 1 bar $O_2$, or if it is coverage loss due to subsurface diffusion of Pt.

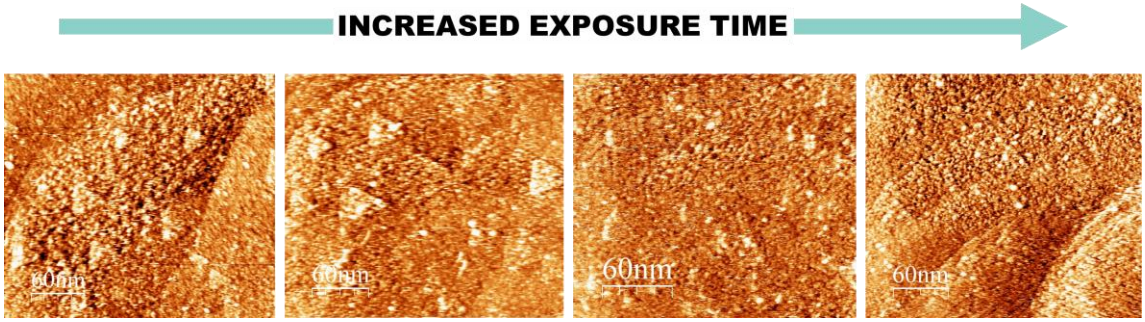


Figure 4.28: STM images showing change with time of Pt deposited on Rh(111) for 5 min at 475 K while being exposed to 1 bar $O_2$ at 485 K.

We observe that at low Pt coverages, Pt/Rh(111) behave similarly as clean Rh(111) in 1 bar $O_2$ and in the temperatures range RT – 485 K. Rh does not oxidize in these conditions, and although Pt is expected to do so, we do not see any surface oxidation formation or restructuring. This may be attributed to substantial Rh enrichment in the Pt islands, or a perturbation of the electronic structures due to interaction between the two metals, which changes the oxidation properties.

## 4.4 Surface Structures of Rh/Pt(111) in Oxygen with Near-Ambient Pressure X-ray Photoelectron Spectroscopy

In order to study the oxidation of PtRh alloys, several surfaces with increased Rh coverage were prepared on Pt(111). Clean Pt(111) and Rh/Pt(111) with coverages of 0.4, 0.5 and 1.2 ML were studied as-prepared and after post-annealing to cover surface composition from Pt-rich to Rh-rich. Near-ambient pressure X-ray photoelectron spectroscopy was used to establish the influence of post-annealing temperature on formation of chemisorbed structures and surface oxides in 1 mbar of $O_2$ at 600 K. Sample preparation and NAP-XPS measurements were performed at the Hippie Beamline at MAX-IV in Lund. Herein we use the abbreviation AP when referring to as-prepared, while XPS measurements performed at near-ambient pressure are denoted as NAP.

### 4.4.1 Rh 3*d* Pt 4*d* for As-Prepared and Post-Annealed Surfaces

Deposition of Rh on Pt(111) was performed at 373 K, and the Rh 3*d* Pt 4*d* spectra were collected at a photon energy of 910 eV. The three prepared surfaces had Rh coverages of 0.4 ML, 0.5 ML and 1.2 ML, as estimated by Ivashenko et al. [72]. Deconvolution of the Rh $3d_{5/2}$ peak for all AP surfaces (Figure 4.29 a)) showed presence of two species; one component at 307.3 eV assigned to bulk Rh, and one component at 306.9 eV assigned to uncoordinated surface atoms [63, 71]. The bulk component at 307.3

eV is attributed to both subsurface Rh, and Rh residing below surface Rh in a multilayered island. All the surfaces had a ratio of bulk Rh to uncoordinated surface atoms of approximately 1:1.

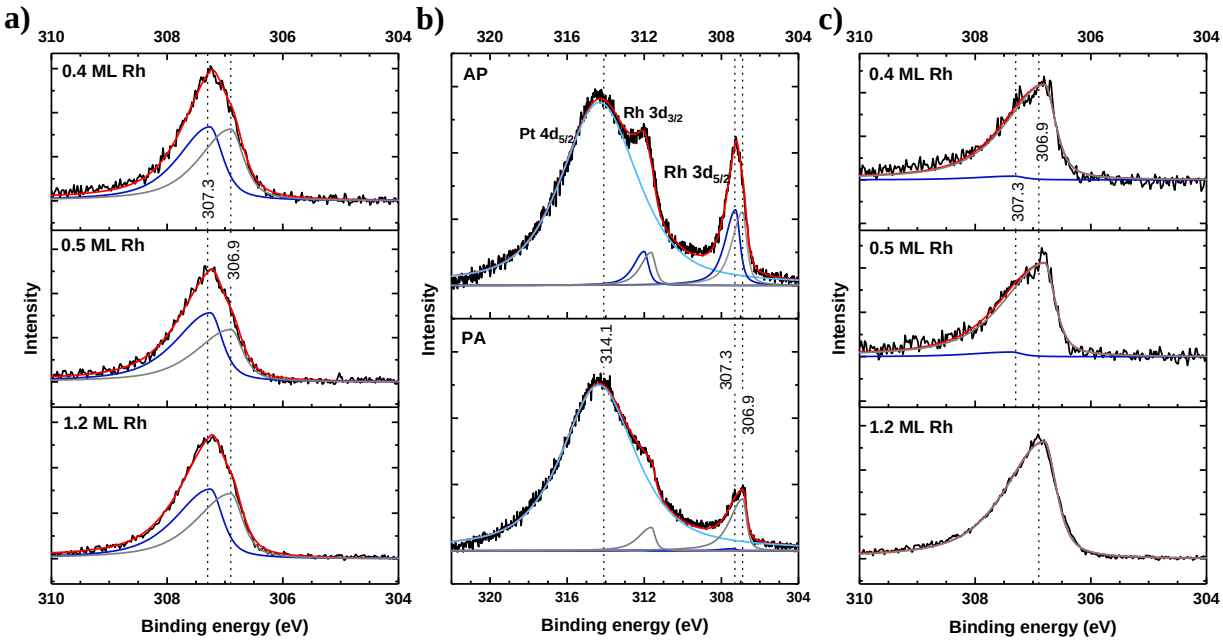


Figure 4.29: a) XP spectra of Rh 3$d_{5/2}$ showing AP Rh/Pt(111) surfaces with presence of both bulk Rh at 307.3 eV and uncoordinated surface atoms at 306.9 eV: 0.4 ML (top), 0.5 ML (middle) and 1.2 ML (bottom). b) Comparison of Rh 3*d* Pt 4*d* XP spectra of 0.4 ML Rh/Pt(111) surface AP (top) and PA (bottom). Rh 3*d* peaks decrease significantly upon PA due to Rh subsurface diffusion and enrichment of Rh islands with Pt. c) Comparsion of Rh 3$d_{5/2}$ XP spectra for all post-annealed Rh/Pt(111) surfaces: 0.4 ML (top), 0.5 ML (middle) and 1.2 ML (bottom). While all Rh films featured mainly surface species at 306.9 eV, a minor bulk component at 307.3 eV was found for 0.4-0.5 ML.

In the roadmap for preparation of Rh/Pt(111) surfaces [37], it was shown that deposition of Rh on Pt(111) at 373 K resulted in 3D growth. This deposition temperature was too low to overcome the interlayer diffusion barrier that prevents 2D growth. This can explain the presence of the bulk component in the XP spectra on both the 0.4 and 0.5 ML surface. Despite their submonolayer coverage, formation of multilayered islands is likely, in which the bulk Rh signal can be attributed to the lower-lying Rh layers. Additionally, small amounts of Rh diffusing subsurface during preparation can also contribute to Rh bulk signal.

PA was performed to promote mixing of Pt and Rh. PA was performed at different temperatures for the three surfaces: 770 K, 700 K and 600 K for the 0.4 ML, 0.5 ML and 1.2 ML surface, respectively. Zheng et al. reported in their Rh/Pt(111) roadmap that post-annealing to 600 K was required to get sufficient Pt and Rh mixing, and subsurface diffusion of Rh became more significant only above 750 K [37]. Hence we expect that upon PA of the 1.2 ML surface to 600 K, only flattening of islands occurs, and not substantial alloying of Pt and Rh. The 0.4 ML and 0.5 ML were exposed to higher annealing

temperatures, and we expect more subsurface diffusion of Rh for these surfaces. Figure 4.29 b) compares AP and PA spectra for 0.4 ML surface, confirming that PA to 770 K resulted in a significant decrease in Rh coverage. The Rh 3*d* peak signal had decreased substantially relative to the Pt 4*d* peak. In particular a twofold decrease was found in the Pt $4d_{5/2}$ to Rh $3d_{5/2}$ peak ratio, dropping from of 6:1 for AP to 13.5:1 for PA. This results was representative for both the 0.4 ML and 0.5 ML surface.

Fit of the Rh $3d_{5/2}$ spectra for the 0.4 ML and 0.5 ML surfaces Pa to 700 – 770 K (upper part of Figure 4.29 c)) showed almost complete loss of bulk Rh (307.3 eV), leaving essentially Rh surface atoms (306.9 eV). Only 4-5% of the Rh $3d_{5/2}$ peak corresponded to bulk Rh for the 0.4 ML and 0.5 ML surface, respectively. The coverages had been reduced from 0.4 ML and 0.5 ML, to 0.18 ML and 0.36 ML, respectively, as determined by Ivashenko et al. [72]. The relatively high annealing temperatures used for the 0.4 ML and 0.5 ML surfaces allowed for substantial Rh subsurface diffusion and Pt enrichement of islands, resulting in Pt-Rh exchange and alloying. In addition, lateral growth and flattening of Rh islands was expected, with a change from multi- to monolayered islands. Still, both surfaces showed presence of bulk Rh in the XP spectra upon PA, which was attributed to subsurface Rh, indicating mixing of Pt and Rh.

Fitting of the Rh $3d_{5/2}$ spectra for the 1.2 ML surface upon PA (lower part of Figure 4.29 c)) showed presence of only surface Rh atoms, and a small coverage loss upon PA to 1.0 ML, as determined by Ivashenko et al. [72]. However, the low annealing temperature (600 K) suggests mostly flattening of islands occurs, and no significant subsurface diffusion of Rh. This is reflected in the absence of bulk signal originating from subsurface Rh.

### 4.4.2 Oxidation of Rh/Pt(111)

Oxidation of the post-annealed surfaces was performed by exposing to 1 mbar $O_2$ at 600 K. *In-situ* O 1*s* spectra were collected at a photon energy of 1130 eV, and are shown in Figure 4.30 a). The O 1*s* spectra of bare Pt(111) (top of Figure 4.30 a)) shows presence of only one component at 529.5 eV, which is attributed to chemisorbed oxygen. This is in accordance with literature, where it is reported that formation of oxide on Pt(111) requires higher oxygen pressures and temperatures [59, 61], or prolonged exposure [60]. In the conditions employed, we expect the chemisorbed (2 × 2)-O structure to form. Pt $4f_{7/2}$ spectra collected at a photon energy of 675 eV (Figure 4.30 b)) confirmed this observation. The spectra of the surface in UHV shows presence of bulk component at 70.9 eV and surface component at 70.6 eV, in accordance with literature [56, 123]. Upon exposure to oxygen, a new component at 71.1 eV is present, attributed to Pt coordinated to chemisorbed oxygen forming the (2 × 2)-O overlayer [56].

The surface containing 0.4 ML Rh featured broadening of the main peak in O 1*s* spectra (second from the top in Figure 4.30 a)), but fitting of the peak indicated presence of only one component at 529.5 eV corresponding to chemisorbed oxygen. Although the oxidation conditions employed here are favoring formation of Rh surface oxide, the absence of peak at 528.9 eV indicated that no surface oxide formed on this surface, which was verified by the Rh 3*d* spectra described later. In the O 1*s* spectra a small peak at around 531.2 eV was present for all surfaces, which Blomberg et al. [69] report as signal from –OH group forming on the surface due to adsorption of H.

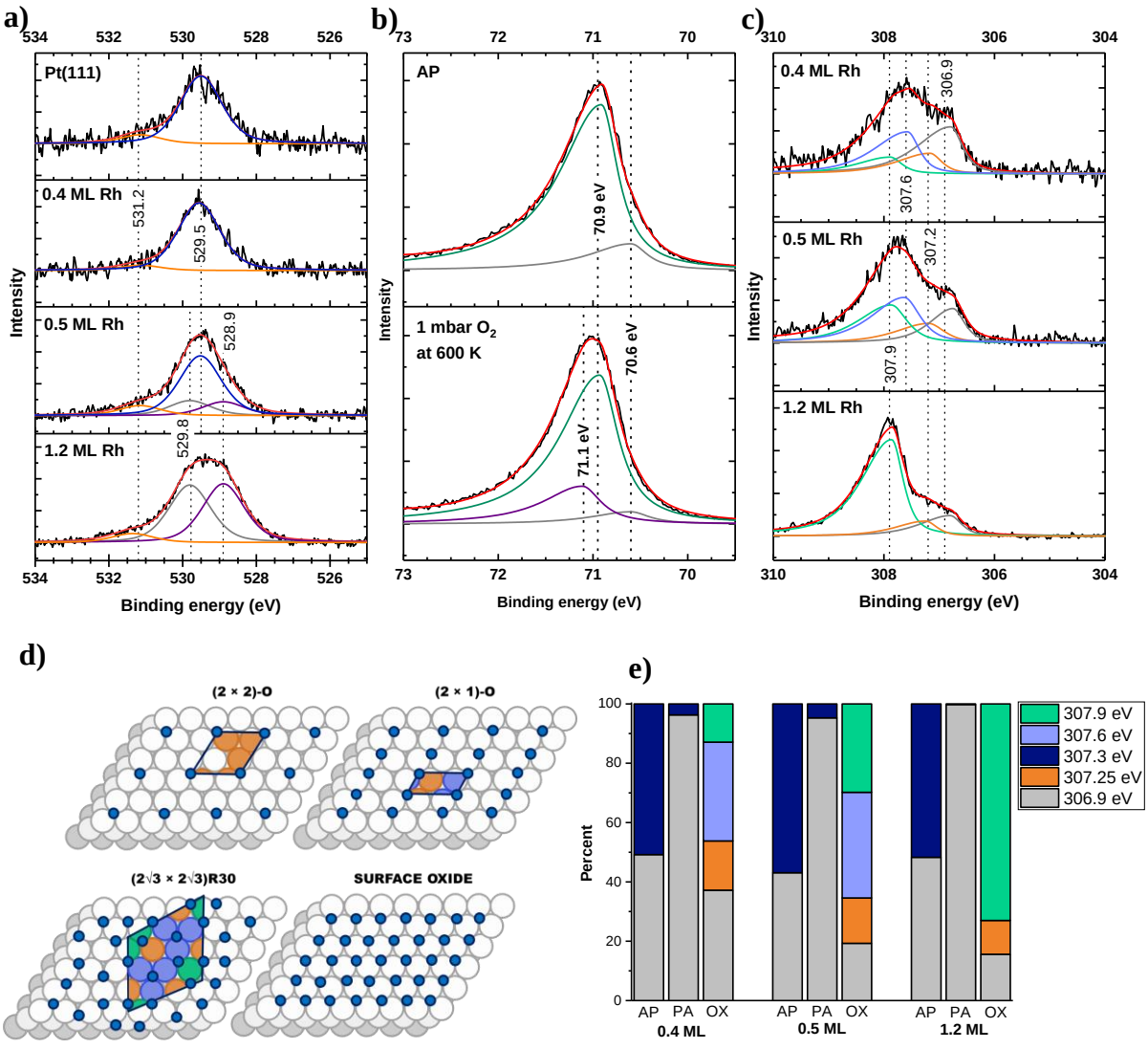


Figure 4.30: **a)** NAP O 1*s* XP spectra of Pt(111) (top), 0.4 ML (2nd), 0.5 ML (3rd) and 1.2 ML (bottom) Rh/Pt(111) exposed to 1 mbar $O_2$ at 600 K. Chemisorbed O at 529.5 eV, is shown in navy color. Purple and grey component at 528.9 eV and 529.8 eV, respectively corresponds to surface and subsurface O of the $RhO_2$ surface oxide. Orange component at 531.2 eV corresponds to –OH group. **b)** Pt $4f_{7/2}$ spectra of clean Pt(111) AP (top) and in 1 mbar $O_2$ at 600 K (bottom). Bulk Pt (70.9 eV) and uncoordinated surface Pt (70.6 eV) are present in the spectra of surface in UHV. Upon exposure to $O_2$, an additional component corresponding to Pt coordinated to chemisorbed oxygen is present at 71.1 eV. **c)** Rh $3d_{5/2}$ spectra of 0.4 ML (top), 0.5 ML (middle) and 1.2 ML (bottom) Rh on Pt(111)

exposed to 1 mbar $O_2$ at 600 K. Grey component at 306.9 eV correspond to surface Rh atoms. Orange component at 307.2 eV corresponds to Rh bound to one O, blue peak at 307.6 eV corresponds to Rh bound to two O, and green peak at 307.9 eV corresponds to Rh bound to three O. **d)** Schematic illustration of chemisorbed oxygen structures (2 × 2), (2 × 1) and (2√3 × 2√3)R30, and surface oxide on Rh(111) surface. Orange Rh atoms are coordinated to one O, purple to two O, and green to 3 O. Ratio for (2x1) is 1:1 for 1O:2O, and for (2√3 × 2√3)R30 is 3:6:3 for 1O:2O:3O. Adapted from [72]. **e)** Distribution of Rh 3*d* components from XP spectra for 0.4, 0.5 and 1.2 ML surface AP, PA and oxidized. It should be noted that the 3O component and surface oxide is located at same binding energy value, hence, both are green, the same applies for 1O and Rh at the interface between metal and surface oxide.

The main peak in the O 1*s* spectra of 0.5 ML Rh (post-annealed to 700 K) was broader than that of 0.4 ML (second from bottom of Figure 4.30 a)). Therefore, the fitting of the spectra required three components. As with the 0.4 ML surface, the largest component corresponded to chemisorbed oxygen. In addition, two new components located at 529.8 eV and 528.9 eV were found, with a separation of approximately 0.9 eV, similar to what has previously been reported as a trilayer surface oxide [68, 69]. The component at 528.9 eV corresponded to the top-most O atoms in the O-Rh-O trilayer, while the component at 529.8 eV originates from to the interlayer O atoms. Estimated peak area suggested that about 32.5% of the oxygen signal was attributed to surface oxide (from both top-most O and interlayer).

For the 1.2 ML surface, the main peak of the O 1*s* spectra (bottom of Figure 4.30 a)) was deconvoluted into two components located at 529.8 eV and 528.9 eV, which both correspond to surface oxide. No presence of chemisorbed species was found, suggesting that the entire surface is covered with the trilayer surface oxide.

The Rh $3d_{5/2}$ spectra were collected at a photon energy of 910 eV provided details of Rh oxidation state for all surfaces (Figure 4.30 c)). For the 0.4 ML surface, the O 1*s* spectra indicated no presence of surface oxide, which was confirmed by deconvolution of the Rh $3d_{5/2}$ peak. Fitting of the spectra showed presence of four components, with the largest component at 306.9 eV, corresponding to uncoordinated Rh surface atoms. Three new components at 307.9 eV, 307.6 eV and 307.2 eV were found during exposure to $O_2$. To help with the assignment of these components, various ordered chemisorbed oxygen ad-layers on the Rh(111) surface were considered (see also section 1.3.7) [62-64, 66, 67]. As illustrated in Figure 4.30 d), Rh can be coordinated to one, two or three oxygen atoms, which are denoted 1O, 2O and 3O, respectively [67]. Difference in coordination number will alter the chemical environment, and hence the binding energy of the Rh atom will differ depending on the coordination. The binding energy for the 3O species is expected around 307.9 eV, and due to absence of surface oxide in O1s spectra, the component found at 307.9 eV in the 0.4 ML surface was assigned to 3O. Further, the only component expected at 307.6 eV is the 2O species. The final peak at 307.2 eV fits the range where we expect both interface Rh and 1O species. From the O 1*s* spectra, no surface oxide was found, and hence the interface

possibility was excluded and the peak was attributed to the O 1*s* species. The three peaks had an O1:O2:O3 ratio of 1:2:0.8. The only structure that has all three components present and has the expected ratio of 1:2:1 is the (2√3 × 2√3)R30 chemisorbed structure. The observed and expected ratios do not match perfectly. A few possibilities can help explaining this mismatch. The (2 × 1) or (2 × 2)-3O structures both contribute with 2O species (1O:2O ratio of 1:1, and 1O:2O:3O ratio of 0:2.5:1, respectively) and were reported to co-exist with the (2√3 × 2√3)R30 structure. Additionally, since the islands of Rh on Pt(111) do not correspond exactely to ideal Rh(111) surface, defects in the (2√3 × 2√3)R30 structure can explain the lower 3O contribution.

From the O 1*s* spectra of the 0.5 ML surface, we expect both surface oxide and chemisorbed structures to form. Fitting of the Rh 3*d* spectra revealed presence of the same four peaks as for the 0.4 ML, but with different ratios. Uncoordinated Rh surface atoms were present at 306.9 eV, as well as the three peaks at 307.9 eV, 307.6 eV and 307.2 eV, with a ratio of 0.9:2:1.7. Upon formation of the (2√3 × 2√3)R30 chemisorbed structure, the peak at 307.9 eV (3O) should have only half the intensity of the peak at 307.6 eV (2O). The mismatch in peak ratio suggests that not all of the signal at 307.9 eV is attributed to 3O. From the O 1*s* spectra it was found that approximately 24% of the oxygen belongs to surface oxide, and the rest is chemisorbed oxygen. Subtracting the contribution from (2√3 × 2√3)R30 structure from the 3O peak area leaves 18% of Rh excess within the 307.9 eV peak. Combined O 1*s* and Rh 3*d* spectra indicate that around 20% of the Rh coverage form the trilayer oxide, and the remaining 80% exhibit a chemisorbed (2√3 × 2√3)R30 structure.

As shown in the O 1*s* spectra, presence of surface oxide, and no chemisorbed oxygen, was suggested on the 1.2 ML surface. This was confirmed by the Rh 3 $d_{5/2}$ spectra, where peak fitting revealed a large component at 307.9 eV, corresponding to Rh from the trilayer oxide structure. Another component was found at 307.2 eV, which can be assigned to interface Rh. For bulk Rh(111), the Rh in the interlayer between the surface oxide and the bulk Rh is expected to have a binding energy of approximately -0.25 eV relative to bulk component [68]. The position of the interface peak found in the 1.2 ML is -0.1 eV from the bulk Rh found in the as-prepared spectra. This can be justified by differences in interface formed at Rh(111) and Rh/Pt(111), where Pt-Rh are alloyed. In addition, a small component corresponding to uncoordinated surface Rh atoms is present. An overview with the different amount of species found for AP, PA and oxidized surface at the corresponding binding energy is included in Figure 4.30 e).

In conclusion, we observe that upon PA of Rh/Pt(111) surfaces, multilayered islands will flatten out, and mixing of Pt and Rh will occur. The impact of PA on alloying is the most pronounced at higher temperatures, where substantial subsurface diffusion of Rh and enrichement of Rh islands with Pt are

accelerated. Consequently, this will hinder growth of a Rh surface oxide, and only chemisorbed structures will form on the highly alloyed Pt-Rh surfaces.

# 5 Discussion

With focus on the experimental results obtained in this work, some few selected topics will be elaborated more in depth. This study and literature show the ways for Pt-Rh surfaces preparation with respect to substrate crystal (Pt/Rh). It was observed that the metal deposited (Rh or Pt), deposition temperature and post-annealing dictate degree of alloying, morphology and growth. I.e., various nanostructured surfaces are obtained, which in turn may affect interaction with reactant gas species (and formation of products) when exposed to reactive gasses. We will compare and correlate our findings for Pt/Rh(111) with the inverse system Rh/Pt(111). We discuss the behavior of Pt-Rh surfaces in various oxygen atmospheres, studied by means of STM and (NAP)-XPS, and show how tuning the Rh and Pt content on the surface alters the oxidation of surfaces. Lastly, we highlight how combining several characterization techniques to study surface structures facilitates making valid conclusions. We also discuss the strength of studying surfaces all the way from UHV to beyond ambient conditions.

## 5.1 Preparation of Pt-Rh Surfaces

As presented in section 4.1.11, one key activity in this MSc project was to provide an overview of routes to prepare various Pt/Rh(1111) surfaces; to create a synthesis-strategy roadmap (Figure 4.16 in section 4.1.11). A corresponding roadmap for the reverse system of Rh/Pt(111) has been reported by our group [37]. In order to summarize and correlate the results obtained in this thesis with those obtained by Zheng et al. [37], the schematics presented in Figure 5.1 is made. Interestingly, it has been observed that the choice of starting crystal, Rh(111) or Pt(111) has an impact on the morphology, growth mode and alloying. The results also indicate that tuning parameters like substrate temperature during Pt/Rh deposition, coverage and PA time and temperature, allows us to easily control the surface characteristics like morphology of islands, island size and step decoration of Pt on Rh(111) and Rh on Pt(111). The key trends observed are that increased deposition temperature leads to more compact, faceted and larger islands, as well as more 2D growth. PA results in coverage loss and flattening of islands. Deposition temperature, as well as PA time and temperature can also alter alloying of Rh and Pt. Literature describes that we should expect different behavior in terms of mixing for Pt/Rh(111) and Rh/Pt(111) [38]. Surface segregation is expected for Pt on Rh(111), while Rh on Pt(111) results in anti-segregation. Further, diffusion of Rh into Pt(111) occurs faster than for Pt into Rh(111) [23]. These differences will have implications on the interaction of surfaces with oxygen, as discussed below.

The main motivation behind the work discussed above is to get a better understanding of nucleation, growth and alloying of Pt-Rh surfaces. Thereafter, this roadmap is provided as a tool for future work where it is beneficial to tune preparation conditions to obtain specific nanostructured surfaces. These

can in turn be used as guideline in the preparation of 2D model catalysts to correlate the dynamics between the catalytic active surface, adsorbed species and the chemical reaction in question. Finally, it should be pointed out that to the best of our knowledge, this is the first study which correlates the preparation and morphology of the two inverse systems; Pt/Rh(111) and Rh/Pt(111).

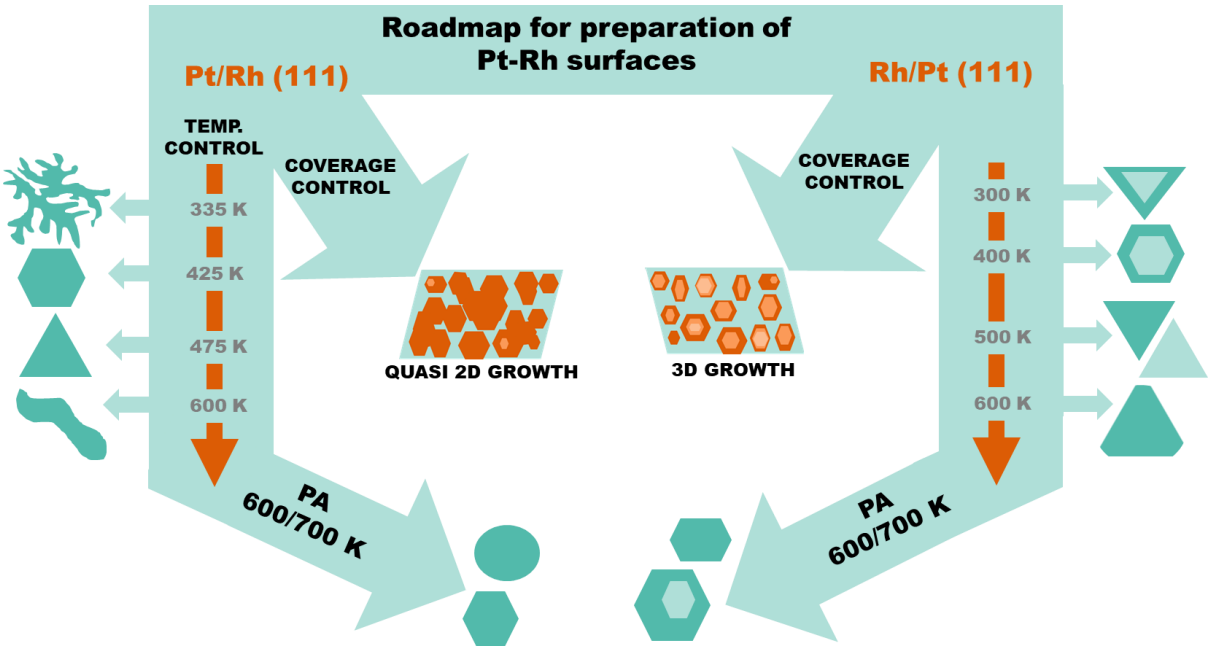


Figure 5.1: Synthesis strategy roadmap for preparation of Pt-Rh surfaces, showing Pt on Rh(111) and Rh on Pt(111). The roadmap illustrates the effect of deposition temperature on morphology, PA, and effect of coverage increase on growth mode and morphology.

***Morphology***

By inspecting Figure 5.1, we see that the as-prepared surfaces of the two systems show significant differences in morphology at low deposition temperatures (RT – 400 K). Pt/Rh(111) forms dendritic and branched islands, similar to Co/Re(0001) [41], and Au/Ru(0001) [42]. For Rh/Pt(111) compact, faceted islands are formed already at low deposition temperatures, similar to Pt/Pt(111) [31], and Ru/Pt(111) [33]. This indicates a difference in diffusion barrier, where Rh has a higher mobility on Pt(111) compared to the reverse system. Increased deposition temperature (425 K and above) led to larger, more compact, faceted islands for both systems. Upon changing deposition temperature, a variety of different islands morphologies were observed, similar to what has been observed for other systems [31, 33, 34, 40-42]. Increased coverage did not alter the islands morphology (see Figure 4.18 in section 4.2), and it was observed that step decoration was more dominating for Pt/Rh(111) compared to Rh/Pt(111). PA induced morphological changes on both systems, where islands coalesced and shape changed to more hexagonal or rounded. Flattening of islands occurred for high coverage surfaces (see Figure 4.18 in section 4.2). It was observed for Pt/Rh(111), PA at a lower temperature (600 K) for a shorter amount of time induced significantly less restructuring than PA at a higher temperature (700 K),

indicating that the PA temperature and time affected the degree of morphological changes. XPS results of Rh/Pt(111) indicated morphological changes upon PA, where substantial loss of the bulk Rh component suggested flattening of islands and presence of only single-layered islands. There is some uncertainty whether the bulk signal actually arises from the lower-lying Rh layers, or if it comes from subsurface Rh.

Another interesting morphological feature that was observed only on Pt/Rh(111) is the lamellar domain structure (section 4.1). It formed on all ~0.2 ML surfaces prepared at deposition temperatures in the range 385 – 600 K (except 500 K), and was retained upon PA, suggesting a high stability. Also on the 2.3 ML surface, it was observed on the lower-lying Pt layers (section 4.2). A possible reason for this restructuring is the discrepancy in height for a single layer of Pt and Rh (0.23 nm and 0.22 nm, respectively [37]). This can cause every other Pt atom row residing on Rh(111) to be slightly shifted upwards due to lack of space, causing this lamellar domain structure. An illustration of the possible model is presented in Figure 5.2. However, this model reminds to be confirmed by computational modelling.

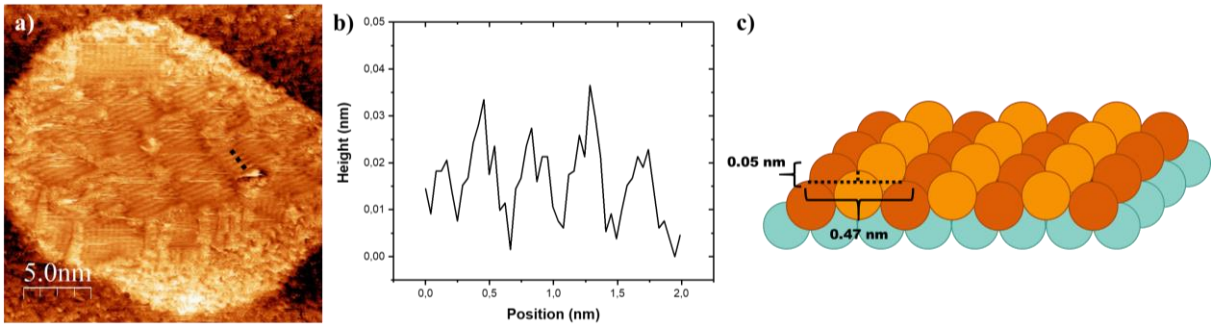


Figure 5.2: a) STM image of lamellar structure on Pt/Rh(111) 600 K. Dotted line corresponds to height profile in b). b) Height profile of lamellar structure. c) Possible model of the lamellar domains where every other Pt row on Rh(111) is slightly shifted upwards due to differences in atomic radius. Turquoise circles illustrate Rh(111) terrace, dark orange corresponds to lower Pt atoms, and light orange to upper Pt atoms. Taking into account the interlayer spacing of Rh of 0.22 nm, 0.23 nm for Pt, the height difference indicated by the vertical line is estimated at 0.05 nm. This matches the height of lamellar structure. The horizontal line shows one period of the structure of 0.47 nm, corresponding quite well to experimental results of ~0.4 nm.

***Growth mode***

Another temperature dependent effect illustrated in Figure 5.1 is the growth mode. For Pt/Rh(111) surfaces, only monolayered islands were observed at low coverage, and upon deposition of 0.65 ML and above (see Figure 4.18 ) multi-layered islands formed, indicating a quasi-2D growth. For Rh/Pt(111) [37], however, already at low coverages multilayered island formed. The 3D growth was retained until around 600 K, where there was a switch to more 2D growth. The change from a quasi-2D growth to a more pure 2D growth at higher temperatures (700 K and above) was also confirmed for Pt/Rh(111) (see Figure 4.21 in section 4.2). This is consistent with a study by Duisberg et al. [44], where Pt/Rh(111)

deposited at 700 K showed a 2D growth mode. This strong temperature-dependent growth mode, where higher temperatures leads to a more 2D growth pattern has been associated with the onset for surface alloy formation [33], and was observed for multiple other metal-on-metal systems including Pt/Pt(111) [31, 34] and Ru/Pt(111) [33, 124]. Notably, for Pt/Pt(111) it has also been observed that higher CO contamination levels led to more 3D growth [36]. Possible influence of gas contaminations on growth mode in the Pt/Rh(111) system should be clarified before a final conclusion is made. XPS results (section 4.4.1) of as-prepared Rh/Pt(111) surfaces show signal from both bulk and surface Rh, indicating multi-layered islands form, with substantial amount of surface Rh, supporting the 3D growth mode previously reported for Rh/Pt(111) [37].

***Alloying***

As previously mentioned, we expect Rh to mix with Pt(111) [38]. This was shown in the Rh/Pt(111) synthesis strategy roadmap [37], where higher deposition temperatures (600 K) and PA resulted in a coverage drop, and at 700 K and above complete subsurface diffusion and alloying with Pt. Our results obtained from XP spectra of PA Rh/Pt(111) surfaces (section 4.4.1) confirm the literature. The Rh/Pt(111) surfaces had undergone coverage losses, revealing subsurface diffusion of Rh and alloying with Pt. The relative coverage loss was greatest for the surface that had been annealed to the highest temperature (770 K), confirming that higher PA temperature led to more subsurface diffusion and alloying of Pt and Rh. In addition, from XPS we observed that the binding energy values for Rh $3d_{5/2}$ were slightly shifted to higher values compared to literature [67-69], which can be a result of alloying with Pt. Multiple other metal-on-metal systems have shown that the alloying process starts to dominate as deposition temperature is increased [31, 33, 41]. For the reverse system (Pt/Rh(111)), literature has reported that segregation is expected [38]. Purely based on STM images of Pt/Rh(111) (section 4.1 and 4.2) it is difficult to conclude whether alloying occurs or not. However, we observe no coverage loss upon PA to 600 K, and some upon PA to 700 K. This indicates some subsurface diffusion of Pt occurs at 700 K, but it is uncertain whether Pt will mix with Rh, or form a segregated phase. This will be elaborated on further in section 5.2 where we discuss oxidation of Pt-Rh surfaces, and use this as a tool for distinguishing between pure Rh and PtRh alloyed areas.

## 5.2 Pt-Rh Surfaces in Oxygen Atmospheres

Another objective of this MSc work was to study the behavior of Pt-Rh surfaces in oxidative atmospheres, and see how tuning Pt and Rh content and alloying altered the oxidation. Key findings are summarized in Figure 5.3. The denominator for all the surfaces is that the requirement for surface oxidation is presence of Rh at the surface. Depending on which system you start with (Pt/Rh(111) or Rh/Pt(111)), there are different ways of manipulating the Rh content on the surface. On the left side of Figure 5.3, i.e. when starting with Pt/Rh(111), increasing the Pt coverage alters surface composition and

prevents oxidation. For the reverse system, Rh/Pt(111) (right side of Figure 5.3), we see that increased PA temperature prevents surface oxidation due to increased alloying.

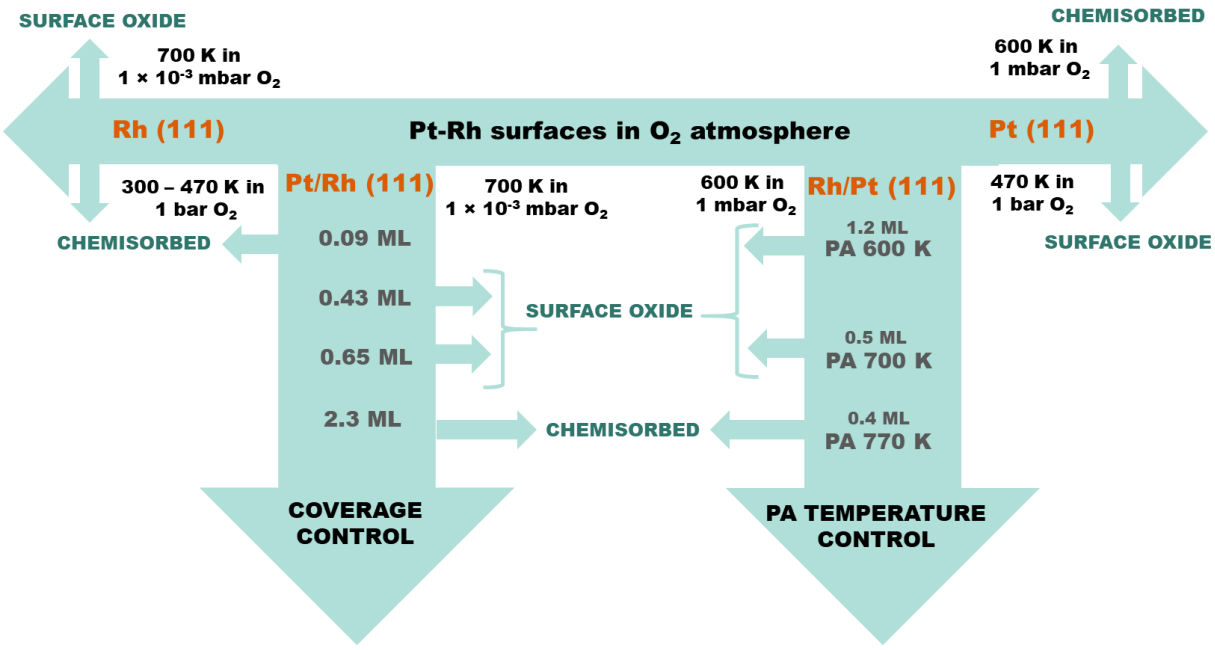


Figure 5.3. Summary of Pt-Rh surfaces in oxygen atmospheres. Temperature and oxygen pressure during oxidation is indicated on the top, and the surface structures labelled indicate the dominating phase. The *left* arrow shows oxidation of clean Rh(111), and the *left down* arrow (Pt/Rh(111)) indicates how controlling Pt coverage alters oxidation. The *right down* arrow (Rh/Pt(111)) shows that controlling PA temperature governs surface structure formed, and the *right* arrow shows oxidation behavior of clean Pt(111).

### 5.2.1 Low Oxygen Pressure ($pO_2 = 1 \times 10^{-3}$ – 1 mbar)

Behavior of the PtRh surfaces in oxygen atmospheres was studied by means of STM and LEED (Pt/Rh(111) surfaces), and by XPS (Rh/Pt(111) surfaces). In agreement with literature [63, 68, 69], growth of an ultra-thin $RhO_2$ surface oxide was achieved on clean Rh(111). This surface oxide displayed a moiré pattern observed in STM images, as well as in LEED. Other late transition metals have also showed growth of a two-dimensional surface oxide [125-127]. Pt is reported to oxidize at higher temperatures and/or pressures compared to Rh [56, 59-61], and we do not expect moiré to form on Pt(111) at the applied conditions. Hence, we used presence of moiré in STM images and LEED to guide our conclusion on oxidation of PtRh alloys.

STM images revealed that increased Pt content resulted in a gradual loss of moiré pattern (see Figure 4.26 in section 4.3.1). Since the surface oxide only grew where there was substantial amounts of Rh, we could use the oxidation procedure to identify where there was Pt enrichment simply by observing where the moiré pattern did not form. Literature has reported that we expect segregation of Pt solute in a Rh host [38]. The composition of the un-oxidized areas could be Pt segregated from Rh(111) forming a

separate layer that passivates the surface from oxidizing, or a Pt enriched PtRh alloy. It is also uncertain if the obtained composition is a result of annealing in UHV, or if the surface composition changes upon oxidation, as has been reported for core-shell Rh@Pt nanoparticles (NPs) [128]. It should be noted that the NPs were 8-11 nm in size, indicating that they are in the nanosize regime in all three dimensions, suggesting a different electronic structure compared to our surfaces, which are considered bulk materials in the *xy*-plane. Still, we should not exclude a possible compositional change upon oxidation for our Pt/Rh(111) surfaces.

For the 0.14 ML surface, moiré formed over the entire surface (Figure 4.26 in section 4.3.1). From what we know of oxidation behavior of Pt, it is highly unlikely that the observed islands mainly consist of Pt. A significant amount of Rh must have replaced Pt so that oxidation became possible. Gustafson et al. [63] reported that upon oxidation of Rh(111) excess Rh from the bulk formed Rh ad-islands, which have the ability to oxidize. This allows us to distinguish between Pt islands and Rh ad-islands. Since the islands on the 0.14 ML surface oxidized, we can conclude that they are predominately Rh ad-islands. On the 0.43 and 0.65 ML surfaces, part of the rim around the islands were oxidized (Figure 5.4), leading to the conclusion that there is Rh enrichment in these areas, and they are most likely due to formation of Rh ad-islands. The interior of the islands did not oxidize, revealing a change in composition. The exact composition of the inner part of the islands is not known, although we can speculate about a high Pt content.

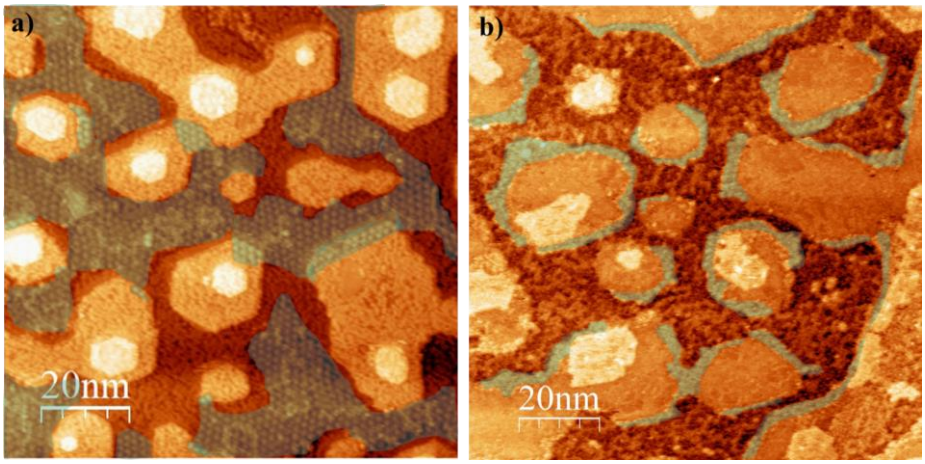


Figure 5.4: Moiré pattern highlighted in STM images of oxidized Pt/Rh(111) surfaces. a) 0.43 ML surface where moiré form on island edges and on Rh(111) terraces. b) 0.65 ML surface where moiré only forms on island rims.

On the Rh(111) terraces surrounding the islands, less moiré formed as Pt coverage increased, seen in Figure 5.4 a) (see Figure 4.26 in section 4.3.1). Around most Pt islands on the 0.43 ML surface there was a border varying from a few nanometers to approximately 10 nm where moiré did not form (Figure 5.4 a)). This suggests that these areas contain an increased amount of Pt, or that alloying of Pt and Rh has occurred, which prevented surface oxide formation. It can also be that Pt dissolved into Rh surfaces

perturbs the electronic properties of the terraces. These results are in agreement with a previous study [44], where it was shown that for Pt deposited on Rh(111) at 700 K, Pt diffuses to step edges, hence we expect more Pt to be found in these areas. Increasing the coverage from 0.43 to 0.65 ML, we observe that moiré no longer forms on the Rh(111) terraces between islands, suggesting there is a transition region is this coverage range. A possible explanation is that above the transition coverage, the Rh(111) terraces are so enriched with Pt that oxidation is prevented. Still, we do observe moiré on the island rims, suggesting that nucleation and growth of Rh oxide is initiated along Pt islands, and if the terraces have sufficiently low Pt content, it continues to grow in these areas. This suggests that the surface energy for Rh around Pt islands is different from the surface energy of Rh in Rh(111) terraces, as a result of a change in chemical environment. It is possible that it is easier for Rh around Pt islands to oxidize since it is part of a nanostructure. It would be useful to reproduce these results to support the theory, which would give information on the growth mechanism of surface oxide. It should be noted that there is a possible discrepancy in oxidation mechanism for Pt/Rh(111) compared to clean Rh(111).

No moiré was observed for the 2.3 ML Pt/Rh(111) surface (Figure 4.24 in section 4.3.1). The surface does not oxidize due to excessive amount of Pt. As previously mentioned, in a core-shell Rh@Pt NP the surface composition undergoes a reversible change upon changing the conditions from oxidizing to reducing [128]. Rh is capable of diffusing through Pt shell and segregates to the surface of the NP in oxidative environments. We observe a different behavior for bulk Rh under a 2.3 ML Pt film, corresponding to a thickness of approximately 0.5 nm. In contrast to the structure of a NP, the Pt film is built up of continuous Pt layers where there might be higher barriers for surface diffusion, or perhaps no diffusion channels like there are in NPs. Even though the thickness of the film might be the same, the NPs are nanostructured in all three dimensions, while the Pt film on Rh(111) is only considered a nanostructure in the *z*-direction, and in the *xy*-plane the film is a bulk structure. In addition, Rh in the NP is regarded a nanostructure, while Rh in the 2.3 ML Pt/Rh(111) system is a single crystal of Rh with bulk properties in all three dimensions. When going from a 0D nanostructure (NP) to a 2D nanostructure (thin film), the electronic structure changes, which suggests a change in chemical properties and different behaviors for the two systems. Another possibility is that Rh is indeed able to diffuse through the Pt film, but the surface is so enriched with Pt that oxidation is prevented.

XPS results obtained by studying oxidation of the reverse system (Rh/Pt(111)) confirmed the STM results (section 4.4.2). As reported in literature [37], and from the XP spectra of as-prepared and post-annealed Rh/Pt(111) surfaces (described in section 4.4.1) it was shown that higher PA temperature leads to increased alloying of Rh with Pt(111). Exposing the surfaces to an oxygen atmosphere revealed that larger amounts of $RhO_2$ surface oxide formed on the surfaces that were annealed to lower temperatures. Hence, PA temperature will determine the alloying of Rh with Pt(111), and increased alloying of Rh with Pt(111) will hinder surface oxide formation. XP spectra of Pt 4*f* showed presence of only

chemisorbed oxygen, and no formation of surface oxide, confirming literature [56, 59-61]. Two of the Rh/Pt(111) surfaces studied had similar coverages, but were annealed to different temperatures around 700 – 775 K. The surface annealed to the highest temperature showed no presence of surface oxide, while the other did. Based on this we can conclude that absence of surface oxide is mainly an effect of PA temperature, not of coverage. We have also observed that even the smallest ad-islands of Rh/Rh(111) can oxidize, which leads to the conclusion that islands size or coverages does not hinder oxidation.

### 5.2.2 High Oxygen Pressure ($pO_2$ = 1 bar)

Clean Rh(111) was exposed to 1 bar $O_2$ at temperatures in the range 300 – 470 K in Reactor STM. No surface oxide, nor any other reconstruction was visible in the STM images (Figure 4.27). From the phase diagram in Figure 1.12 [63], these temperatures are not significantly high to grow a surface oxide. We do, however, expect a chemisorbed oxygen structure to form under these conditions [63]. The absence of reconstructions on the surface might be a result of poor resolution. Obtaining atomically resolved images in the conditions of high pressures (1 bar) and elevated temperatures is a known challenge [1] (p. 7), [129] (p. 205).

Pt(111), however, has been reported to oxidize in 1 bar $O_2$ at around 530 K [61], which reconstructs into a spoked-wheel superstructure. These findings have been reproduced in our lab at 485 K [122]. At lower temperatures, a disordered structure should form [61]. STM images of 0.09 ML Pt/Rh(111) obtained at RT up to 435 K (Figure 4.27), indicated that no disordered structure formed on the Pt islands, nor was any chemisorbed reconstruction seen on the Rh terraces. As temperature increased, STM image quality decreased, which made it harder to see any fine details. Upon increasing the temperature to 485 K, no spoked-wheel reconstruction within the Pt islands was observed. This result indeed confirms our previous findings that combining Rh and Pt alters the oxidation process. From the absence of spoked-wheel structure, we can conclude that presence of Rh is hindering oxidation of Pt. Still, this is somewhat surprising considering that we expect Pt to segregate from Rh(111), and remain at the top of the surface [38]. As previous mentioned, Rh in Rh@Pt NPs will diffuse to the top in oxidative environments to form oxide structure [128]. Although the temperature used in that study was higher than 485 K, it still shows that oxidative environments can alter the composition of a PtRh system. Our previous result (section 4.3.1) shows that upon exposing 0.14 ML Pt/Rh(111) to low $O_2$ pressure at 700 K, surface oxide formed across the entire surface. This indicated that Rh enrichment in Pt islands must have occurred. For the 0.09 ML surface however, temperature was not significantly high to form surface oxide, but the process of Rh enrichment in Pt islands might already have been initiated. By inspecting the STM images of 0.09 ML Pt/Rh(111) it appears as though there is a loss of Pt islands with increased time (Figure 4.28). If this assumption is correct, it suggests that oxidative environments induces Pt subsurface diffusion. However, it is difficult to conclude on this due to insufficient image quality.

## 5.3 Combining Techniques and Using Realistic Conditions

An important aspect of the work presented in this MSc thesis is the strength of combining several techniques to investigate surface structures. Combining techniques like STM, XPS, LEED and DFT allows us to approach what is being investigated from several aspects, which makes it much easier to arrive to the correct conclusions. DFT calculations, though only used via available published data, allows us to view the thermodynamics of the system, while XPS addresses the chemical composition and state. These findings can in turn be verified by means of STM and LEED, which are used for structural characterization. This three-sided approach with computational modeling, compositional characterization and structural characterization, illustrated in Figure 5.5, is needed in order to fully understand the active surface. State-of-the-art work in this field also emphasizes the importance of combining several techniques. We see from Gustafson et al. [63, 68], and Blomberg et al. [69] that DFT, STM, XPS and LEED are combined to support findings. Similarly, in this MSc thesis a similar complementary approach is adopted.

In this MSc thesis, main instrumental tool was STM. For structural characterization of model surfaces STM is a highly suitable technique [130, 131], allowing for atomic scale observation of active sites such as kinks, step edges and defects. STM combines the possibility to obtain electronic and topographical information. However, image interpretation is often not straightforward, which is why many use DFT to simulate the imaging. In this work, STM was used to investigate both morphology and growth by altering conditions such as temperature, coverage, PA time and temperature. In addition, STM allows us to infer about presence of pure metal, alloy, or oxide. In addition, LEED was used to verify surface cleanness and crystallinity, and observe moiré pattern, which implicated formation of surface oxide. XPS complemented these results by giving additional information on the chemical composition of the surface. Although DFT was not used in this thesis, much of the previous work have used it as a tool to support or complement experimental data.

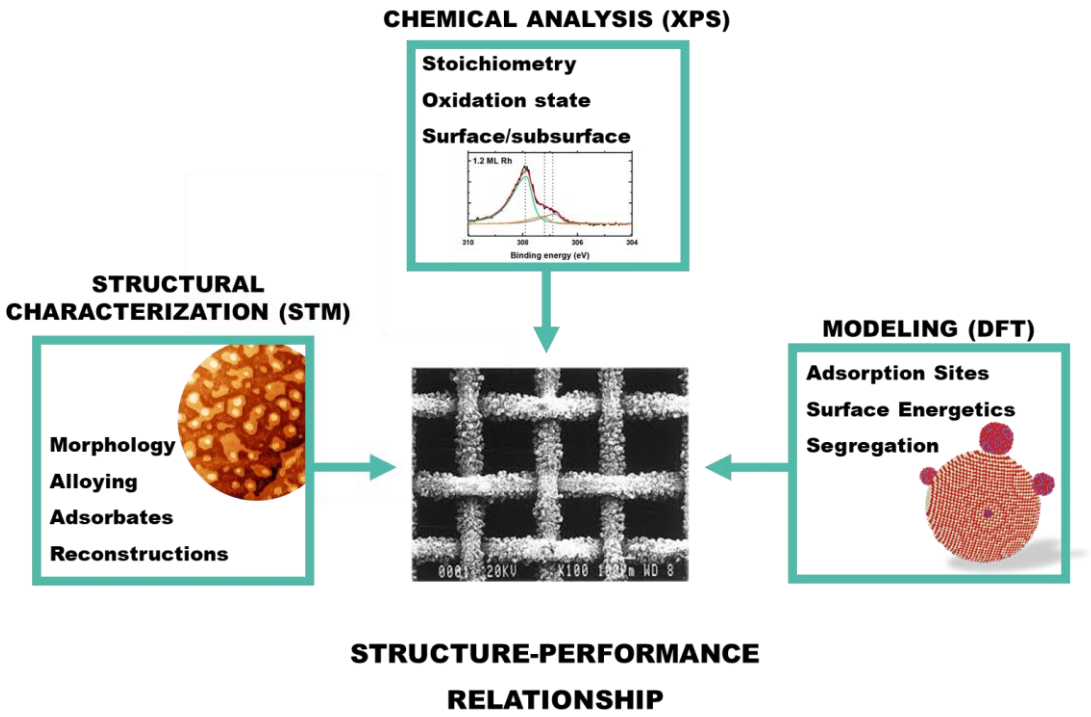


Figure 5.5: Combination of techniques (structural characterization, chemical analysis characterization and computational modeling) provides an excellent pathway to study structure-performance relationship, which can be correlated to real catalysts. Image of Pt-Rh gauze in the center from [21].

Another important aspect when studying surface structures is to minimize the materials- , temperature- and pressure gap (described in 1.1). Major advances have been made over the last decades to allow for study of surfaces under ambient conditions and beyond, as well as studying more complex structures. Multiple studies on Pt(111) and Pt(110) in NO, $O_2$, CO and $H_2$ [61, 132-135] have shown the importance of investigating surfaces in the bar-range (0.2 – 5 bar) by revealing discrepancies of the surface structure when studying them under UHV or at low pressure, compared to near-ambient pressure and beyond. The surfaces that restructure in *in-situ* or *operando* experiments will most likely also restructure in real life. As mentioned, bimetallic Rh@Pt NPs undergo a reversible change in surface composition when switching from oxidizing to reducing conditions [128], highlighting the importance of studying the surface composition of Pt-Rh surfaces in catalytically relevant conditions.

In this work surfaces are explored in the pressure range from $1 \times 10^{-3}$ mbar to 1 bar in STM, and at 1 mbar in XPS, and in temperatures ranging from 300 – 770 K to capture the dynamics of the surfaces structures. The results discussed above show the impact of high temperature and pressure beyond UHV on the resulting surface structures, and illustrate that it is indeed necessary to study surface structures at (near)-ambient pressure conditions to get an accurate understanding of the active surface.

# 6 Conclusions

In order to get a better understanding of the nucleation, growth and alloying processes in the Pt-Rh system, various Pt/Rh(111) surfaces were prepared and studied at UHV by means of STM and LEED. Varying preparation conditions like deposition temperature, coverage, post-annealing temperature and time showed strong influence on the morphology, growth and alloying. With increasing temperature morphology of islands changed from dendritic, to compact triangles and hexagons, to worm-like structures. In addition, it was shown that the growth mode changed with higher deposition temperatures; from a quasi-2D growth to a more pure 2D growth. Post-annealing did not alter the Pt coverage, but the island morphology changed to more rounded shapes. In addition, it was concluded that the various nanostructures could be produced in a reproducible manner following the outlined protocols. For systematic studies, this aspect is of key importance. A summary of the results were presented in a "synthesis strategy roadmap", which was made as a tool to guide preparation of well-defined Pt-Rh nanostructures surfaces.

A complementary synthesis strategy roadmap for the inverse system (Rh/Pt(111)) has been previously developed by our group [37], and therefore the results for the two systems were compared and discussed. In addition, Rh/Pt(111) surfaces with various coverages (0.4 – 1.2 ML) were studied AP and PA by means of XPS to support our previous results [37], and to extend our insight into the properties of Pt-Rh surfaces. XPS confirmed the findings by Zheng et al. [37], stating that PA resulted in increased alloying of Pt and Rh, in which higher PA temperatures lead to more mixing. In addition, XPS results suggested a 3D growth mode, as was shown in the Rh/Pt(111) roadmap [37]. Overall, it was concluded that the choice of starting substrate, Pt(111) or Rh(111), as well as deposition temperature and PA conditions play a major role on the resulting surface in terms of morphology, growth and alloying. The large variety of Pt-Rh surfaces provides a range of distinct Pt-Rh nanostructures to establish structure-performance relationships.

In order to follow the oxidation behavior of Pt-Rh surfaces, various surfaces ranging from clean Rh(111) to clean Pt(111) were studied in oxidative environments utilizing STM, LEED *ex-situ* at UHV, and *in-situ* by Reactor STM and NAP-XPS. Oxidation was studied over a large pressure range, covering six orders of magnitude from $10^{-3}$ to $10^{3}$ mbar. At low $O_2$ pressures ($1 \times 10^{-3}$ mbar) combined with high temperature (700 K), Rh(111) and Rh(111) surfaces with various coverages of Pt were studied by means of STM and LEED. A surface oxide formed on clean Rh(111), as has been reported by Gustafson et al. [68], and by increasing the Pt content on Rh(111), surface oxidation was hindered. For Pt coverages up to approximately 0.5 ML, significant parts of Rh(111) terraces formed a surface oxide. Above this coverage, terrace oxidation was hindered, which is concluded to be a result of Pt enrichment.

*In-situ* measurements in Reactor STM of bare Rh(111) and Pt/Rh(111) at high $O_2$ pressures (1 bar) showed that temperature of 485 K and below are not high enough for the surface oxidation. Although pure Pt is expected to oxidize in these conditions [61], Pt in Pt/Rh(111) did not oxide due to enrichment of Pt islands with Rh with Pt islands, following the trend of bare Rh(111). It was similarly seen in the inverse system (Rh/Pt(111) studied by means of NAP-XPS) that at 1 mbar $O_2$ no surface oxide forms on Pt(111), and enrichment of Pt (due to post-annealing) allows to diminish oxidation of Rh islands.

Overall, it was concluded that the amount of Rh located at the surface is what ultimately governs the oxidation process of Pt-Rh surfaces. However, the ways of controlling the Rh content at the surface are different depending on whether a Pt(111) or a Rh(111) single crystal is used. When starting with a Rh(111) surface, one can simply control the amount of oxide by varying the Pt coverage. When starting with Pt(111), the amount of Rh on the surface can be controlled by adjusting the deposition or post-annealing temperature, as high temperatures favors alloying by Pt diffusion onto the surface.

The current project also demonstrate the importance of using complementary characterization techniques such as XPS (chemical analysis), STM (morphology), LEED (surface structure) and DFT. Combining these techniques with utilizing variable gas pressures to extract fine details is of importance to control surface properties. Although DFT calculations were outside of the scope of the thesis, important relevant literature was used for comparison [67, 68]. The broadened understanding of Pt-Rh surfaces allows us to correlate the structure and catalytic performance, which is of particular interest since important chemical processes such as ammonia oxidation and CO oxidation both rely on Pt-Rh catalysts.

# 7 Perspectives

Our results from preparation of a synthesis strategy roadmap for Pt/Rh(111) (section 4.1), higher coverage Pt/Rh(111) surfaces (section 4.2), and the Rh/Pt(111) roadmap reported by Zheng et al. [37] show the rich variation in surface structures achievable by tuning preparation conditions. In the Pt/Rh(111) roadmap, the effects of deposition temperature and PA on morphology, growth and alloying were mainly explored. In addition, the effect of Pt coverage was explored. Parameters which have not been evaluated systematically are the deposition rate and the PA time. To develop a further understanding of the Pt-Rh system, and to prepare even more well-defined Pt-Rh surfaces, the effects of tuning these parameters should be explored.

When discussing oxidation of Pt/Rh(111) surfaces at low pressures ($pO_2 = 1 \times 10^{-3} - 1$ mbar), it is uncertain whether Pt forms an alloy with Rh, or if Pt is segregated and remains on the surface. We believe it would be fruitful to perform XPS measurements during oxidation of Pt/Rh(111) with various coverages, and with post-annealing to various temperatures. This would allow us to follow compositional changes and get insight into the different oxygen-induced species formed, and the stoichiometry of formed oxides. When studying the oxidized 0.43 and 0.65 ML Pt/Rh(111) surfaces, it was observed as though 0.5 ML is a transition coverage, around which oxidation of Rh(111) terraces changes behavior. To understand the oxidation mechanism for Pt/Rh(111) better, it would be useful to study the oxidation of a series of surfaces with coverages close to 0.5 ML. NAP-XPS measurements for Pt/Rh(111) were indeed planned in March 2020 at MAX-IV, Lund. The measurements will be re-scheduled and completed later.

For comparison of oxidation of thick Pt on Rh(111) and bare Pt(111) (at high pressures $pO_2 = 1$ bar, at 470 K), it would be interesting to study the oxidation process for higher content of Pt on Rh(111), and explore the onset for Pt oxidation by increasing Pt coverage. It would also be useful to study surfaces both AP and PA to view differences in oxidation by altering alloying of Pt and Rh. For 0.09 ML Pt/Rh(111) coverage of Pt dropped with time. It would be useful to explore this further, and investigate if there is an actual coverage loss due to subsurface diffusion of Pt, whether it is reversible or it is a scanning effect.

As highlighted in section 5.3, combining different approaches to understand surface structure makes it easier to draw conclusions. In the work presented in this MSc thesis, no computational modeling was performed. Currently, our group has excellent knowledge when it comes to surface sensitive techniques such as XPS, STM and LEED, and on computational modelling on bulk- and nanomaterials in general. However, we are currently not doing DFT calculations on surfaces, and this would be a natural extension

of our work. DFT modelling is useful to understand the thermodynamics of the system, and is an element that could provide further insight into the behavior of Pt-Rh surfaces. It would allow us to draw conclusions from the experimental results we already have obtained and to predict properties of other bimetallic alloys.

Finally, we use characterization techniques that allow us to study surfaces at ambient conditions and beyond (up to 6 bar and 575 K in the Reactor STM) so that we can study the surfaces at the conditions they are used at in *real life*. Typically, the surfaces are utilized for catalysis. Therefore, the systematic studies on preparation of surfaces and their behavior in oxidizing conditions should be expanded to viewing the surfaces in real chemical processes; e.g. ammonia oxidation at mild conditions for NOx abatement, which is a process studied in the NAFUMA group.

# 8 Appendix

## 8.1 Other Pt/Rh(111) surfaces

Pt was deposited on Rh(111) at 425 K for 30 min followed by PA to 625 K. The surface is shown in Figure 8.1 a)-b). HP measurement was performed with 1 bar $O_2$ while heating to 470 K. As indicated by the STM images in Figure 8.1 c) - h) no clear surface reconstructions or oxide formation could be observed at this pressure and temperature. The most striking change from the STM images collected in UHV is the dotted structure, especially visible in Figure 8.1 d) and e). The dotted structure is also visible inside the vacancy islands.

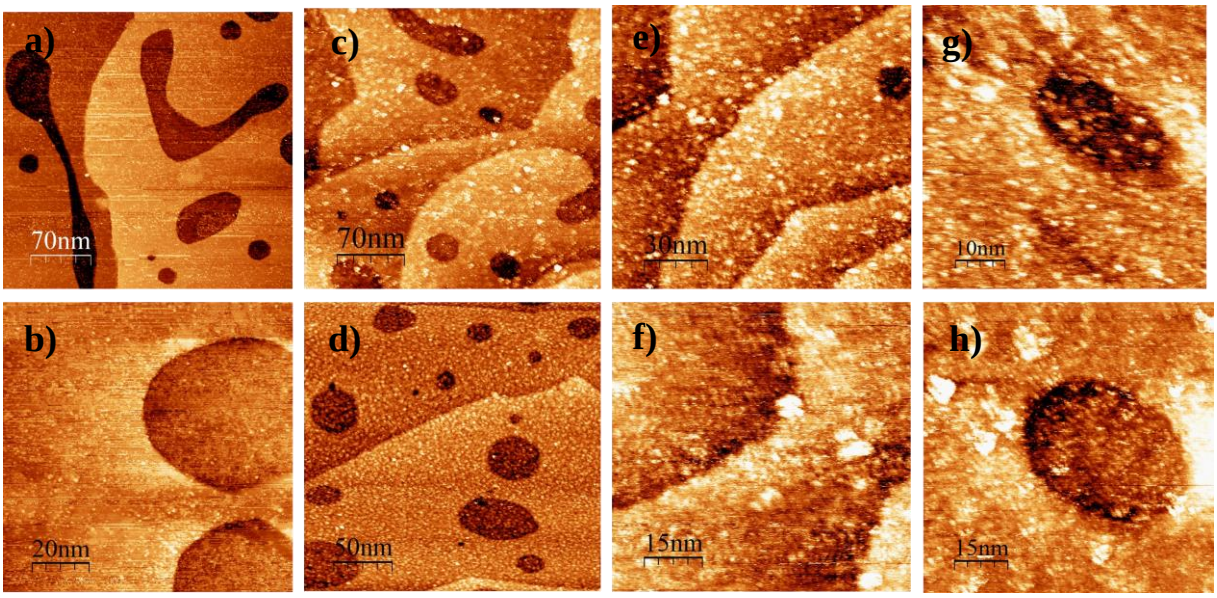


Figure 8.1: Pt deposited on Rh(111) for 30 min at 425K, followed by PA to 625 K in a) - b) UHV. c) – h) 1 bar $O_2$ at 470 K.

Pt was deposited on Rh(111) at RT, first for 80 min, followed by 20 min. The coverage was estimated to be 3 ML, and the resulting STM image of the AP surface can be seen in Figure 8.2 a)-b). The STM images show 3D growth of Pt islands with a branched shape, and the number of layer-steps could be counted to approximately 6, with some variation among the islands. PA was then performed at 625 K for 10 min, and STM images the resulting surface is shown in Figure 8.2 c)-e). PA led to lateral growth of the lower-lying layers and faceting of the upper multilayered islands.

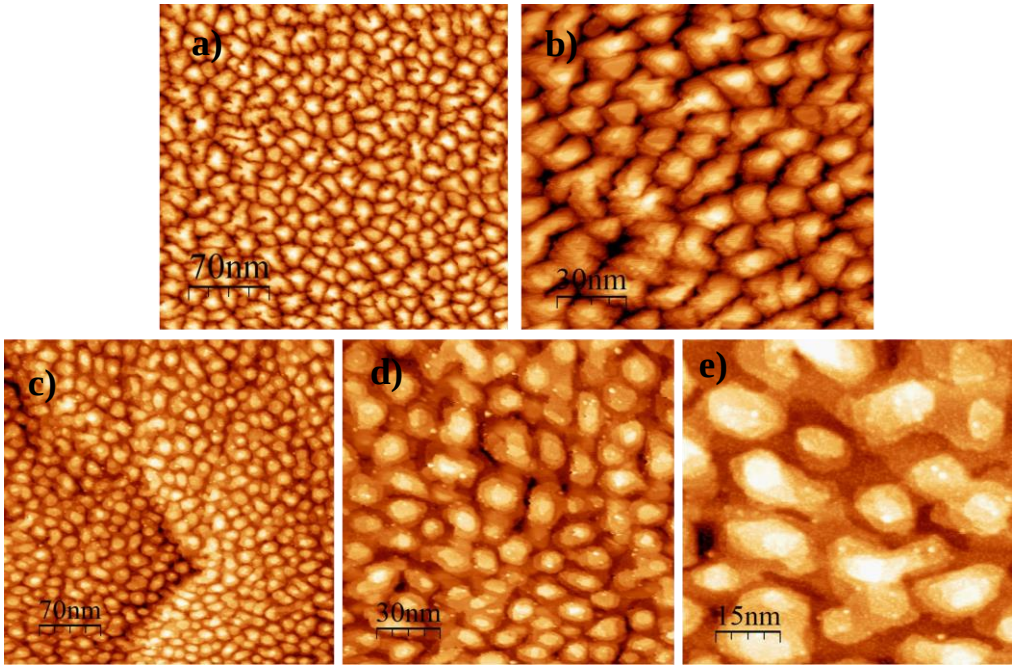


Figure 8.2: a) – b) 3 ML Pt deposited on Rh(111) at RT. c) – e 3 ML Pt deposited on Rh(111) at RT and PA to 625 K.

## 8.2 Rh/Pt(111)

Rh was deposited on Pt(111) at 400 K for 16 min. The surface was then PA to 725 K for 10 min, and can be view in Figure 8.3 a). The surface was exposed to 1 bar of $O_2$ and heated to 470 K simultaneously as scanning was performed. The resulting images (Figure 8.3 b-c)) indicate no major changes upon introducing the surface to oxygen.

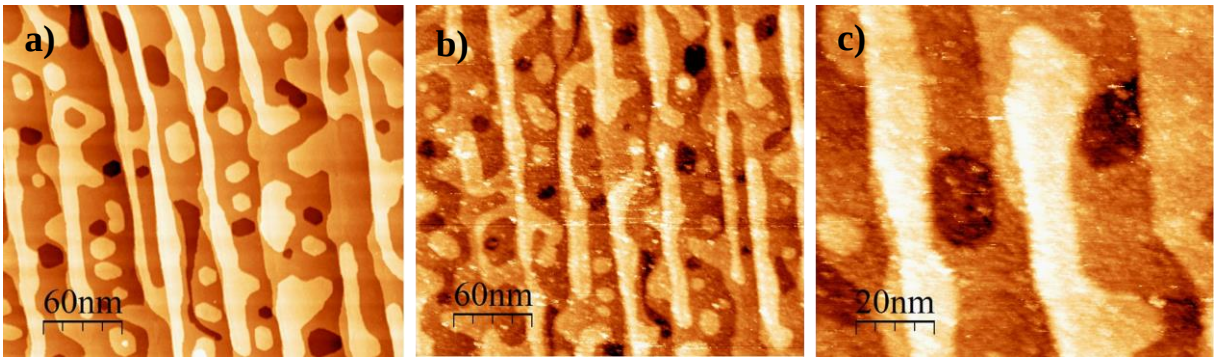


Figure 8.3: Rh/Pt(111) 8nA 16 min 400 K PA 725 K a) in UHV, b) in 1 bar of $O_2$, c) in 1 bar $O_2$ at a smaller scale.

# Literature


1. Frenken, J. and I. Groot, eds. *Operando Research in Heterogeneous Catalysis*. 2017, Springer: Switzerland.
2. Freund, H.J., H. Kuhlenbeck, J. Libuda, G. Rupprechter, M. Bäumer, and H. Hamann, *Bridging the pressure and materials gaps between catalysis and surface science: clean and modified oxide surfaces.* Topics in Catalysis, 2001. **15**(2): p. 201-209.
3. *Current Trends of Surface Science and Catalysis*. 2014: Springer New York.
4. Vang, R.T., E. Lægsgaard, and F. Besenbacher, *Bridging the pressure gap in model systems for heterogeneous catalysis with high-pressure scanning tunneling microscopy*. Physical Chemistry Chemical Physics, 2007. **9**(27): p. 3460-3469.
5. Stampfl, C., A. Soon, S. Piccinin, H. Shi, and H. Zhang, *Bridging the temperature and pressure gaps: Close-packed transition metal surfaces in an oxygen environment.* Journal of Physics Condensed Matter, 2008. **20**: p. 184021.
6. Somorjai, G.A., *Introduction to surface chemistry and catalysis*. 1994, New York: Wiley.
7. Contreras, A.M., X.M. Yan, S. Kwon, J. Bokor, and G.A. Somorjai, *Catalytic CO oxidation reaction studies on lithographically fabricated platinum nanowire arrays with different oxide supports.* Catalysis Letters, 2006. **111**(1): p. 5-13.
8. Mom, R.V., O. Ivashenko, J.W.M. Frenken, I.M.N. Groot, and A.O. Sjåstad, *Nucleation, Alloying, and Stability of Co–Re Bimetallic Nanoparticles on Al2O3/NiAl(110).* The Journal of Physical Chemistry C, 2018. **122**(16): p. 8967-8975.
9. Kuhlenbeck, H., S. Shaikhutdinov, and H.-J. Freund, *Well-Ordered Transition Metal Oxide Layers in Model Catalysis – A Series of Case Studies.* Chemical Reviews, 2013. **113**(6): p. 3986-4034.
10. Grunes, J., J. Zhu, M. Yang, and G.A. Somorjai, *CO Poisoning of Ethylene Hydrogenation over Pt Catalysts: A Comparison of Pt(111) Single Crystal and Pt Nanoparticle Activities.* Catalysis Letters, 2003. **86**(4): p. 157-161.
11. Westerström, R., J.G. Wang, M.D. Ackermann, J. Gustafson, A. Resta, A. Mikkelsen, J.N. Andersen, E. Lundgren, O. Balmes, X. Torrelles, J.W.M. Frenken, and B. Hammer, *Structure and reactivity of a model catalyst alloy under realistic conditions.* Journal of Physics: Condensed Matter, 2008. **20**(18): p. 184018.
12. Somorjai, G.A. and C. Aliaga, *Molecular Studies of Model Surfaces of Metals from Single Crystals to Nanoparticles under Catalytic Reaction Conditions. Evolution from Prenatal and Postmortem Studies of Catalysts.* Langmuir, 2010. **26**(21): p. 16190-16203.
13. Stoltze, P., *Surface science as the basis for the understanding of the catalytic synthesis of ammonia*. Physica Scripta, 1987. **36**(5): p. 824-864.

14. Starr, D.E., Z. Liu, M. Hävecker, A. Knop-Gericke, and H. Bluhm, *Investigation of solid/vapor interfaces using ambient pressure X-ray photoelectron spectroscopy*. Chemical Society Reviews, 2013. **42**(13): p. 5833-5857.
15. Soon, A., S. Piccinin, H. Shi, H. Zhang, and C. Stampfl, *Bridging the temperature and pressure gaps: close-packed transition metal surfaces in an oxygen environment*. 2008: Bristol, UK :. p. 184021.
16. Dong, G., E.B. Fourré, F.C. Tabak, and J.W.M. Frenken, *How Boron Nitride Forms a Regular Nanomesh on Rh(111)*. Physical Review Letters, 2010. **104**(9): p. 096102.
17. *APXPS endstation*. [cited 2020 29.04]; Available from: https://www.maxiv.lu.se/accelerators-beamlines/beamlines/species/species-experimental-station/apxps-endstation/.
18. DeCaluwe, S.C., M.E. Grass, C. Zhang, F.E. Gabaly, H. Bluhm, Z. Liu, G.S. Jackson, A.H. McDaniel, K.F. McCarty, R.L. Farrow, M.A. Linne, Z. Hussain, and B.W. Eichhorn, *In Situ Characterization of Ceria Oxidation States in High-Temperature Electrochemical Cells with Ambient Pressure XPS*. The Journal of Physical Chemistry C, 2010. **114**(46): p. 19853-19861.
19. Chmielarz, L. and M. Jabłońska, *Advances in selective catalytic oxidation of ammonia to dinitrogen: a review*. RSC Advances, 2015. **5**(54): p. 43408-43431.
20. Imbihl, R., A. Scheibe, Y.F. Zeng, S. Günther, R. Kraehnert, V.A. Kondratenko, M. Baerns, W.K. Offermans, A.P.J. Jansen, and R.A. van Santen, *Catalytic ammonia oxidation on platinum: mechanism and catalyst restructuring at high and low pressure.* Physical Chemistry Chemical Physics, 2007. **9**(27): p. 3522-3540.
21. Bergene, E., O. Tronstad, and A. Holmen, *Surface Areas of Pt–Rh Catalyst Gauzes Used for Ammonia Oxidation.* Journal of Catalysis, 1996. **160**(2): p. 141-147.
22. Kalyva, M., D.S. Wragg, H. Fjellvåg, and A.O. Sjåstad, *Engineering Functions into Platinum and Platinum–Rhodium Nanoparticles in a One-Step Microwave Irradiation Synthesis.* ChemistryOpen, 2017. **6**(2): p. 273-281.
23. Kumar, S., D. Waller, H. Fjellvåg, and A.O. Sjåstad, *Development of custom made bimetallic alloy model systems based on platinum – rhodium for heterogeneous catalysis.* Journal of Alloys and Compounds, 2019. **786**: p. 1021-1029.
24. Steiner, C., B. Schönfeld, M.J. Portmann, M. Kompatscher, G. Kostorz, A. Mazuelas, T. Metzger, J. Kohlbrecher, and B. Demé, *Local order in Pt-47 at.% Rh measured with x-ray and neutron scattering.* Physical Review B, 2005. **71**(10): p. 104204.
25. Park, J.Y., Y. Zhang, M. Grass, T. Zhang, and G.A. Somorjai, *Tuning of Catalytic CO Oxidation by Changing Composition of Rh−Pt Bimetallic Nanoparticles.* Nano Letters, 2008. **8**(2): p. 673-677.
26. Bundli, S., P. Dhak, M. Jensen, A.E. Gunnæs, P.D. Nguyen, H. Fjellvåg, and A.O. Sjåstad, *Controlled alloying of Pt-Rh nanoparticles by the polyol approach.* Journal of Alloys and Compounds, 2019. **779**: p. 879-885.

27. *Phase diagram of platinum-rhodium system*, in *Binary Alloy Phase Diagrams plus Updates* 1996, ASM International.
28. Park, J.Y., K. Qadir, and S.M. Kim, *Role of Surface Oxides on Model Nanocatalysts in Catalytic Activity of CO Oxidation*, in *Current Trends of Surface Science and Catalysis*, J.Y. Park, Editor. 2014, Springer New York: New York, NY. p. 145-170.
29. Hendriksen, B.L.M. and J.W.M. Frenken, *CO Oxidation on Pt(110): Scanning Tunneling Microscopy Inside a High-Pressure Flow Reactor*. Physical Review Letters, 2002. **89**(4): p. 046101.
30. Farber, R.G., M.E. Turano, and D.R. Killelea, *Identification of Surface Sites for Low-Temperature Heterogeneously Catalyzed CO Oxidation on Rh(111).* ACS Catalysis, 2018. **8**(12): p. 11483-11490.
31. Bott, M., T. Michely, and G. Comsa, *The homoepitaxial growth of Pt on Pt(111) studied with STM.* Surface Science, 1992. **272**(1): p. 161-166.
32. Michely, T. and G. Comsa, *Temperature dependence of the sputtering morphology of Pt(111).* Surface Science, 1991. **256**(3): p. 217-226.
33. Berkó, A., A. Bergbreiter, H.E. Hoster, and R.J. Behm, *From bilayer to monolayer growth: Temperature effects in the growth of Ru on Pt(111).* Surface Science, 2009. **603**(16): p. 2556-2563.
34. Michely, T., M. Hohage, M. Bott, and G. Comsa, *Inversion of growth speed anisotropy in two dimensions.* Phys Rev Lett, 1993. **70**(25): p. 3943-3946.
35. Jacobsen, J., K.W. Jacobsen, and P. Stoltze, *Nucleation of the Pt(111) reconstruction: a simulation study.* Surface Science, 1994. **317**(1): p. 8-14.
36. Kalff, M., G. Comsa, and T. Michely, *How Sensitive is Epitaxial Growth to Adsorbates?* Physical Review Letters, 1998. **81**(6): p. 1255-1258.
37. Zheng, J., O. Ivashenko, H. Fjellvåg, I.M.N. Groot, and A.O. Sjåstad, *Roadmap for Modeling RhPt/Pt(111) Catalytic Surfaces.* The Journal of Physical Chemistry C, 2018. **122**(46): p. 26430-26437.
38. Ruban, A.V., H.L. Skriver, and J.K. Nørskov, *Surface segregation energies in transition-metal alloys.* Physical Review B, 1999. **59**(24): p. 15990-16000.
39. Attard, G.A., R. Price, and A. Al-Akl, *Electrochemical and ultra-high vacuum characterisation of rhodium on Pt(111): a temperature dependent growth mode.* Surface Science, 1995. **335**: p. 52-62.
40. Tsui, F., J. Wellman, C. Uher, and R. Clarke, *Morphology transition and layer-by-layer growth of Rh(111).* Phys Rev Lett, 1996. **76**(17): p. 3164-3167.
41. Parschau, M. and K. Christmann, *Cobalt on rhenium(0001) – an example of thermally activated layer intermixing and surface alloying.* Surface Science, 1999. **423**(2): p. 303-323.

42. Hwang, R.Q., J. Schröder, C. Günther, and R.J. Behm, *Fractal growth of two-dimensional islands: Au on Ru(0001).* Physical Review Letters, 1991. **67**(23): p. 3279-3282.
43. Máca, F., M. Kotrla, and O.S. Trushin, *Energy barriers for diffusion on stepped Rh(111) surfaces.* Surface Science, 2000. **454-456**: p. 579-583.
44. Duisberg, M., M. Dräger, K. Wandelt, E.L.D. Gruber, M. Schmid, and P. Varga, *High temperature growth of Pt on the Rh(111) surface.* Surface Science, 1999. **433-435**: p. 554-558.
45. Gland, J.L., B.A. Sexton, and G.B. Fisher, *Oxygen interactions with the Pt(111) surface.* Surface Science, 1980. **95**(2): p. 587-602.
46. Joebstl, J.A., *On the chemisorption of oxygen on platinum (111) surfaces.* Journal of Vacuum Science and Technology, 1975. **12**(1): p. 347-351.
47. Gland, J.L. and V.N. Korchak, *The adsorption of oxygen on a stepped platinum single crystal surface.* Surface Science, 1978. **75**(4): p. 733-750.
48. Materer, N., U. Starke, A. Barbieri, R. Döll, K. Heinz, M.A. Van Hove, and G.A. Somorjai, *Reliability of detailed LEED structural analyses: Pt(111) and Pt(111)-p(2×2)-O.* Surface Science, 1995. **325**(3): p. 207-222.
49. Derry, G.N. and P.N. Ross, *High coverage states of oxygen adsorbed on Pt(100) and Pt(111) surfaces.* Surface Science, 1984. **140**(1): p. 165-180.
50. Parkinson, C.R., M. Walker, and C.F. McConville, *Reaction of atomic oxygen with a Pt(111) surface: chemical and structural determination using XPS, CAICISS and LEED.* Surface Science, 2003. **545**(1): p. 19-33.
51. Weaver, J.F., J.-J. Chen, and A.L. Gerrard, *Oxidation of Pt(111) by gas-phase oxygen atoms.* Surface Science, 2005. **592**(1): p. 83-103.
52. Saliba, N.A., Y.L. Tsai, C. Panja, and B.E. Koel, *Oxidation of Pt(111) by ozone (O3) under UHV conditions.* Surface Science, 1999. **419**(2): p. 79-88.
53. Parker, D.H., M.E. Bartram, and B.E. Koel, *Study of high coverages of atomic oxygen on the Pt(111) surface.* Surface Science, 1989. **217**(3): p. 489-510.
54. Bartram, M.E., R.G. Windham, and B.E. Koel, *The molecular adsorption of nitrogen dioxide on Pt(111) studied by temperature programmed desorption and vibrational spectroscopy.* Surface Science, 1987. **184**(1): p. 57-74.
55. Devarajan, S.P., J.A. Hinojosa, and J.F. Weaver, *STM study of high-coverage structures of atomic oxygen on Pt(111): p(2×1) and Pt oxide chain structures.* Surface Science, 2008. **602**(19): p. 3116-3124.
56. Miller, D.J., H. Öberg, S. Kaya, H. Sanchez Casalongue, D. Friebel, T. Anniyev, H. Ogasawara, H. Bluhm, L.G.M. Pettersson, and A. Nilsson, *Oxidation of Pt(111) under Near-Ambient Conditions.* Physical Review Letters, 2011. **107**(19): p. 195502.

57. Krasnikov, S.A., S. Murphy, N. Berdunov, A.P. McCoy, K. Radican, and I.V. Shvets, *Self-limited growth of triangular PtO2nanoclusters on the Pt(111) surface.* Nanotechnology, 2010. **21**(33): p. 335301.
58. Ellinger, C., A. Stierle, I. Robinson, A. Nefedov, and H. Dosch, *Atmospheric pressure oxidation of Pt(111).* Journal of Physics: Condensed Matter, 2008. **20**: p. 184013.
59. Ivashenko, O., *Personal Communication* 2020.
60. Fantauzzi, D., S. Calderon, J. Mueller, M. Grabau, C. Papp, H.-P. Steinrück, T. Senftle, A. van Duin, and T. Jacob, *Growth of Stable Surface Oxides on Pt(111) at Near-Ambient Pressures.* Angewandte Chemie International Edition, 2017. **56**.
61. van Spronsen, M.A., J.W.M. Frenken, and I.M.N. Groot, *Observing the oxidation of platinum.* Nature Communications, 2017. **8**(1): p. 429.
62. Schwegmann, S., H. Over, V. De Renzi, and G. Ertl, *The atomic geometry of the O and CO + O phases on Rh(111).* Surface Science, 1997. **375**(1): p. 91-106.
63. Gustafson, J., *Oxidation of some Late Transition Metal Surfaces: Structural Studies from UHV to Atmospheric Pressure*, in *Department of Synchrotron Radiation Research*. 2006, Lund University: Lund.
64. Wong, P.C., K.C. Hui, M.Y. Zhou, and K.A.R. Mitchell, *LEED investigations of the Rh(111)-(2×2)-O surface structure: measurements with a video analyser in the presence of some electron beam disordering of the adsorbed layer.* Surface Science Letters, 1986. **165**(1): p. L21-L25.
65. Marchini, S., C. Sachs, and J. Wintterlin, *STM investigation of the (2×2)O and (2×1)O structures on Rh(111).* Surface Science, 2005. **592**(1): p. 58-64.
66. Reimann, C.T., M. El‐Maazawi, K. Walzl, B.J. Garrison, N. Winograd, and D.M. Deaven, *Rh atom ejection from keV ion‐bombarded p(2×2)O/Rh{111}: Adsorption site and coverage determination from angle‐resolved desorption measurements.* The Journal of Chemical Physics, 1989. **90**(3): p. 2027-2034.
67. Köhler, L., G. Kresse, M. Schmid, E. Lundgren, J. Gustafson, A. Mikkelsen, M. Borg, J. Yuhara, J.N. Andersen, M. Marsman, and P. Varga, *High-Coverage Oxygen Structures on Rh(111): Adsorbate Repulsion and Site Preference Is Not Enough.* Physical Review Letters, 2004. **93**(26): p. 266103.
68. Gustafson, J., A. Mikkelsen, M. Borg, E. Lundgren, L. Köhler, G. Kresse, M. Schmid, P. Varga, J. Yuhara, X. Torrelles, C. Quirós, and J.N. Andersen, *Self-Limited Growth of a Thin Oxide Layer on Rh(111).* Physical Review Letters, 2004. **92**(12): p. 126102.

69. Blomberg, S., E. Lundgren, R. Westerström, E. Erdogan, N.M. Martin, A. Mikkelsen, J.N. Andersen, F. Mittendorfer, and J. Gustafson, *Structure of the Rh2O3(0001) surface.* Surface Science, 2012. **606**(17): p. 1416-1421.
70. Farber, R.G., M.E. Turano, E.C.N. Oskorep, N.T. Wands, E.V. Iski, and D.R. Killelea, *The Quest for Stability: Structural Dependence of Rh(111) on Oxygen Coverage at Elevated Temperature.* The Journal of Physical Chemistry C, 2017. **121**(19): p. 10470-10475.
71. Toyoshima, R., M. Yoshida, Y. Monya, K. Suzuki, K. Amemiya, K. Mase, B.S. Mun, and H. Kondoh, *High-Pressure NO-Induced Mixed Phase on Rh(111): Chemically Driven Replacement.* The Journal of Physical Chemistry C, 2015. **119**(6): p. 3033-3039.
72. Ivashenko, O., N. Johanson, C. Pettersen, M. Jensen, J. Zheng, J. Schnadt, and A.O. Sjåstad, *How surface species drive product distribution during ammonia oxidation, STM and AP-XPS study.* . 2020, University of Oslo: Oslo.
73. Kittel, C. and P. McEuen, *Introduction to solid state physics*. 8th ed. ed. 2005, Hoboken, N.J: Wiley.
74. Tilley, R.J.D., *Understanding solids : the science of materials*. 2nd ed. ed. 2013, Chichester: Wiley.
75. Lundgren, E., M. Schmid, G. Leonardelli, A. Hammerschmid, B. Stanka, and P. Varga, *On the Role of Kinks and Strain in Heteroepitaxial Growth: An STM Study.* Surface Review and Letters, 2000. **07**(05n06): p. 673-677.
76. Hudson, J.B., *Surface science : an introduction*. 1992, Boston: Butterworth-Heinemann.
77. Kolasinski, K.W., *Experimental Probes and Techniques*, in *Surface Science*. 2012. p. 51-114.
78. Woodruff, D.P., *Adsorption and reaction at stepped surfaces: a historical viewpoint.* Journal of Physics: Condensed Matter, 2016. **28**(49): p. 491001.
79. Smoluchowski, R., *Anisotropy of the Electronic Work Function of Metals.* Physical Review, 1941. **60**(9): p. 661-674.
80. Barber, Z.H., *The Structure of Vapor-Deposited Materials*, in *Reference Module in Materials Science and Materials Engineering*. 2016, Elsevier.
81. Masel, R.I., *Principles of adsorption and reaction on solid surfaces*. 1996: New York (N.Y.) : Wiley.
82. Ascheron, C.E., W. Skolaut, R. Behrisch, and W. Eckstein, *Sputtering by Particle Bombardment: Experiments and Computer Calculations from Threshold to MeV Energies*. Topics in Applied Physics. Vol. 110. 2007, Berlin, Heidelberg: Berlin, Heidelberg: Springer Berlin Heidelberg.
83. Smallman, R.E., *Modern physical metallurgy*, A.H.W. Ngan, Editor. 2014, Butterworth-Heinemann: Oxford, UK.

84. Ferrari, P., S. Rojas, D.E. Diaz-Droguett, and A.L. Cabrera, *Evaporation of Low-Vapor Pressure Metals Using a Conventional Mini Electron Beam Evaporator*. Instrumentation Science & Technology, 2014. **42**(2): p. 142-152.
85. Mattox, D.M., *Chapter 6 - Vacuum Evaporation and Vacuum Deposition*, in *Handbook of Physical Vapor Deposition (PVD) Processing (Second Edition)*, D.M. Mattox, Editor. 2010, William Andrew Publishing: Boston. p. 195-235.
86. Binnig, G., H. Rohrer, C. Gerber, and E. Weibel, *Surface Studies by Scanning Tunneling Microscopy*. Physical Review Letters, 1982. **49**(1): p. 57-61.
87. Nobel Media AB 2020. *Press release: The Nobel Prize in Physics 1986*. 2020 [cited 2020 24 Feb]; Available from: https://www.nobelprize.org/prizes/physics/1986/press-release/.
88. Birdi, K., *Scanning Probe Microscopes*. 2003, Boca Raton: CRC Press.
89. Leng, Y., *Material Characterization, Introduction to Microscopic and Spectroscopic Methods*. Second Edition ed. 2013, Hong Kong.
90. Chaika, A.N., *High Resolution STM Imaging*, in *Surface Science Tools for Nanomaterials Characterization*, C.S.S.R. Kumar, Editor. 2015, Springer Berlin Heidelberg: Berlin, Heidelberg. p. 561-619.
91. Tomitori, M., *Scanning Tunneling Microscopy*, in *Roadmap of Scanning Probe Microscopy*, S. Morita, Editor. 2007, Springer Berlin Heidelberg: Berlin, Heidelberg. p. 7-14.
92. Grzela, T., *Comparative STM-based study of thermal evolution of Co and Ni germanide nanostructures on Ge(001)*. 2015.
93. Voigtländer, B., *Scanning Tunneling Microscopy*, in *Scanning Probe Microscopy: Atomic Force Microscopy and Scanning Tunneling Microscopy*, B. Voigtländer, Editor. 2015, Springer Berlin Heidelberg: Berlin, Heidelberg. p. 279-308.
94. Schitter, G. and M.J. Rost, *Scanning probe microscopy at video-rate*. Materials Today, 2008. **11**: p. 40-48.
95. Stroscio, J.A., R.M. Feenstra, and A.P. Fein, *Local state density and long-range screening of adsorbed oxygen atoms on the GaAs(110) surface*. Physical Review Letters, 1987. **58**(16): p. 1668-1671.
96. Hoogeman, M.S., D.G.v. Loon, R.W.M. Loos, H.G. Ficke, E.d. Haas, J.J.v.d. Linden, H. Zeijlemaker, L. Kuipers, M.F. Chang, M.A.J. Klik, and J.W.M. Frenken, *Design and performance of a programmable-temperature scanning tunneling microscope*. Review of Scientific Instruments, 1998. **69**(5): p. 2072-2080.
97. Dong, G., G.J.C.v. Baarle, and J.W.M. Frenken, *Graphene Formation on Metal Surfaces Investigated by In-situ STM*, in *Advances in Graphene Science*
A. Mahmood, Editor. 2013, InTechOpen.

98. Kuipers, L., R.W.M. Loos, H. Neerings, J.t. Horst, G.J. Ruwiel, A.P.d. Jongh, and J.W.M. Frenken, *Design and performance of a high‐temperature, high‐speed scanning tunneling microscope.* Review of Scientific Instruments, 1995. **66**(9): p. 4557-4565.
99. McIntyre, B.J., M.B. Salmeron, and G.A. Somorjai, *A scanning tunneling microscope that operates at high pressures and high temperatures (430 K) and during catalytic reactions.* Catalysis Letters, 1992. **14**(3): p. 263-269.
100. Laegsgaard, E., L. Österlund, P. Thostrup, P.B. Rasmussen, I. Stensgaard, and F. Besenbacher, *A high-pressure scanning tunneling microscope.* Review of Scientific Instruments, 2001. **72**(9): p. 3537-3542.
101. Rößler, M., P. Geng, and J. Wintterlin, *A high-pressure scanning tunneling microscope for studying heterogeneous catalysis.* Review of Scientific Instruments, 2005. **76**(2): p. 023705.
102. Kolmakov, A. and D.W. Goodman, *In situ scanning tunneling microscopy of individual supported metal clusters at reactive gas pressures from 10−8 to 104Pa.* Review of Scientific Instruments, 2003. **74**(4): p. 2444-2450.
103. Rasmussen, P.B., B.L.M. Hendriksen, H. Zeijlemaker, H.G. Ficke, and J.W.M. Frenken, *The "reactor STM": A scanning tunneling microscope for investigation of catalytic surfaces at semi-industrial reaction conditions.* Review of Scientific Instruments, 1998. **69**(11): p. 3879-3884.
104. Herbschleb, C.T., P.C.v.d. Tuijn, S.B. Roobol, V. Navarro, J.W. Bakker, Q. Liu, D. Stoltz, M.E. Cañas-Ventura, G. Verdoes, M.A.v. Spronsen, M. Bergman, L. Crama, I. Taminiau, A. Ofitserov, G.J.C.v. Baarle, and J.W.M. Frenken, *The ReactorSTM: Atomically resolved scanning tunneling microscopy under high-pressure, high-temperature catalytic reaction conditions.* Review of Scientific Instruments, 2014. **85**(8): p. 083703.
105. LPM, *ReactorSTM system Quick Start Guide*. 2016, Leiden Probe Microscopy.
106. Fahlman, A., C. Nordling, and K. Siegbahn, *ESCA : atomic, molecular and solid state structure studied by means of electron spectroscopy*. 1967: Uppsala : Almqvist and Wiksell.
107. Einstein, A., *Über einen die Erzeugung und Verwandlung des Lichtes betreffenden heuristischen Gesichtspunkt.* Annalen der Physik, 1905. **322**(6): p. 132-148.
108. Haasch, R.T., *X-Ray Photoelectron Spectroscopy (XPS) and Auger Electron Spectroscopy (AES)*, in *Practical Materials Characterization*, M. Sardela, Editor. 2014, Springer New York: New York, NY. p. 93-132.
109. Van der Heide, P., *X-ray photoelectron spectroscopy : an introduction to principles and practices*. 2012, Wiley: Hoboken, New Jersey.
110. Siegbahn, H. and K. Siegbahn, *ESCA applied to liquids.* Journal of Electron Spectroscopy and Related Phenomena, 1973. **2**(3): p. 319-325.

111. Zhong, L., D. Chen, and S. Zafeiratos, *A mini review of in situ near-ambient pressure XPS studies on non-noble, late transition metal catalysts.* Catalysis Science & Technology, 2019. **9**(15): p. 3851-3867.
112. Davisson, C. and L.H. Germer, *Diffraction of Electrons by a Crystal of Nickel*. Physical Review, 1927. **30**(6): p. 705-740.
113. Clarke, L.J., *Surface crystallography : an introduction to low energy electron diffraction*. 1985, Chichester: Wiley.
114. Horio, Y., *Low-Energy Electron Diffraction*, in *Compendium of Surface and Interface Analysis*, J. The Surface Science Society of, Editor. 2018, Springer Singapore: Singapore. p. 349-353.
115. McMurry, J.E., *Organic Chemistry*. 8th ed. 2012: Brooks/Cole.
116. Lahesmaa-Korpinen, A.-M., *Computational approaches in high-throughput proteomics data analysis*. 2012.
117. *The Reactor STM*. [cited 2020 28.05]; Available from: https://www.mn.uio.no/kjemi/english/research/groups/nafuma/laboratories/operando-methods/the-reactor-stm/.
118. *HIPPIE Beamline*. [cited 2020 28.05]; Available from: https://www.maxiv.lu.se/accelerators-beamlines/beamlines/hippie/.
119. Laboratory, M.I. 2017 [cited 2020 20.05.05]; Available from: https://twitter.com/MAXIVLaboratory/status/865181761134710784/photo/1.
120. Nečas, D. and P. Klapetek, *Gwyddion: an open-source software for SPM data analysis.* 2012. **10**(1): p. 181.
121. Horcas, I., R. Fernández, J.M. Gómez-Rodríguez, J. Colchero, J. Gómez-Herrero, and A.M. Baro, *WSXM: A software for scanning probe microscopy and a tool for nanotechnology*. Review of Scientific Instruments, 2007. **78**(1): p. 013705.
122. Ivashenko, O., *Personal Communication*. 2020.
123. Puglia, C., A. Nilsson, B. Hernnäs, O. Karis, P. Bennich, and N. Mårtensson, *Physisorbed, chemisorbed and dissociated O2 on Pt(111) studied by different core level spectroscopy methods.* Surface Science, 1995. **342**(1): p. 119-133.
124. Bergbreiter, A., A. Berkó, P. Erne, H. Hoster, and R. Behm, *On the origin of Ru bilayer island growth on Pt(111).* Vacuum, 2009. **84**: p. 13-18.
125. Carlisle, C.I., D.A. King, M.L. Bocquet, J. Cerdá, and P. Sautet, *Imaging the Surface and the Interface Atoms of an Oxide Film on Ag(111) by Scanning Tunneling Microscopy: Experiment and Theory.* Physical Review Letters, 2000. **84**(17): p. 3899-3902.
126. Todorova, M., E. Lundgren, V. Blum, A. Mikkelsen, S. Gray, J. Gustafson, M. Borg, J. Rogal, K. Reuter, J.N. Andersen, and M. Scheffler, *The Pd(100)–(5×5)R27°-O surface oxide revisited.* Surface Science, 2003. **541**(1): p. 101-112.

127. Lundgren, E., G. Kresse, C. Klein, M. Borg, J.N. Andersen, M. De Santis, Y. Gauthier, C. Konvicka, M. Schmid, and P. Varga, *Two-Dimensional Oxide on Pd(111).* Physical Review Letters, 2002. **88**(24): p. 246103.
128. Tao, F., M.E. Grass, Y. Zhang, D.R. Butcher, F. Aksoy, S. Aloni, V. Altoe, S. Alayoglu, J.R. Renzas, C.-K. Tsung, Z. Zhu, Z. Liu, M. Salmeron, and G.A. Somorjai, *Evolution of Structure and Chemistry of Bimetallic Nanoparticle Catalysts under Reaction Conditions.* Journal of the American Chemical Society, 2010. **132**(25): p. 8697-8703.
129. Rodríguez, J.A., J.C. Hanson, and P.J. Chupas, *In-situ characterization of heterogeneous catalysts*. 2013, Wiley: Hoboken, New Jersey.
130. Besenbacher, F., J.V. Lauritsen, and S. Wendt, *STM studies of model catalysts.* Nano Today, 2007. **2**(4): p. 30-39.
131. Lauritsen, J.V. and F. Besenbacher, *Model Catalyst Surfaces Investigated by Scanning Tunneling Microscopy*, in *Advances in Catalysis*, B.C. Gates and H. Knzinger, Editors. 2006, Academic Press. p. 97-147.
132. Su, X., P.S. Cremer, Y.R. Shen, and G.A. Somorjai, *Pressure Dependence (10^-10 - 700 Torr) of the Vibrational Spectra of Adsorbed CO on Pt(111) Studied by Sum Frequency Generation.* Physical Review Letters, 1996. **77**(18): p. 3858-3860.
133. Jensen, J.A., K.B. Rider, M. Salmeron, and G.A. Somorjai, *High Pressure Adsorbate Structures Studied by Scanning Tunneling Microscopy: CO on Pt(111) in Equilibrium with the Gas Phase.* Physical Review Letters, 1998. **80**(6): p. 1228-1231.
134. McIntyre, B.J., M. Salmeron, and G.A. Somorjai, *In situ scanning tunneling microscopy study of platinum (110) in a reactor cell at high pressures and temperatures.* Journal of Vacuum Science & Technology A, 1993. **11**(4): p. 1964-1968.
135. van Spronsen, M.A., G.J.C. van Baarle, C.T. Herbschleb, J.W.M. Frenken, and I.M.N. Groot, *High-pressure operando STM studies giving insight in CO oxidation and NO reduction over Pt(110).* Catalysis Today, 2015. **244**: p. 85-95.